Institute of Biomechanics

Center of Biomedical Engineering

Kronesgasse 5-I

8010 Graz, Austria

Master's Thesis

Constitutive Modeling of Collagen Fiber Dispersion

with Application to the Arterial Wall

to achieve the degree of

Master of Science

Author: Andreas J. Reinisch, BSc.

Supervisor: Professor Gerhard A. Holzapfel

Co-Supervisor: Andreas J. Schriefl, PhD

June 10, 2013

Contents

Abstract

Cardiovascular diseases are the leading cause of death in the western world, and an understanding of the development, progression and effects of these diseases is of crucial importance for their treatment. Pathologies such as atherosclerosis and aneurysms are, among other factors, also related to biomechanics and mechanobiology since the microstructure and, therefore, the mechanical properties of diseased tissues change. This calls for a structurally based constitutive model of the mechanical behavior of cardiovascular tissue to gain more insight into physiological and pathological processes of the tissue. To this end we strive for a model which accounts for the structure and geometry of the cardiovascular system. Such a model has to incorporate the orientation and dispersion of collagen fibers which are the mechanically most important constituents in the passive arterial tissue. Since we want to account for the complex geometry of blood vessels we utilize numerical methods which in turn call for an efficient mathematical framework to solve the initial/boundary value problems.

A newly developed approach is based on experimental data of collagen fiber orientations of human arteries, from which two parameters quantifying the in-plane (circumferential-axial plane) and out-of-plane (radial-axial plane) dispersion of the fibers are extracted. Using these dispersion measures, an average fiber stretch based on the fiber distribution and the macroscopic kinematics is computed and incorporated in a hyperelastic, nonlinear and structurally motivated anisotropic continuum mechanical framework. The necessary mathematical and mechanical background is provided and the implementation of this model for the biaxial tension test, inflation test, and in a finite element code is shown. Finally, results of mechanical tests of human arteries are compared to the output of our model. In conclusion, a computationally efficient model based on histological data and capable to reproduce experimental results is presented.

Kurzfassung

Erkrankungen des Herz-Krauslaufsystems sind die führende Todesursache in der westlichen Welt und für ihre Behandlung ist es von größter Bedeutung deren Entstehung, Verlauf und Auswirkungen zu verstehen. Pathologien wie Atherosklerose und Aneurysmen sind stark mit Biomechanik und Mechanobiologie verknüpft, da sich unter anderem die Mikrostruktur und damit die mechanischen Eigenschaften des Gewebes ändern. Deshalb streben wir nach einem Modell des mechanischen Verhaltens von weichen biologischen Geweben, um Einblicke in die physiologischen Prozesse und pathologischen Veränderungen zu bekommen. Dieses Modell muss die Orientierung und Dispersion von Kollagenfasern, welche die wichtigste Rolle für das passive Verhalten von arteriellem Gewebe spielen, berücksichtigen. Um die komplexe Geometrie von Blutgefäßen zu erfassen benötigen wir numerische Methoden wie die Finite Elemente Methode und effiziente Verfahren, um die auftretenden Randwertprobleme zu lösen.

Der hier präsentierte Ansatz basiert auf histologischen Daten der Kollagenfaserverteilung in menschlichen Arterien, aus denen zwei Parameter, welche die Streuung der Kollagenfasern beschreiben, extrahiert werden. Mit diesen Parametern ist es möglich, die durchschnittliche Dehnung der Fasern aufgrund der makroskopischen Verformung zu berechnen. Diese Dehnung wird in einem hyperelastischen Modell verwendet, das die Nichtlinearität und Anisotropie des Gewebes beschreiben kann. Die Implementierung des Modells für den biaxialen Zugversuch, den Inflationstest und einen effizienten Finite-Elemente-Code und wird gezeigt und die notwendigen mathematischen und mechanischen Grundlagen werden beschrieben. Außerdem werden Ergebnisse von mechanischen Tests an menschlichen Arterien mit den Resultaten des vorgestellten Modells verglichen. Zusammenfassend wird ein Modell, das auf histologischen Daten basiert und experimentelle Ergebnisse reproduzieren kann, präsentiert.

Acknowledgment

First of all, I wish to acknowledge my family who always supported me during my studies and made it possible for me to deepen my knowledge at the universities in Graz and, during my exchange semester, in Eindhoven.

My sincere gratitude goes to my supervisor, Prof. Gerhard A. Holzapfel, who also gave me the opportunity to work at the Institute of Biomechanics for three years, what kindled my enthusiasm and motivation for biomechanics. The possibilities to present at conferences, work in an international team and contribute to scientific publications are certainly among the most important experiences during my studies. With his profound knowledge of mechanics, biology and medicine he always steered me in the right direction when I was at the end of my wits.

I am particularly grateful for the support of Dr. Andreas J. Schriefl who was the co-supervisor of my thesis and always available for me if I had any question. Not only his extensive insight into physics and biology but also the relaxed but yet fertile working atmosphere make it a real joy to work with him.

Many others also deserve to be acknowledged here, especially my coworkers from the Institute of Biomechanics. Michael J. Unterberger was a big help with everything related to mechanics and programming, and Thomas S. E. Eriksson spared no efforts to help me with finite elements and all related questions. The atmosphere at the institute made it a pleasure to work there, especially thanks to my longtime colleague sitting next to me, Gerhard Sommer, who always found ways to cheer me up.

Finally I say thanks to my friends and colleagues who made it so enjoyable to study in Graz and Eindhoven and with whom I shared this great time of my life.

‘*And you will find someday that, after all, it isn’t as horrible as it looks.*’

RICHARD P. FEYNMAN

.

1 Medical Background

'Human subtlety will never devise an invention more beautiful, more simple or more direct than does nature because in her inventions nothing is lacking, and nothing is superfluous.'

LEONARDO DA VINCI

Nature has been an inspiration for human mankind for ages, and even though painters, sculptors, writers and other artists are the first who come into mind when talking about inspiration, also engineers can benefit from looking at the structures and functions in living organisms which perfected by evolution over millions of years. We cannot only learn from nature to improve engineering applications (a discipline called biomimetics), but also intervene in biological systems which are out of equilibrium, especially in the human body. Changes in our lifestyle (diet, less exercise, ...) occur so fast that evolutionary processes cannot keep pace, leading to so called lifestyle diseases (e.g., atherosclerosis, cancer, diabetes, stroke). In addition, a system so complex as the human body is subjected to a lot of possible dysfunctions and injuries which cannot, at least not in a satisfactory manner, be compensated by natural regulation mechanisms. Here engineers can help to improve the medical treatment and diagnoses and use their skills and tools to gain more insight into the development and progression of diseases. To this end we seek to determine the structure and function of, e.g., nucleic acids, proteins, cells, tissues and organs, and fortunately we do not have to loot graveyards like Leonardo[1] to obtain specimens for our experiments. Instead, we are able to look into the human body without even touching it using techniques like X-Ray, MRI, ultrasound and so on, we can use elaborate tools such as the finite

[1] Who was also a productive researcher in biomechanics.

element method to solve complex mathematical problems, and we can access a vast amount of literature to guide and inspire us. The challenges we are facing are not abstract mathematical problems, instead it is our goal to improve the overall state of health.

Chapter one will give a brief overview of the underlying biological background and medical pathologies which motivate our work, starting with a general description of the cardiovascular system. Subsequently we will go to the tissue/molecular level and review the microstructure of arteries, where we focus on collagen as the main contributor to the mechanical behavior of soft tissue in general and blood vessels in particular. We choose atherosclerosis as an example of pathological disorder in blood vessels which is of special interest in the context of biomechanics. Finally, we will see that biomechancis and mechanobiology are an important part in understanding diseases and their treatment.

1.1 The Cardiovascular System

Already in a four week old fetus the cardiovascular system (CVS) starts to function, and it is the last system to cease at the end of life. The main functions of the CVS are (i) supplying tissues with oxygen and nutrients, (ii) removing the waste products accumulated during cellular metabolism[2] and (iii) transporting hormones. To perform these tasks, the CVS consists of a pump (the heart) and a conduit system (the blood vessels or circulatory system). The low-pressure system of the CVS (the right side of the heart, the veins and the pulmonary circulation) is pressurized with $3 - 8$ kPa and perfuses the lungs where oxygen (O_2) is taken up and carbondioxide (CO_2), a waste product of cellular respiration, is released. With pressures from $10 - 16$ kPa, the left ventricle of the heart and the systemic circulation form the high pressure system. The aorta is the largest vessel of the systemic circulation and arches out of the left ventricle of the heart, from where it extends into the abdomen, where it divides first into the common iliac arteries and ultimately branches into thin walled (one cell thick) capillaries [Kowalak et al., 2001].

The walls of arteries are in general thicker than those of veins because they have to resist a higher pressure, while veins are endowed with valves to prevent the backflow of blood. The

[2] The waste products are transported to the kidneys, liver and skin where they are excreted.

thickness gradually decreases [Schriefl et al., 2012a] as the vessels become smaller, while the wall to lumen ratio becomes bigger. Blood vessels are composed of three main constituents, namely the endothelium, SMCs, and connective tissue containing elastic elements.

1.2 Microstructure of Cardiovascular Tissue

In continuum mechanics we assume that the mechanical properties are determined by the microstructure of the material. Hence, we will take a closer look at the microstructure of cardiovascular tissue which depends largely on the extracellular matrix (ECM). It not only governs the mechanical properties but also plays an important role in biological processes, e.g., cells migrate through the ECM, adhere to it, and develop their phenotype depending on their environment; proteins and small molecules, such as ions anchor to it; and nutrients and hormones diffuse into the ECM which connects cells and the supplying capillary network [Humphrey, 2002]. The ECM shows solid- and fluid-like behavior, where the fluid phase has dissolved chemical species and consists mainly of water while the solid phase is constituted of cells (mainly fibroblasts and SMCs) and their products, namely collagen fibers, elastin (which is only synthesized prenatally) and proteoglycans (PGs). Although the ECM contains various different constituents, only collagen fibrils and PGs are present in all connective tissues [Ottani et al., 2001]. The large interstitial PGs are believed to maintain the shape of the tissue and render the material incompressible by binding water. A higher compressibility might increase the transmural transport of atherogenic lipoproteins and therefore promote the development of atherosclerotic lesions [Boutouyrie et al., 2001], see section 1.5. While the role of PGs in other tissues like cartilage or the intervertebral disk is well understood, their function in vascular mechanics is not clear. In a recent contribution [Azeloglu et al., 2007], e.g., the authors hypothesize about the influence of PGs on the residual stress regulation in the aorta.

The components of the ECM are in continuous interaction, for example fibroblasts and SMCs produce collagen which in turn interacts with SMCs changing their phenotype and activity (depending on the type of collagen, see 1.3 [Díez, 2007]). In this thesis we do not account for the active behavior of muscle cells but only account for the passive mechanical behavior of the tissue which is mainly governed by elastin and collagen.

Elastin. As the name suggests, the protein elastin endows tissues such has the lung, skin and blood vessels with elasticity. Since elastin returns to its original configuration when the load is removed (truly elastic material), it is believed that its primary role is to store and return mechanical energy [Humphrey, 2002]. Elastin is the major component of elastic fibers in the ECM and is synthesized in less than one day by fibroblasts and SMCs [Davidson et al., 1986]. It is the most biologically stable protein (in most organisms it has a half-life in the order of the lifespan[3]) and also the most elastic one [Taylor and Humphrey, 2009]. Elastin fibers are from 0.2 to $5\,\mu$m in diameter and can take up uniaxial extension of up to $150\,\%$ without breaking, where collagen fails around $10\,\%$. The precursors of elastin, tropoelastin molecules, are highly connected by crosslinks [Labrosse, 2007], giving the elastic arteries near the heart the ability to distend during systole and recoil during diastole.

Elastic Properties of Arteries. The artery is not only a conduit system for the blood flow, but also serves as a reservoir for the blood pressure. The distensibility of the elastic arteries (the arteries close to the heart) is one of the most important properties of the cardiovascular system and arises from the microstructure of the extracellular matrix. It allows the aorta to distend during systole (the phase in the cardiac cycle when the heart contracts) and therefore to store some of the energy of the heart beat. Between the cardiac contractions, the elastic recoil propels blood through the peripheral vascular system. This vital function is known as the Windkessel effect which describes the capacitive behavior of the arteries 'smoothing' the blood flow and reducing the load on the heart [Wagenseil and Mecham, 2009]. It was mathematically quantified in 1899 by Otto Frank [Frank, 1899/1990], a main contributor to arterial mechanics after whom also the Frank-Starling law of the heart was named [Parker, 2009].

Arterial stiffening is one of the major effects of ageing and results in a less compliant aorta, meaning that the vessel less readily expands. This loss of elasticity is a major problem and it is widely recognized that the (macro)molecules in the extracellular matrix are, together with transmural pressure, the main factors in arterial stiffness [Díez, 2007].

[3] Note that in humans the half-life of elastin is around 40 years [Arribas et al., 2006].

1.3 Collagen

With an ultimate tensile strength in the range of $50 - 100$ MPa [Fung, 1993], collagen fibers endow soft biological tissues with the ability to resist loads in the direction of the fibers. Due to the gradual recruitment of collagen fibers upon deformation, they render the mechanical behavior of soft biological tissues nonlinear, a phenomenon found in all vertebrae [Shadwick, 1999, Fung, 1981]. Since collagen fibers are able to withstand high tensile stresses, they are essential in tissues such as tendons and ligaments whose main function is to transfer (tensile) forces in one direction (between muscle/bone and bone/bone), where the collagen fibers are aligned towards the same direction forming a 'fiber family'. Also other tissues such as the arterial wall, cartilage or the cornea are endorsed with collagen fibers, where the number, direction and dispersion of fiber families can vary from tissue to tissue and also depend on the location of the tissue in the body (see, e.g., [Schriefl et al., 2012a] for orientation and dispersion of collagen fibers along the aorta and the common iliac arteries).

In the human body there are 28 known types of collagen, whereas in the human artery only type I and III are abundant [Hulmes, 2008, Taylor and Humphrey, 2009]. They are synthesized by fibroblasts and SMCs, while type IV collagen for example is deposited in the ECM by endothelial cells. Depending on the type, it takes a cell 10-60 min to synthesize a complete intracellular collagen precursor, called procollagen (tripal-helical protein chains with a length of about 300 nm) [Nimni, 1992] which is then excreted to the extracellular space. In the ECM, collagen molecules assemble themselves to groups of four or five molecules, so called fibrils. These molecules are ordered in parallel with a characteristic d-spacing, where the molecules are shifted by 67 nm inside the fibrils (see Fig. 1.1d). A fibril has a thickness in the range of 50 to a few hundred nanometers and many fibrils form a collagen fascicle with a diameter of 50 to 300 μm [Humphrey, 2002]. Immediately after secretion, collagen fibrils have no tensile strength but obtain their resistance to tension through subsequent formation of inter- and intramolecular covalent crosslinks [Reiser et al., 1992]. Collagen fibers are subdivided into multiple, parallel threads of equivalent cross section, an arrangement which has two advantages: (i) the propagation of cracks is prohibited (Cock-Gordon effect) and (ii) the flexibility increases tremendously (it is inversely proportional to the forth power of the radius of each thread) [Ottani et al., 2001].

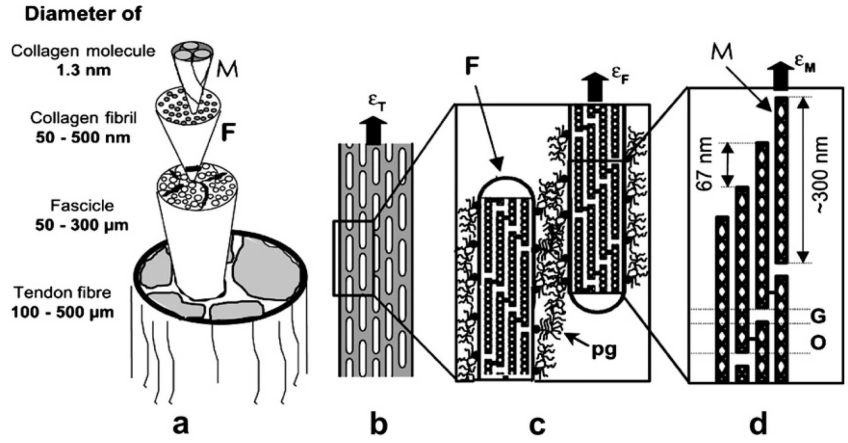

Figure 1.1: (a) Illustration of the hierarchical structure of a tendon which is composed of fascicles containing collagen fibrils (F), which in turn are made up of parallel collagen molecules (M). (b) The tendon is a composite of collagen fibrils and a proteoglycan-rich matrix. (c) If the tissue is subjected to the strain ε_{t}, some strain will be partly taken up by the proteoglycan matrix and partly transmitted to the fibrils carrying the strain ε_{F}. (d) In the unloaded tissue, the collagen molecules are staggered with an axial spacing of 67 nm while the lateral spacing is around 1.5 nm [Fratzl and Weinkamer, 2007].

The half-life of collagen strongly depends on the location in the body, e.g., it is only a few days in the periodontal ligament, weeks to months in the arterial wall, many months in tendons and possibly years in bones. In comparison, most *intracellular* proteins have a half-life of hours or days [Alberts et al., 1994, Humphrey, 2002]. The turnover of collagen is believed to be regulated by the local state of stress and/or strain [Humphrey, 2002].

Collagen Fiber Dispersion. In [Schriefl et al., 2012a], the three-dimensional orientation of collagen fibers in the human aorta and common iliac arteries was quantified. The researchers studied eleven healthy, non-atherosclerotic samples exploiting the birefringent properties of collagen enhanced by picrosirius red staining. The lack of existing constitutive models to properly represent the results of [Schriefl et al., 2012a], i.e., the dispersion of collagen fibers, are the key motivation for this thesis. Other follow-up works, e.g. [Schriefl et al., 2012b,d], continued to investigate the dispersion of collagen fibers, and recently also the fiber dispersion in the diseased artery was quantified [Schriefl et al., 2012a]. One of the key results is that in diseased arteries, the out-of-plane dispersion is much higher than in healthy ones and cannot be neglected [Schriefl et al., 2013a]. This topic will be discussed in more detail in chapter 4 of this thesis.

1.4 Structural Composition of Arteries

Based on their location in the human body, arteries can be classified into the elastic type (close to the heart), muscular type (distributing the blood from elastic arteries to the periphery), and arterioles (in the tissue, main contributors to the flow resistance). However, for our purposes it is more interesting to take a look at the microstructure of the tissue. Even without a microscope we can distinguish three concentric layers in arterial cross sections, namely the intima, media and adventitia (from the lumen to the outer border, respectively, see Fig. 1.2). For a detailed review of the structure of these layers, the reader is referred to the works of [Schoen, 1994, Gottlieb, 2007, Holzapfel et al., 2000]. In this thesis we will give a very brief overview of the main histological and mechanical properties of these layers. It should be noted that the structure and composition of each layer depend on the location in the body, since the vessels have to meet different requirements along the arterial tree [Schriefl et al., 2012a].

Intima. The intima is the innermost layer of the artery and in direct contact with the blood stream. In the healthy artery of newborns it consists only of a (mechanically negligible) subendothelial layer covered with a monolayer of endothelial cells. Processes such as arteriosclerosis (natural stiffening of the artery with age) and atherosclerosis (pathological deposition of various substances in the intima, see section 1.5) can change the biochemical composition and mechanical behavior of the intima [Holzapfel et al., 2005a], making it mechanically relevant. In the capillaries at the end of the arterial tree where water, oxygen, nutrients, hormones and waste products are exchanged between blood and the surrounding tissue, the intima consists only of an endothelial lining to with a thickness of one layer to facilitate diffusion. In contrast to most animals, the human intima also contains resident SMCs [Libby et al., 2011].

Media. The media consists of a three-dimensional network of SMCs, elastin and collagen fibers and is the mechanically most important layer in the healthy arterial wall. It endows the artery with tensile strength in both the circumferential and axial direction because of collagen fibers oriented in preferred directions (see section 1.3), so called fiber families [Holzapfel et al., 2000]. The SMCs allow the media to adapt its diameter by narrowing (vasoconstriction) or widening (vasodilatation) the lumen to regulate blood pressure and flow [Gottlieb, 2007].

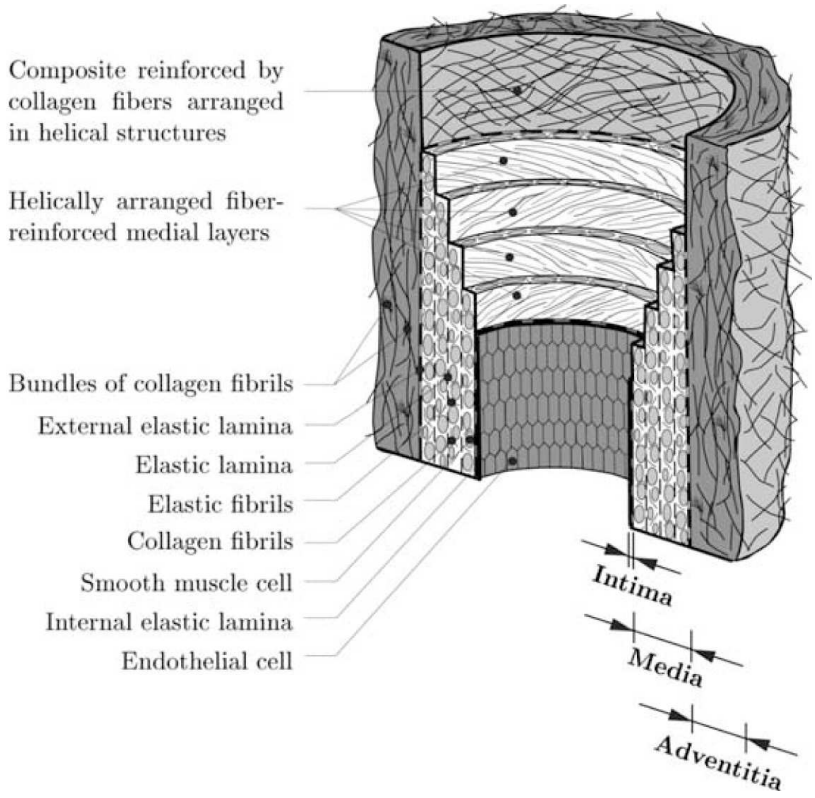

Figure 1.2: Schematic of a healthy elastic artery composed of three layers: intima (I), media (M) and adventitia (A). In a healthy elastic artery, the intima consists of a single layer of endothelial cells which do not contribute to the mechanical behavior of the arterial wall. The subendothelial layer is composed of SMCs and collagen fibrils and its thickness varies with location in the body, age and disease. The media contains SMCs, elastic and collagenous fibrils organized in layers. In the outermost layer, the adventitia, thick bundles of collagen fibrils are arranged in helical structures which serve to protect the artery from overstretching [Holzapfel et al., 2000].

Adventitia. The outermost layer is mainly composed of ground substance and thick bundles of collagen fibers which are produced by fibroblast and fibrocytes. The collagen fibers are arranged helically and give the adventitia its strength in the supra-physiological load domain, where it serves as a preventive 'jacket-like' tube protecting the artery from rupturing [Burton, 1954]. In the physiological loading domain, however, the fibers are crimped and do not contribute to the mechanical behavior. In cerebral arteries, the adventitia is completely absent, in elastic arteries it makes up around $10\,\%$ of the wall thickness and in muscular arteries this ratio is even higher [Labrosse, 2007]. Moreover, the adventitia is surrounded by loose connective

tissue and contains the vasa vasorum[4], i.e., vessels that perfuse the vascular wall since in large arteries the supply of oxygen by diffusion from the lumen to the outermost layers of the media and adventitia is not sufficient [Schoen, 1994]. This vasculature network makes the adventitia a prominent site of vascular inflammation [Wagenseil and Mecham, 2009].

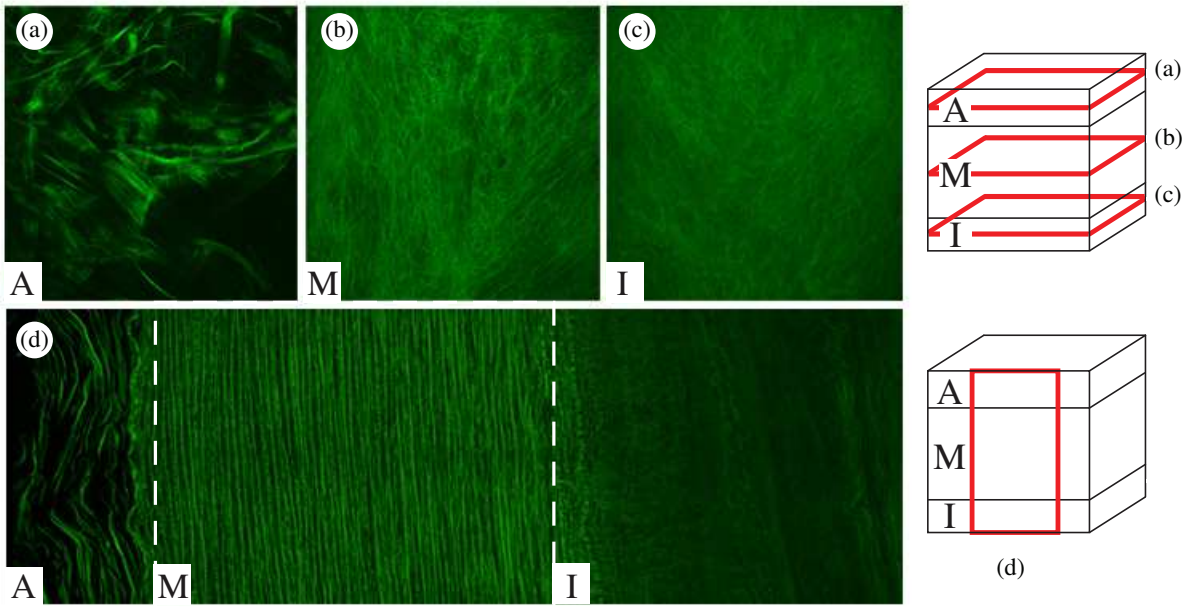

Figure 1.3: Second harmonic generation images of a healthy, non-atherosclerotic human abdominal aorta. In (a)-(c), the in-plane orientation of collagen fibers in the adventitia, media and intima is shown, respectively. These images show the arrangement of collagen fibers, schematically depicted in Fig. 1.2, i.e.; fiber bundles in the avdentitia, fiber families in the media and an isotropic fiber network in the intima. In (d), a cross-section of the entire wall is shown, where the adventitia is at the very left and the intima is located at the right of the image. Therefore, the horizontal and vertical sides of the image correspond to the radial and axial direction, respectively. The media clearly shows a high in-plane orientation of fibers in the circumferential-axial plane. At the very right, the location of the respective images (a-d) of the layers is depicted. Unpublished images, taken with permission from Andreas J. Schriefl.

[4]Latin for ‘the vessels of the vessels’.

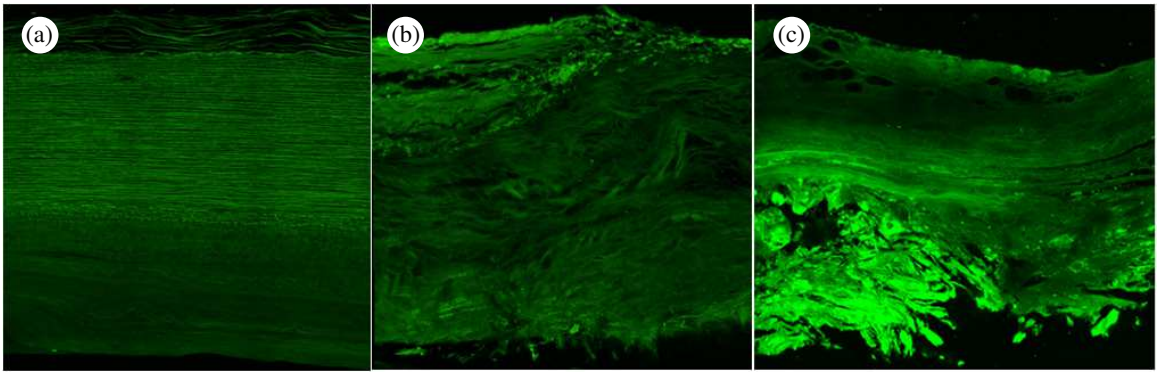

Figure 1.4: Image (a) shows the entire wall of a healthy human abdominal aorta, while (b) and (c) show cross-sections of atherosclerotic wall tissue. In the healthy wall we can distinguish the three layers, whereas in the diseased sample these layers merge into each other. Moreover, the atherosclerotic arterial wall displays considerable out-of-plane dispersion and a very inhomogeneous structure which varies strongly between each specimen. Unpublished images, taken with permission from Andreas J. Schriefl.

1.5 Pathologies of the Cardiovascular System

Due to the complexity of the CVS a variety of complicated pathological changes with potentially dramatic consequences can occur. The importance of cardiovascular diseases (CVDs) is also highlighted by the World Health Organization (WHO) in [WHO Media centre, 2012], from where we cite four of the main key facts related to CVDs:

- CVDs are the number one cause of death globally: more people die annually from CVDs than from any other cause.
- An estimated 17.3 million people died from CVDs in 2008, representing 30% of all global deaths. Of these deaths, an estimated 7.3 million were due to coronary heart disease and 6.2 million were due to stroke.
- Low- and middle-income countries are disproportionally affected: over 80% of CVD deaths take place in low- and middle-income countries and occur almost equally in men and women.
- By 2030, almost 25 million people will die from CVDs, mainly from heart disease and stroke. These are projected to remain the single leading cause of death.

One example of a CVD is the progressive narrowing of the vessel lumen leading to ischemia of the tissue perfused by that vessel, a problem especially in the heart. The effect of this narrowing is immediately clear when considering Poiseuille's law which states that the flow through a tube is inversely proportional to the forth power of the diameter. Although this law includes some assumptions not valid for the artery (rigid vessel wall, developed flow, ...), it provides an impression of the profound flow-limiting effects caused by a narrowed lumen. Other pathological changes include intravascular thrombosis, causing acute obstruction and/or embolism and weakening of the vessel walls, leading to dilatation (aneurysm formation) or rupture. In order to understand and effectively treat these diseases, it is important to consider the underlying structure of the vessel and the related biochemical and biomechanical changes [Schoen, 1994, Humphrey, 2002].

Atherosclerosis. Probably the most important disease related to blood vessels is atherosclerosis, which is characterized by intimal thickening and lipid deposition in the arterial wall and is a form of arteriosclerosis, literally meaning hardening of the arteries. Arteriosclerosis is a group of diseases which is characterized by thickening and stiffening of the arteries and manifests as two other morphologies besides of atherosclerosis, namely Monckbergs medial calcific sclerosis (calcification of the media of muscular arteries) and arteriolosclerosis (proliferative hyaline thickening of the walls of small arteries and arterioles) [Schoen, 1994]. Atherosclerosis is the most common and important form of arteriosclerosis.

In Fig. 1.5, key steps in the development of an atherosclerotic lesion is shown. Due to irritating stimuli (dyslipidaemia, hypertension, pro-inflammatory mediators), leukocytes from the blood stream adhere to the activated endothelial monolayer and migrate into the intima. Most of the leukocytes are monocytes which differentiate into macrophages and absorb lipids, which turns them into foam cells. Subsequently SMCs migrating from the media into the intima and resident SMCs in the intima proliferate, resulting in an increased production of ECM components. As a consequence, inflammatory cells, SMCs, lipid and connective tissue progressively aggregate in the intima of the large and medium-sized elastic and muscular arteries. Dying cells in advancing lesions leave extracellular lipid and cellular debris behind which can accumulate in the central region of the plaque [Libby et al., 2011]. In the classic case, the atherosclerotic lesion is a fibroinflammator lipid plaque (atheroma) which spreads into the media of the arte-

rial wall and into the lumen of the vessel, leading to a stenosis (narrowing) of the lumen. The three main components of such a plaque are cells (SMCs, macrophages and other leukocytes), connective tissue (collagen, elastin, proteoglycans) and lipid deposits (both intra- and extracellular), mainly cholesterol which is derived from lipoproteins in the blood. Rupture of the fibrous cap initiates blood coagulation and leads to thrombus formation, the ultimate complication of atherosclerosis. A complicated atherosclerotic plaque is described by the transformation of a simple atheroma to a complicated lesion. It is characterized by calcification, i.e., mineral deposition and resorption regulated by osteoblast-like and osteoclast-like cells in the vessel wall [Schoen, 1994].

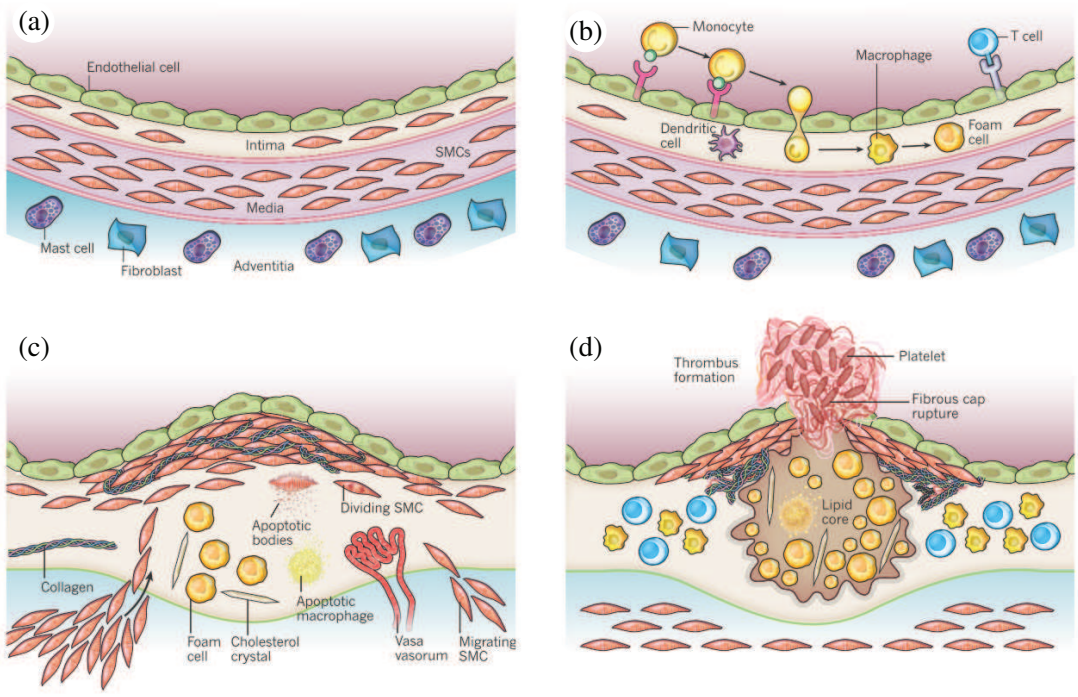

Figure 1.5: In (a), the three layers of the artery are shown, for details see section 1.4 and Fig. 1.2. Panel (b) shows the initial stage of atherosclerosis where leukocytes migrate into the intima and in (c) the SMCs migration and proliferation is shown. Finally, in (d) thrombus formation is depicted. For details, see [Libby et al., 2011], from where the picture was taken and modified.

The major causes of atherosclerosis are hyperlipidemia, hypertension, cigarette smoking and diabetes. Other risk factors of atherosclerosis are obesity, physical inactivity, male gender, increasing age, family history, stress, oral contraceptives and high carbohydrate intake [Schoen, 1994]. There is no single hypothesis explaining the origin of atherosclerosis but several, not

mutually exclusive mechanisms have been proposed (e.g., the insudation hypothesis, encrustation hypothesis, reaction to injury hypothesis, monoclonal hypothesis). The trigger which initiates the process is most controversial, but the focal nature of this disease suggests that complex flow fields of the blood and therefore biomechanics and mechanical factors, e.g., low shear stresses, etc., play an important role. For further details, the reader is referred to [Humphrey and Canham, 2000, Schoen, 1994, Gottlieb, 2007, Kowalak et al., 2001].

There are many potential complications arising from atherosclerosis, e.g., embolism or acute occlusion caused by the rupture of an atherosclerotic plaque and subsequent flow with the blood until it completely occludes the lumen of a muscular artery. This results in an infarction (ischemic necrosis) of the tissue which should otherwise receive blood supply by the obstructed vessel, causing myocardial infarction (in the heart), stroke (in the brain) or gangrene (in the intestine or lower extremities). Another pathology caused by atherosclerosis is the chronic narrowing of the vessel lumen by the plaque. Due to the chronic shortage of blood, the organ suffers of atrophy. A complicated lesion can also extend into the media of an elastic artery and weaken the wall, promoting the development of an aneurysm. This typically happens in the abdominal aorta (abdominal aortic aneurysm, AAA) and can lead to a vascular catastrophe in case the aneurysm ruptures.

Any artery can be subjected to atherosclerosis, but the aorta, the coronary and the cerebral systems are most likely to be affected. Therefore, aortic aneurysms, myocardial infarction and cerebral infarction are the most common consequences of this abnormality of the arterial wall [Schoen, 1994]. If the coronary arteries are affected by atherosclerosis, the diminished blood flow can result in coronary artery disease (CAD). Also the ability of the vessel to dilate is reduced, altogether leading to an insufficient supply of oxygen and nutrients to the myocardium beyond the lesion. This results in local myocardial ischemia within $10\,\mathrm{s}$ after coronary artery occlusion. Within several minutes, the lack of oxygen forces myocardiac cells to shift from aerobic to anaerobic metabolism resulting in an accumulation of lactic acid and consequent reduction of cellular pH. This combination of hypoxia, reduced energy availability and acidosis results in abnormal shortening of muscle fibers which reduces the strength of contractions in the affected region. As a consequence, less blood can be ejected from the heart with each contraction [Kowalak et al., 2001].

1.6 Medical Interventions

One of the most common medical interventions to treat the narrowed lumen of an artery is percutaneous transluminal coronary angioplasty (PTCA), especially for the epicardial coronary arteries. In this procedure, a balloon catheter is inserted in the coronary arteries where it is inflated to push the plaque into the media and dilate the stenotic vessel. Although in most cases the vessel lumen is satisfactorily dilated, the balloon causes endothelial damage. In 30 to $40\,\%$ of treatments, intimal hyperplasia due to smooth muscle cell proliferation and matrix deposition leads to restenosis over a period of three to six months. Moreover, wall remodeling also causes narrowing of the lumen through contraction of the vessel wall. Drug eluting stents with anti-proliferative agents inhibit the growth of smooth muscle cells in the vessel wall by blocking the cell cycle and thus reduce restenosis by a considerable amount [Gottlieb, 2007]. However, the detailed mechanical and biochemical processes and long term complications are not fully understood yet, requiring more research including a reliable model of the growth, remodeling and related arterial mechanics accounting for the finite deformations of the arterial wall. The importance of biomechanics is illustrated in, e.g., [Holzapfel et al., 2005b] where the researchers demonstrated that also the geometry and material properties of the stent are important.

2 Continuum Mechanical Framework

'To get into this question [of tissue elasticity] more closely, without the aid of mathematics, is scarcely possible.'

C. S. ROY

As we have seen in the previous chapter, mechanics plays an important role in many physiological and pathological processes in the human body. Medical interventions like PTCA as well as diseases like aneurysms require a detailed knowledge of the stresses and strains in the tissue to make predictions and guide medical doctors in the diagnosis and operations. Especially the maximum stress in the arterial wall is of great interest to asses, e.g., the severeness of an aneurysm and classify its rupture potential. To provide the necessary mathematical and mechanical background for this thesis, we will review some of the the basic concepts and methods in continuum mechanics in this chapter. For a more detailed introduction to continuum mechanics see, e.g., the books of [Ogden, 1997, Holzapfel, 2000] on which this chapter is largely based.

The overview presented here will introduce a central quantity in continuum mechanics, the local deformation gradient $\mathbf{F}$, which maps a vector from the undeformed (reference) configuration to the deformed (current) configuration[1]. With this quantity we define a measure of deformation, the right Cauchy-Green tensor $\mathbf{C}$, which is independent of rigid body motions (translocations and rotations). This deformation measure can be incorporated in an important quantity in the context of hyperelasticity, namely the strain-energy Ψ induced in the body by the

[1]The undeformed configuration is also called the material or Lagrangian configuration while the deformed configuration is also referred to as the spatial or Eulerian configuration.

deformation[2]. The strain-energy function (SEF) is used to derive the elasticity tensor and the stress tensor required for the finite element implementation of the constitutive model. Therefore, we will also discuss the elasticity tensor (in both the Lagrangian and Eulerian setting), the most important stress tensors, and the theory of anisotropy for finite deformations.

2.1 Continuum Bodies and their Deformations

Although living tissues possess many properties which are unusual in engineering applications (they grow, remodel, are mixtures of very different and inhomogeneous materials, ...), they still obey the basic postulates of mechanics (e.g., the conservation laws)[3]. Also fundamental quantities such as stress, strain and entropy are convenient measures in the analysis of such materials. Even though we might have to adapt the set of tools we use as engineers, we still can use familiar concepts and seek to formulate constitutive relations and solve initial/boundary value problems (I/BVP). We should be aware that constitutive equations do not describe the material, but rather the behavior of the material under specific conditions. Nevertheless, the formulation of constitutive equations helps us to gain insight into the function and structure of the material and is essential to solve engineering problems. In this context, continuum mechanics provides us with very useful theories to solve the resulting differential equations with their initial/boundary values.

In continuum mechanics we describe a body, denoted $\mathcal{B}$ (see Fig. 2.1(a)), as a continuous assembly of matter in space. With this fundamental assumption we 'smear out' details at the molecular and atomic level and, therefore, lose a lot of information. Nevertheless this approach is essential in engineering applications since it allows us to reduce the amount of information so we can handle it in a computationally efficient way. Moreover, we do not seek to describe the state of every single microscopic particle, but instead aim to represent the body in the macroscopic world, so it is important to determine the size of a finite volume element. On the one hand, this finite element should be large enough to represent the contained particles in a proper

[2] Note that also other deformation measures such as $\mathbf{F}$ could be used in the SEF.

[3] Since tissues are able to grow, they are an open system where mass can be transported over the system boundaries.

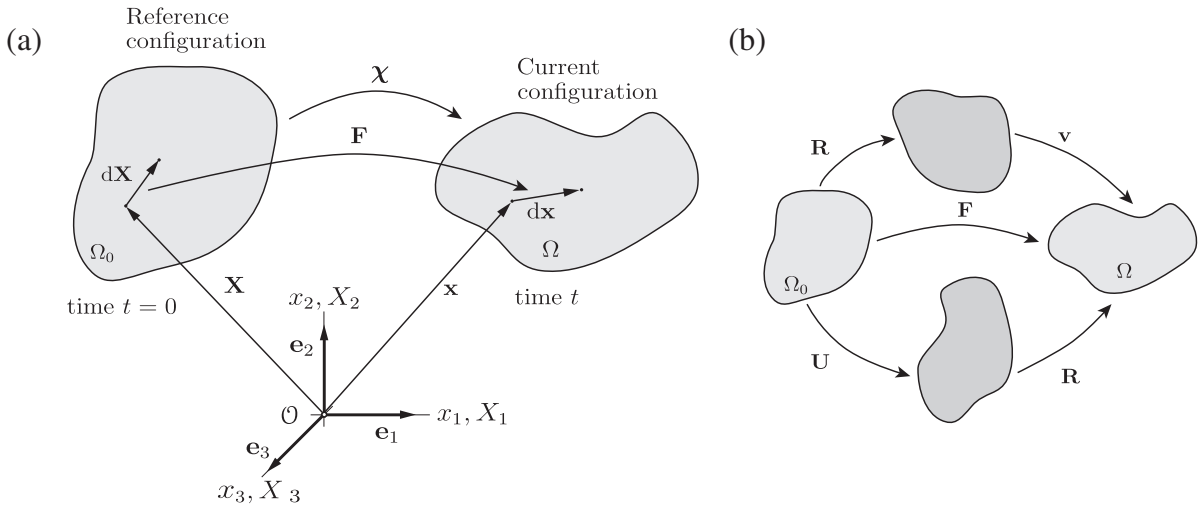

Figure 2.1: In panel (a), the transformation of a body from the reference configuration Ω_0 to the deformed configuration Ω by the map $\boldsymbol{\chi}(\mathbf{X}, t)$ is displayed. The vector $\mathrm{d}\mathbf{X}$ in the reference state Ω_0 is transformed to the deformed vector $\mathrm{d}\mathbf{x}$ into the spatial setting by the deformation gradient $\mathbf{F}(\mathbf{X}, t)$. Panel (b) shows the polar decomposition of the deformation gradient $\mathbf{F}$ into a rotational part $\mathbf{R}$ and a stretching part, either $\mathbf{U}$ or $\mathbf{v}$, the right and left stretch tensors, respectively.

way, on the other hand it must be small enough to be treated analytically. Fung describes this as 'The concept of a material as a continuum is a mathematical idealization of the real world and applicable to problems in which the finite structure of matter can be ignored.' [Fung, 1965].

Such a collection of particles forming the body $\mathcal{B}$ can be represented in an arbitrary coordinate system. For our purpose, a set of orthonormal basis vectors $\{\mathbf{e}_1, \mathbf{e}_2, \mathbf{e}_3\}$ is convenient to describe a point $P \in \mathcal{B}$ in 3D space. Since we are solely operating in a Cartesian coordinate system, we will in the following not distinguish between co- and contravariant components of tensors. The continuum body $\mathcal{B}$ can move and occupies a geometrical region $\Omega_0, ..., \Omega$ at every point of time t. For $t = 0$ we define a special region Ω_0, called the reference (undeformed) configuration[4].

Theoretically, the reference and the current configuration could be defined in different coordinate systems and hence we had to write[5] $\mathbf{X} = X_A \mathbf{E}_A$ in the Lagrangian setting and $\mathbf{x} = x_a \mathbf{e}_a$

[4]We write quantities in the reference configuration in capital letters while quantities in the deformed configuration are denoted by lower case symbols.

[5]We use Einstein summation convention where we sum over indices which appear twice.

in the Eulerian configuration. In our analysis, however, the coordinate systems for the material and spatial configuration coincide (i.e., the material and the spatial reference frame are collinear) and we denote the axis by the unit vectors $\mathbf{e}_a$ and the coordinate axis by x_a, X_A. The motion $\boldsymbol{\chi}(\mathbf{X}, t)$ transforms a body from Ω_0 to the current (deformed) configuration Ω by $\mathbf{x} = \boldsymbol{\chi}(\mathbf{X}, t)$. The inverse motion is denoted by $\boldsymbol{\chi}^{-1}(\mathbf{x}, t)$ and maps a point from the current configuration back to the reference configuration, i.e., $\mathbf{X} = \boldsymbol{\chi}^{-1}(\mathbf{x}, t)$. The mapping $\boldsymbol{\chi}$ defines a so called push-forward of quantities from the material configuration to the spatial configuration, whereas $\boldsymbol{\chi}^{-1}$ is called the pull back and maps a tensor from the Eulerian setting to the Lagrangian configuration. Depending on whether this quantity is a co- or contravariant[6] tensor, these operations are different. The push-forward and pull-back of contravariant tensors (such as the most common stress tensors) are defined as

$$\boldsymbol{\chi}_*(\bullet)^{\#} = \mathbf{F}(\bullet)^{\#}\mathbf{F}^{\mathrm{T}}, \quad \boldsymbol{\chi}_*^{-1}(\bullet)^{\#} = \mathbf{F}^{-1}(\bullet)^{\#}\mathbf{F}^{-\mathrm{T}}, \tag{2.1}$$

respectively. Here we introduce the local deformation gradient

$$\mathbf{F} = \partial\boldsymbol{\chi}(\mathbf{X}, t)/\partial\mathbf{X}, \tag{2.2}$$

which allows us to map a tangent vector $\mathrm{d}\mathbf{X}$ from the reference configuration to the current configuration by $\mathrm{d}\mathbf{x} = \mathbf{F}\,\mathrm{d}\mathbf{X}$. $\mathbf{F}$ is in general non-symmetric and a two-point tensor, i.e., it has coordinates in two different configurations, namely in both the reference and the current configuration. This can also be seen when writing the transformation of a tangent vector in index notation, $\mathrm{d}x_a = F_{aA}\mathrm{d}X_A$. It is important to note that $\mathbf{F}(\mathbf{X}, t)$ is defined locally, i.e., it describes the motion in the neighborhood of a point. Moreover, the deformation gradient links the material and spatial configuration via a linear transformation. This is very convenient since it allows us to represent the deformation gradient tensor in a given coordinate system by a matrix. The determinant of $\mathbf{F}$ is denoted J and is the ratio between the volume in the current configuration and the reference configuration, $J = \det\mathbf{F} = V/V_0 > 0$. For incompressible materials we require J to be equal to unity. The existence of the inverse mapping $\mathbf{F}^{-1}(\mathbf{x}, t)$ ensures that at a time t a particle cannot occupy two locations in space and that two particles cannot occupy the same location.

[6] We denote contravariant tensors by a superscript $\#$, whereas covariant tensors usually have a superscript $\flat$.

We can decompose the deformation gradient in two parts according to

$$\mathbf{F} = \mathbf{RU} = \mathbf{vR}, \tag{2.3}$$

where $\mathbf{R}$ is a proper[7] ($\det \mathbf{R} = 1$) orthogonal ($\mathbf{R}^{\mathrm{T}} = \mathbf{R}^{-1}$) tensor and $\mathbf{U}$ and $\mathbf{v}$ are the right (material) and left (spatial) stretch tensors, respectively. This multiplicative split of the deformation, also called polar decomposition, is illustrated in Fig. 2.1(b) where we see how the tensors operate on a continuum body: if we apply the rotation $\mathbf{R}$ first, we have to use the left stretch tensor $\mathbf{v}$ to deform the body and if we want to perform the deformation first, the right stretch tensor $\mathbf{U}$ is required. Note that both decompositions involve the same orthogonal rotation tensor $\mathbf{R}$ and that the stretch tensors are symmetric ($\mathbf{U} = \mathbf{U}^{\mathrm{T}}$, $\mathbf{v} = \mathbf{v}^{\mathrm{T}}$).

Since we treat our material as incompressible, we face numerical problems such as ill-conditioning in general and volumetric locking in particular. To avoid these problems, we decouple the pressure field from the displacement field by applying the multiplicative decomposition of $\mathbf{F}$ into a spherical (dilatational, volume changing) part $J^{1/3}\mathbf{I}$ and a unimodular (distortional, volume preserving) part

$$\overline{\mathbf{F}} = J^{-1/3}\mathbf{F}, \tag{2.4}$$

where $\det \overline{\mathbf{F}} = 1$, see [Flory, 1961, Ogden, 1978]. In the following, we denote quantities related to this distortional deformation with a bar or a tilde, depending on the context and operations we perform.

2.2 Strain Measures

To solve the equations describing the deformation of a continuum body, we have to use a constitutive law which provides a relation between stress and strain. But since strain is (as stress) an abstract (arbitrary) quantity, we have to make meaningful definitions which allow us to set up a consistent and physically reasonable framework. As shown in [Holzapfel, 2000], the right Cauchy-Green tensor $\mathbf{C} = \mathbf{F}^{\mathrm{T}}\mathbf{F}$ is a (nonlinear) measure of deformation which is frequently used in continuum mechanics. It is symmetric, positive definite[8] and yields the square of the

[7] An improper orthogonal tensor is characterized by $\det \mathbf{R} = -1$, which represents a reflection.

[8] Positive definite means that $\mathbf{u} \cdot \mathbf{Cu} > 0, \mathbf{u} \neq \mathbf{0}$.

stretch λ of a vector $\mathbf{a}_0$ in the reference configuration by $\lambda^2 = \mathbf{a} \cdot \mathbf{a} = (\mathbf{F}\mathbf{a}_0)^{\mathrm{T}} \cdot (\mathbf{F}\mathbf{a}_0) = \mathbf{a}_0 \cdot \mathbf{C}\mathbf{a}_0$. The diagonal components of $\mathbf{C}$ are the square of the stretches in the respective direction while the off-diagonal components are related to the shear deformations. Moreover, the eigenvalues of $\mathbf{C}$ are the squares of the principal stretches of the continuum body. Note that since $\mathbf{C}$ does not contain rigid body movements like translations or rotations, it is not useful in a constitutive law since it is unity in the state of no deformation. Therefore we introduce the Green-Lagrange strain tensor $\mathbf{E} = \frac{1}{2}(\mathbf{C} - \mathbf{I})$, which is a 'true' strain measure since it equals the zero tensor $\mathbf{O}$ if no deformation is applied to the body. The factor $1/2$ is introduced for consistency with the linear theory[9].

2.3 Forces and Stresses

Stresses are the reaction of a body to externally applied forces. These external forces can either be surface loads (friction, pressure, ...) or body loads (gravity, electromagnetic forces, ...). If we cut a body which is under an external load in the current configuration (see Fig. 2.2, right side) we obtain a surface on which we can define an infinitesimal area element $\mathrm{d}s$ with the unit normal vector $\mathbf{n}$. As a reaction to the externally applied forces, the traction vector $\mathbf{t}$ acts on the oriented surface $\mathrm{d}s$ holding the body in equilibrium. This traction vector $\mathbf{t}$ has the unit force per unit area and is called the Cauchy (or true) traction vector since it is defined in the current configuration. It is named after Augustin-Louis Cauchy (1789-1857) who postulated 1827 one of the most fundamental theorems of continuum mechanics; it introduces the Cauchy stress tensor $\boldsymbol{\sigma}(\mathbf{x}, t)$, a symmetric, second-order tensor field, which relates the normal vector $\mathbf{n}(\mathbf{x}, t)$ to the traction vector $\mathbf{t}(\mathbf{x}, t, \mathbf{n})$ by $\mathbf{t}(\mathbf{x}, t, \mathbf{n}) = \boldsymbol{\sigma}(\mathbf{x}, t)\mathbf{n}$. The fundamental conclusion of this theorem is the linear relationship between the traction vector $\mathbf{t}$ and the unit normal vector $\mathbf{n}$. Since we link two oriented quantities (traction and surface), stress is a tensor of second order [Humphrey, 2002]. Note that the stress tensor is independent of the orientation of the surface but can vary with the location in the body (this is also reflected in the arguments of the stress tensor).

[9] Note that this factor only influences the resulting material parameters. If we choose another factor (or omit it completely), only the parameters determined by fitting the constitutive law would change

The Cauchy stress is the most natural and physical measure of stress since it is defined completely in the deformed configuration and is mostly used in fluid mechanics where the problems are formulated in the spatial setting. In solid mechanics, however, the geometry of the deformed configuration is not known and, therefore, it facilitates the analysis to set up the governing equations of motion and equilibrium in the reference configuration. This leads to the introduction of purely mathematical quantities but simplifies the formulation of equations and their numerical treatment. Since we want to work in the reference configuration, we apply the concepts

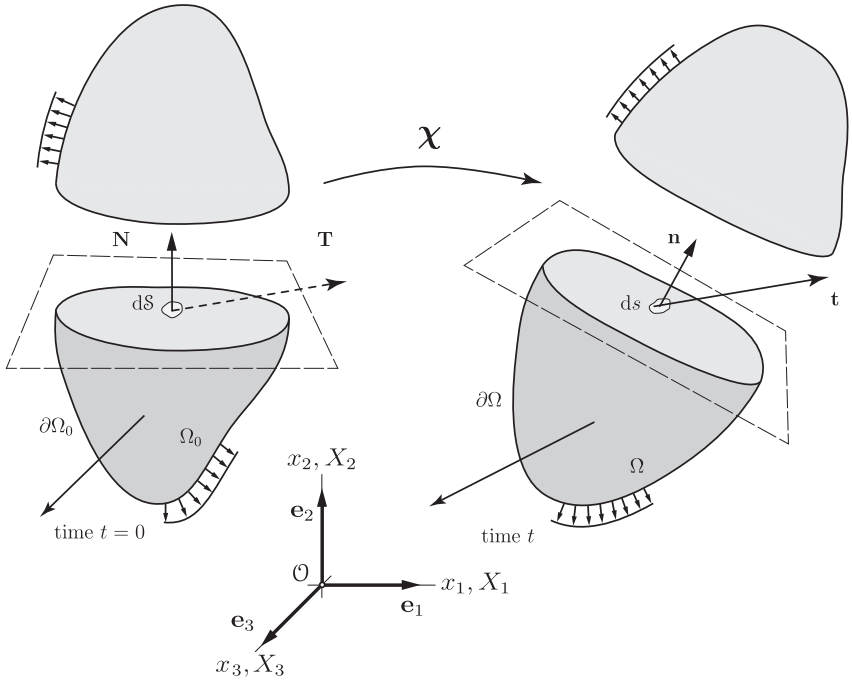

Figure 2.2: A continuum body which is subjected to surface- and body loads. Upon cutting the body open in the current configuration (right side) we can define an area element $\mathrm{d}s$, represented by a unit normal vector **n**, on which the traction vector **t** acts as a reaction to the external forces. The same can be done for the reference configuration (left side), where we define the infinitesimal area element $\mathrm{d}\mathcal{S}$ with the normal vector **N** and the traction vector **t**, mapped by $\mathbf{F}^{-1}$ to the reference configuration yielding **T**. Note that **T** acts on Ω but is a function of **X** and the outward normal **N** to the boundary surface Ω_0, which is indicated by the dashed line.

introduced above to the body in Ω_0 as illustrated in Fig. 2.2 (left side). We map the current traction vector $\mathbf{t}(\mathbf{x}, t, \mathbf{n})$ from its point of application **x** back to the corresponding point **X** in the reference configuration and obtain the first Piola-Kirchhoff (nominal) traction vector $\mathbf{T}(\mathbf{X}, t, \mathbf{N})$ which acts on the unit area element $\mathrm{d}\mathcal{S}$ and points in the same direction as $\mathbf{t}(\mathbf{x}, t, \mathbf{n})$ in the

current configuration. The first Piola-Kirchhoff traction vector has the physical interpretation of current force per unit area in the reference configuration. It is related to the normal vector defining its surface in a similar way as the Cauchy traction vector, namely by a linear mapping $\mathbf{T}(\mathbf{X}, t, \mathbf{N}) = \mathbf{P}(\mathbf{X}, t)\mathbf{N}$, where we introduced the first Piola-Kirchhoff stress tensor $\mathbf{P}(\mathbf{X}, t)$.

The introduced tensor fields, namely $\boldsymbol{\sigma}(\mathbf{x}, t)$ and $\mathbf{P}(\mathbf{X}, t)$, perform the same operation, i.e., they establish a linear relation between a normal vector and the related traction vector. Nevertheless, they live in different coordinate systems since both define a traction vector in the current configuration but act on the unit vector in a different coordinate system. This can also be seen when writing the mapping in index notation as

$$t_a = \sigma_{ab} n_b \quad \text{and} \quad T_a = P_{aB} N_B, \tag{2.5}$$

where we see that $\mathbf{P}$ is, such as $\mathbf{F}$, a two-point tensor living in both the reference and current configuration since it relates $\mathbf{N}$ (at $t = 0$) to the traction vector $\mathbf{T}$ (at time t). Although $\mathbf{P}$ has a physical interpretation, it is not convenient to use since, in general, it is not symmetric. Note that for infinitesimal deformations the first Piola-Kirchhoff stress tensor and the Cauchy stress tensor are identical since in this case the change in cross-sectional area is (nearly) zero. Hence, the first Piola-Kirchhoff stress is the 3D generalization of the concept of 1D engineering stress where the change in cross-sectional area is neglected. Moreover, it is the work conjugate to the deformation gradient $\mathbf{F}$. Using Nanson's formula, relating an infinitesimal area in the current and reference configuration by $\mathrm{d}\mathbf{s} = J\,\mathbf{F}^{-T}\mathrm{d}\mathbf{S}$, we can establish the relation between the first Piola-Kirchhoff stress tensor and the Cauchy stress tensor $\boldsymbol{\sigma} = J^{-1}\mathbf{P}\mathbf{F}^{\mathrm{T}}$, which is called the Piola transform.

The introduced stress measures are useful since the Cauchy stress represents the 'actual stress' experienced by a body and the first Piola-Kirchhoff stress is convenient for experimental measurement. Nevertheless, we introduce two more stress measures: the Kirchhoff stress tensor $\boldsymbol{\tau}$ and the second Piola-Kirchhoff stress tensor $\mathbf{S}$. The first one is required for the finite element implementation of our material law in the software package FEAP and is defined by the volume ratio times the Cauchy stress tensor, $\boldsymbol{\tau} = J\boldsymbol{\sigma}$. Note that $\boldsymbol{\tau}$ lives, like $\boldsymbol{\sigma}$, solely in the current configuration. The second Piola-Kirchhoff stress tensor, in contrast, lives in the reference configuration and is given by the pull-back of $\boldsymbol{\tau}$. Since $\boldsymbol{\tau}$ is a contravariant tensor, the

pull back is, as in eq. (2.1), given by $\mathbf{S} = \boldsymbol{\chi}_*^{-1}(\boldsymbol{\tau}) = \mathbf{F}^{-1}\boldsymbol{\tau}\mathbf{F}^{-\mathrm{T}}$. Consequently, we obtain the Cauchy stress tensor (i.e., the stress in the current configuration) from the (virtual) stress in the reference configuration by $\boldsymbol{\sigma} = J^{-1}\mathbf{F}\mathbf{S}\mathbf{F}^{\mathrm{T}}$. One can also think of **S** as the relation between the area in the reference configuration and a virtual 'force' in the reference configuration $\tilde{\mathbf{T}}$ which is the pull back of **T** by $\mathbf{F}^{-1}$. Hence, the second Piola-Kirchhoff tensor is a one-point tensor defined by $\tilde{\mathbf{T}}(\mathbf{X}, t) = \mathbf{S}\mathbf{N}$ [Humphrey, 2002].

Note that although **S** has no physical interpretation it is a very useful quantity in computational mechanics. It is symmetric and the energetic conjugate to the Green-Lagrange strain tensor **E**, and can be obtained by the derivation of the strain-energy function with respect to the right Cauchy-Green tensor **C**. The second Piola-Kirchhoff stress tensor **S** is a contravariant material tensor field and parameterized by material coordinates. Therefore, it is useful in computational mechanics and for the formulation of constitutive equations of solids. For a rigid body motion we can write $\mathbf{F} = \mathbf{R}$ (according to eq. (2.3)), and, therefore, $\mathbf{S} = \mathbf{R}^{\mathrm{T}}\boldsymbol{\sigma}\mathbf{R}$. This corresponds to a coordinate transformation, i.e., the components of **S** coincide with the ones of $\boldsymbol{\sigma}$ in the global Cartesian coordinate system rotated by **R**. Another useful property of **S** is its invariance to superimposed rotations in the current configuration [Humphrey, 2002].

2.4 Tensor Algebra

We provide a very brief overview over the required results and identities from tensor algebra. For a more extensive and detailed introduction the reader is referred to the standard works of [Ogden, 1974, Holzapfel, 2000].

The Cayley-Hamilton Theorem. This theorem states that every square matrix satisfies its own characteristic equation. To understand this very important theorem, we first have to define the characteristic equation (polynomial) of a square matrix $[\mathbf{A}]$ as $p(\lambda) = \det(\mathbf{A} - \lambda\mathbf{I}) = \lambda^3 - I_1^A\lambda^2 + I_2^A\lambda - I_3^A = 0$, where I_1^A, I_2^A, I_3^A are the three principal invariants[10] of **A**. From the theorem of Cayley-Hamilton follows that

$$\mathbf{A}^3 - I_1^A\mathbf{A}^2 + I_2^A\mathbf{A} - I_3^A = \mathbf{O}, \tag{2.6}$$

[10] Sometimes these invariants are denoted as I^A, II^A, III^A.

and we conclude that every power of $\mathbf{A}$ higher than three can be represented by a combination of $\mathbf{A}, \mathbf{A}^2$ and $\mathbf{A}^3$. This property is very useful to determine the derivatives of the invariants of a tensor and yields

$$\frac{\partial I_1^A}{\partial \mathbf{A}} = \mathbf{I}, \quad \frac{\partial I_2^A}{\partial \mathbf{A}} = I_1^A \mathbf{I} - \mathbf{A}^{\mathrm{T}}. \tag{2.7}$$

We will demonstrate how to derive the third invariant by multiplying eq. (2.6) with $\mathbf{A}^{-1}$, and after rearranging the equation we obtain

$$\mathbf{A}^2 - I_1^A \mathbf{A} + I_2^A = I_3^A \mathbf{A}^{-1}. \tag{2.8}$$

When we take the derivative of eq. (2.6) with respect to $\mathbf{A}$ and compare the result with eq. (2.8), we see that

$$\frac{\partial I_3^A}{\partial \mathbf{A}} = I_3^A \mathbf{A}^{-1}, \tag{2.9}$$

where we used the results of eq. (2.7). The rules of differentiation for the double contraction and a scalar multiplication are given by

$$\frac{\partial (\mathbf{A} : \mathbf{B})}{\partial \mathbf{C}} = \mathbf{A} : \frac{\partial \mathbf{B}}{\partial \mathbf{C}} + \mathbf{B} : \frac{\partial \mathbf{A}}{\partial \mathbf{C}}, \quad \frac{\partial (\alpha \mathbf{A})}{\partial \mathbf{C}} = \mathbf{A} \otimes \frac{\partial \alpha}{\partial \mathbf{C}} + \alpha \frac{\partial \mathbf{A}}{\partial \mathbf{C}}, \tag{2.10}$$

where $\mathbf{A}$, $\mathbf{B}$ and $\mathbf{C}$ are second-order tensors and α is a scalar. For the next step recall eq. (2.9) and the fact that the determinant of the transpose of a matrix equals the determinant of the original matrix, i.e., $J = \det \mathbf{F} = \det \mathbf{F}^{\mathrm{T}}$. So the derivative of J and $J^{-2/3}$ with respect to $\mathbf{C}$ are given by

$$\frac{\partial J}{\partial \mathbf{C}} = \frac{\partial I_3^{1/2}}{\partial \mathbf{C}} = \frac{1}{2} I_3^{-1/2} \frac{\partial I_3}{\partial \mathbf{C}} = \frac{J}{2} \mathbf{C}^{-1}, \qquad \frac{\partial J^{-2/3}}{\partial \mathbf{C}} = -\frac{1}{3} J^{-2/3} \mathbf{C}^{-1}. \tag{2.11}$$

using the chain rule and noting that $I_3 = \det \mathbf{C} = \det \mathbf{F}^{\mathrm{T}} \det \mathbf{F} = J^2$. The derivative of the modified right Cauchy-Green tensor with respect to its normal counterpart is given by

$$\begin{aligned} \frac{\partial \overline{\mathbf{C}}}{\partial \mathbf{C}} &= \frac{\partial (J^{-2/3} \mathbf{C})}{\partial \mathbf{C}} = J^{-2/3} \frac{\partial \mathbf{C}}{\partial \mathbf{C}} + \mathbf{C} \otimes \frac{\partial J^{-2/3}}{\partial \mathbf{C}} = J^{-2/3} \mathbb{I} - \mathbf{C} \otimes \frac{1}{3} J^{-2/3} \mathbf{C}^{-1} \\ &= J^{-2/3} (\mathbb{I} - \frac{1}{3} \mathbf{C} \otimes \mathbf{C}^{-1}) = J^{-2/3} \mathbb{P}^{\mathrm{T}}, \end{aligned} \tag{2.12}$$

with the definition of the projection tensor $\mathbb{P}$ in the Lagrangian setting

$$\mathbb{P} = \mathbb{I} - \frac{1}{3} \mathbf{C}^{-1} \otimes \mathbf{C}, \tag{2.13}$$

which provides the correct deviatoric projection in the Lagrangian setting, i.e., $[\mathbb{P} : (\bullet)] : \mathbf{C} = 0$. Note that $\mathbb{P}$ is the pull-back of the spatial deviatoric operator [Federico and Grillo, 2012] where $\mathbf{C}$ operates as a metric tensor [Holzapfel, 1996]. Finally, we can also differentiate $\mathbf{C}$ with respect to $\overline{\mathbf{C}}$ finding that

$$\frac{\partial \mathbf{C}}{\partial \overline{\mathbf{C}}} = J^{2/3}\mathbb{I}, \tag{2.14}$$

where $\mathbb{I}$ is a fourth-order identity tensor.

2.5 The Strain-Energy Function

We work in the context of finite hyperelasticity and, therefore, assume the existence of a scalar strain-energy function Ψ from which we can derive the constitutive equation relating stress and strain. This strain-energy function depends on a measure of deformation, for example $\Psi = \Psi(\mathbf{F})$. Note that we omitted the dependency on the position within the material, so we assume a homogeneous material where the strain-energy is the same at every point. For a detailed description of hyperelasticity and related topics such as (poly)convexity see e.g., [Holzapfel, 2000, Holzapfel et al., 2000, 2004].

The strain-energy function has to fulfill certain requirements to be physically meaningful. For example, it is not allowed to compress the body to a point or extend it to infinite volume, therefore the energy required to perform such operations should be infinite, i.e.

$$\begin{aligned} \Psi(\mathbf{F}) &\to \infty \quad \text{for} \quad \det \mathbf{F} \to \infty, \\ \Psi(\mathbf{F}) &\to \infty \quad \text{for} \quad \det \mathbf{F} \to +0. \end{aligned} \tag{2.15}$$

Moreover, the strain-energy in a state of no deformation should be zero, $\Psi(\mathbf{I}) = 0$, and the strain-energy should increase with deformation, $\Psi(\mathbf{F}) \geq 0$.

We can derive the constitutive equation for the stress by taking the derivative of the strain-energy function with respect to the deformation gradient,

$$\mathbf{P} = \frac{\partial \Psi(\mathbf{F})}{\partial \mathbf{F}}, \quad \mathbf{S} = 2\frac{\partial \Psi(\mathbf{C})}{\partial \mathbf{C}}. \tag{2.16}$$

The strain-energy should not change upon a rigid body rotation applied after the deformation, i.e., $\Psi(\mathbf{QF}) = \Psi(\mathbf{F})$ where $\mathbf{Q}$ is a proper orthogonal tensor. If we choose $\mathbf{Q} = \mathbf{R}^{\mathrm{T}}$ and use the

polar decomposition of **F**, i.e.

$$\Psi(\mathbf{R}^{\mathrm{T}}\mathbf{F}) = \Psi(\mathbf{R}^{\mathrm{T}}\mathbf{R}\mathbf{U}) = \Psi(\mathbf{U}). \tag{2.17}$$

Hence, the strain-energy does only depend on the stretching part of **F** and is not affected by any rigid body rotation $\mathbf{R}^{\mathrm{T}}$. The specific choice of the strain-energy function determines the constitutive material behavior and is, therefore, essential for a material model. In chapter 5, we will present an anisotropic, nonlinear strain-energy function which includes fiber dispersion in two planes and allows for an efficient finite element implementation.

Split of the Strain-Energy Function. We assume that it is possible to split the strain-energy function in two parts like

$$\Psi = \Psi_{\mathrm{vol}}(J) + \bar{\Psi}(\overline{\mathbf{C}}), \tag{2.18}$$

as shown in [Holzapfel, 2000]. Here, $\Psi_{\mathrm{vol}}(J)$ is a purely volumetric contribution while $\bar{\Psi}(\overline{\mathbf{C}})$ represents the energy contribution of an isochoric (volume preserving) deformation. As introduced in eq. $(2.16)_2$, the second Piola-Kirchhoff stress tensor **S** is the change of the strain-energy function with respect to the right Cauchy-Green tensor, $\mathbf{S} = 2\partial\Psi(\mathbf{C})/\partial\mathbf{C}$, and using the decoupled form of the strain-energy function Ψ we identify two stress contributions $\mathbf{S} = \mathbf{S}_{\mathrm{vol}} + \overline{\mathbf{S}}$. By virtue of eq. (2.9) and the chain rule we find for the volumetric part

$$\mathbf{S}_{\mathrm{vol}} = 2\frac{\partial\Psi_{\mathrm{vol}}(J)}{\partial\mathbf{C}} = 2\frac{\partial\Psi_{\mathrm{vol}}(J)}{\partial J}\frac{\partial J}{\partial\mathbf{C}} = pJ\mathbf{C}^{-1}, \tag{2.19}$$

where the hydrostatic pressure p for incompressible materials is defined by

$$p = \frac{\partial\Psi_{\mathrm{vol}}(J)}{\partial J}. \tag{2.20}$$

Using eq. (2.12) we obtain for the isochoric part

$$\begin{aligned}\overline{\mathbf{S}} &= 2\frac{\partial\bar{\Psi}(\overline{\mathbf{C}})}{\partial\mathbf{C}} = 2\frac{\bar{\Psi}(\overline{\mathbf{C}})}{\partial\overline{\mathbf{C}}} : \frac{\partial\overline{\mathbf{C}}}{\partial\mathbf{C}} = \tilde{\mathbf{S}} : J^{-2/3}(\mathbb{I} - \frac{1}{3}\mathbf{C}\otimes\mathbf{C}^{-1}) \\ &= J^{-2/3}\mathbb{P} : \tilde{\mathbf{S}} = J^{-2/3}\mathrm{Dev}\,\tilde{\mathbf{S}},\end{aligned} \tag{2.21}$$

where $\tilde{\mathbf{S}}$ is the fictitious second Piola-Kirchhoff stress tensor defined as

$$\tilde{\mathbf{S}} = 2\frac{\partial\bar{\Psi}(\overline{\mathbf{C}})}{\partial\overline{\mathbf{C}}}. \tag{2.22}$$

We see that the isochoric stress is the deviator of the fictitious stress multiplied with $J^{-2/3}$ and $(\mathbb{I})_{ABCD} = \frac{1}{2}(\delta_{AC}\delta_{BD} + \delta_{AD}\delta_{BC})$ is a fourth-order identity tensor. Using the decomposition of the deformation gradient given in eq. (2.4), we define the modified right Cauchy-Green tensor as $\overline{\mathbf{C}} = \overline{\mathbf{F}}^{\mathrm{T}}\overline{\mathbf{F}}$.

To utilize the finite element method, we require the Kirchhoff stress tensor $\boldsymbol{\tau}$ which is the push-forward of $\mathbf{S}$, and hence given by $\boldsymbol{\tau} = \mathbf{F}\mathbf{S}\mathbf{F}^{\mathrm{T}} = \boldsymbol{\tau}_{\mathrm{vol}} + \overline{\boldsymbol{\tau}}$ where we introduced

$$\boldsymbol{\tau}_{\mathrm{vol}} = pJ\,\mathbf{I}, \quad \overline{\boldsymbol{\tau}} = \mathrm{dev}\ \tilde{\boldsymbol{\tau}} = \mathbb{P} : \tilde{\boldsymbol{\tau}} \quad \text{with} \quad \mathbb{P} = \mathbb{I} - \frac{1}{3}\mathbf{I} \otimes \mathbf{I}, \tag{2.23}$$

where $\mathbb{P}$ is the Eulerian projection tensor and $\tilde{\boldsymbol{\tau}}$ is the push forward of the fictitious second Piola-Kirchhoff tensor given in eq. (2.22).

2.6 Elasticity Tensors

Since the relation between the stress tensor $\mathbf{S}$ and the tensor $\mathbf{C}$ will be nonlinear, a Newton-Raphson-like iteration process is required to solve for an incremental displacement. Therefore, we have to linearize eq. $(2.16)_2$ where we introduced the Lagrangian elasticity tensor $\mathbb{C}$ using the total differential of the second Piola-Kirchhoff stress tensor $\mathbf{S}$, i.e.

$$\mathrm{d}\mathbf{S} = \mathbb{C} : \frac{1}{2}\mathrm{d}\mathbf{C}, \quad \text{with} \quad \mathbb{C} = 2\frac{\partial \mathbf{S}}{\partial \mathbf{C}} = 4\frac{\partial^2 \Psi(\mathbf{C})}{\partial \mathbf{C}^2}. \tag{2.24}$$

Note that the matrix representation of the elasticity tensor in the respective coordinate system is the tangent modulus required for the implementation of a nonlinear finite element code. Since the differentiation in eq. $(2.24)_2$ with respect to $\mathbf{C}$ has to fulfill Schwarz's theorem, $\mathbb{C}$ features major symmetries, i.e., $\mathbb{C}_{ABCD} = \mathbb{C}_{CDAB}$. Moreover, $\mathbf{C}$ is symmetric, also introducing minor symmetries, i.e., $\mathbb{C}_{ABCD} = \mathbb{C}_{ABDC} = \mathbb{C}_{BACD} = \mathbb{C}_{BADC}$. This allows to write the symmetric forth-order elasticity tensor in matrix representation (thereby reducing its order) using Voigt notation, so we can write $\mathbb{C}$ as a symmetric 6×6 matrix. This can be imagined as a 'mapping' of indices as

$$\{11\} \to \{1\}, \{22\} \to \{2\}, \{33\} \to \{3\}, \{12, 21\} \to \{4\}, \{23, 32\} \to \{5\}, \{31, 13\}. \to \{6\}.$$

Hence, the tangent matrix (in Voigt notation) passed to FEAP looks like this:

$$[\mathbb{C}^{\mathrm{Voigt}}] = \begin{bmatrix} C_{1111} & C_{1122} & C_{1133} & C_{1112} & C_{1113} & C_{1123} \\ & C_{2222} & C_{2233} & C_{2212} & C_{2213} & C_{2223} \\ & & C_{3333} & C_{3312} & C_{3313} & C_{3323} \\ & & & C_{1212} & C_{1213} & C_{1223} \\ & \text{sym.} & & & C_{1313} & C_{1323} \\ & & & & & C_{2323} \end{bmatrix}. \tag{2.25}$$

With this representation of the indices, the second-order stress tensor $\boldsymbol{\sigma}$ can be written as a column matrix

$$[\boldsymbol{\sigma}^{\mathrm{Voigt}}] = [\sigma_{11} \quad \sigma_{22} \quad \sigma_{33} \quad \sigma_{12} \quad \sigma_{23} \quad \sigma_{31}]^{\mathrm{T}}, \tag{2.26}$$

and similarly the second order strain tensor $\boldsymbol{\epsilon}$ as

$$[\boldsymbol{\epsilon}^{\mathrm{Voigt}}] = [\epsilon_{11} \quad \epsilon_{22} \quad \epsilon_{33} \quad 2\epsilon_{12} \quad 2\epsilon_{23} \quad 2\epsilon_{31}]^{\mathrm{T}}. \tag{2.27}$$

Note that the factor 2 appears to make the shear components ϵ_{ij} the engineering strains γ_{ij} [Taylor, 2000].

The Elasticity Tensor in the Lagrangian Description. We will derive a general expression for the elasticity tensor in the Lagrangian setting for a hyperelastic material. For this purpose, we split the strain-energy function, according to eq. (2.18), into a volumetric and a deviatoric part and consequently use the volumetric and deviatoric second Piola-Kirchhoff stress tensors.

Equipped with the definitions from section 2.4 we start with the split of the strain-energy function eq. (2.18)), and hence the split of the elasticity tensor like $\mathbb{C} = \mathbb{C}_{\mathrm{vol}} + \overline{\mathbb{C}}$, where the volumetric part is given by

$$\begin{aligned} \mathbb{C}_{\mathrm{vol}} &= 4\frac{\partial^2 \Psi_{\mathrm{vol}}}{\partial \mathbf{C}^2} = 2\frac{\partial \mathbf{S}_{\mathrm{vol}}}{\partial \mathbf{C}} = 2\frac{(Jp\mathbf{C}^{-1})}{\partial \mathbf{C}} = 2\mathbf{C}^{-1} \otimes \frac{\partial (Jp)}{\partial \mathbf{C}} + 2Jp\frac{\partial \mathbf{C}^{-1}}{\partial \mathbf{C}} \\ &= 2\mathbf{C}^{-1} \otimes \left(p\frac{\partial J}{\partial \mathbf{C}} + J\frac{\partial p}{\partial \mathbf{C}} \right) - 2Jp\mathbf{C}^{-1} \odot \mathbf{C}^{-1} \end{aligned} \tag{2.28}$$

where we introduced a new tensor product

$$\frac{\partial \mathbf{C}^{-1}}{\partial \mathbf{C}} = -\mathbf{C}^{-1} \odot \mathbf{C}^{-1}.$$

which is defined as

$$-(\mathbf{C}^{-1}\odot\mathbf{C}^{-1})_{ABCD}=-\frac{1}{2}(C^{-1}_{AC}C^{-1}_{BD}+C^{-1}_{AD}C^{-1}_{BC})=\frac{\partial C^{-1}_{AB}}{\partial C_{CD}}.$$

We can simplify $\mathbb{C}_{\text{vol}}$ further according to

$$\begin{aligned}\mathbb{C}_{\text{vol}}&=2\mathbf{C}^{-1}\otimes\left[p\frac{\partial J}{\partial\mathbf{C}}+J\frac{\partial p}{\partial J}\frac{\partial J}{\partial\mathbf{C}}\right]-2Jp\mathbf{C}^{-1}\odot\mathbf{C}^{-1} &(2.29)\\ &=J\mathbf{C}^{-1}\otimes\left[\big(p+J\frac{\partial p}{\partial J}\big)\mathbf{C}^{-1}\right]-2Jp\mathbf{C}^{-1}\odot\mathbf{C}^{-1}\\ &=J\tilde{p}\mathbf{C}^{-1}\otimes\mathbf{C}^{-1}-2Jp\mathbf{C}^{-1}\odot\mathbf{C}^{-1}, &(2.30)\end{aligned}$$

where we introduced the definition $\tilde{p}=p+J{}^{\partial p}/_{\partial J}$, where ${}^{\partial p}/_{\partial J}={}^{\partial^2\Psi_{\text{vol}}}/_{\partial J^2}$. For the isochoric elasticity tensor we get

$$\overline{\mathbb{C}}=2\frac{\partial\overline{\mathbf{S}}}{\partial\mathbf{C}}=2\frac{\partial J^{-2/3}\mathbb{P}:\tilde{\mathbf{S}}}{\partial\mathbf{C}}=2(\mathbb{P}:\tilde{\mathbf{S}})\otimes\frac{\partial J^{-2/3}}{\partial\mathbf{C}}+2J^{-2/3}\frac{\partial(\mathbb{P}:\tilde{\mathbf{S}})}{\partial\mathbf{C}},\tag{2.31}$$

where we split the expression in two parts, $\overline{\mathbb{C}}_1$ and $\overline{\mathbb{C}}_2$. The first expression is given by

$$\overline{\mathbb{C}}_1=2(\mathbb{P}:\tilde{\mathbf{S}})\otimes\frac{\partial J^{-2/3}}{\partial\mathbf{C}}=-\frac{2}{3}(J^{-2/3}\mathbb{P}:\tilde{\mathbf{S}})\otimes\mathbf{C}^{-1}=-\frac{2}{3}\overline{\mathbf{S}}\otimes\mathbf{C}^{-1},\tag{2.32}$$

but the second term is a bit more complicated and reads as

$$\begin{aligned}\overline{\mathbb{C}}_2&=2J^{-2/3}\frac{\partial(\mathbb{P}:\tilde{\mathbf{S}})}{\partial\mathbf{C}}=2J^{-2/3}\frac{\partial}{\partial\mathbf{C}}\left(\tilde{\mathbf{S}}-\frac{1}{3}(\mathbf{C}^{-1}\otimes\mathbf{C}):\tilde{\mathbf{S}}\right)\\ &=2J^{-2/3}\left(\frac{\partial\tilde{\mathbf{S}}}{\partial\overline{\mathbf{C}}}-\frac{1}{3}\frac{\partial(\mathbf{C}^{-1}\otimes\mathbf{C}):\tilde{\mathbf{S}}}{\partial\overline{\mathbf{C}}}\right):\frac{\partial\overline{\mathbf{C}}}{\partial\mathbf{C}}\\ &=2J^{-2/3}\left(\frac{\partial\tilde{\mathbf{S}}}{\partial\overline{\mathbf{C}}}-\frac{1}{3}\frac{\partial(\tilde{\mathbf{S}}:\mathbf{C})\mathbf{C}^{-1}}{\partial\overline{\mathbf{C}}}\right):\frac{\partial\overline{\mathbf{C}}}{\partial\mathbf{C}}=\left[\tilde{\mathbb{C}}-\frac{1}{3}(\mathbb{X}+\mathbb{Y})\right]:\mathbb{P}^{\mathrm{T}},\end{aligned}\tag{2.33}$$

which motivates the definition of the fictitious elasticity tensor in the material configuration

$$\tilde{\mathbb{C}}=2J^{-4/3}\frac{\partial\overline{\mathbf{S}}}{\partial\overline{\mathbf{C}}},\tag{2.34}$$

and the introduction of two more terms, $\mathbb{X}$ and $\mathbb{Y}$, given by

$$\begin{aligned}\mathbb{X}&=2J^{-4/3}\mathbf{C}^{-1}\otimes\frac{\partial(\tilde{\mathbf{S}}:\mathbf{C})}{\partial\overline{\mathbf{C}}}=2J^{-4/3}\mathbf{C}^{-1}\otimes\left(\tilde{\mathbf{S}}:\frac{\partial\mathbf{C}}{\partial\overline{\mathbf{C}}}+\mathbf{C}:\frac{\partial\tilde{\mathbf{S}}}{\partial\overline{\mathbf{C}}}\right)\\ &=\mathbf{C}^{-1}\otimes\Big(\mathbf{C}:\tilde{\mathbb{C}}+2J^{-2/3}\tilde{\mathbf{S}}\Big)=\mathbf{C}^{-1}\otimes\mathbf{C}:\tilde{\mathbb{C}}+2\mathbf{C}^{-1}\otimes J^{-2/3}\tilde{\mathbf{S}}.\end{aligned}\tag{2.35}$$

For the second part we have

$$\begin{aligned}\mathbb{Y} &= 2J^{-2/3}(\tilde{\mathbf{S}} : \mathbf{C})\frac{\partial \mathbf{C}^{-1}}{\partial \overline{\mathbf{C}}}J^{-2/3} = 2J^{-4/3}(\tilde{\mathbf{S}} : \mathbf{C})J^{2/3}\frac{\partial \mathbf{C}^{-1}}{\partial \mathbf{C}} \\ &= -2J^{-2/3}(\tilde{\mathbf{S}} : \mathbf{C})\mathbf{C}^{-1} \odot \mathbf{C}^{-1}. \end{aligned} \tag{2.36}$$

This allows us to finally write the second part of the isochoric elasticity tensor as

$$\begin{aligned}\overline{\mathbb{C}}_2 &= 2J^{-2/3}\frac{\partial(\mathbb{P} : \tilde{\mathbf{S}})}{\partial \mathbf{C}} = \left(\mathbb{I} - \frac{1}{3}\mathbf{C}^{-1} \otimes \mathbf{C}\right) : \tilde{\mathbb{C}} : \mathbb{P}^{\mathrm{T}} - \\ &\quad \frac{2}{3}\mathbf{C}^{-1} \otimes J^{-2/3}\tilde{\mathbf{S}} : \mathbb{P}^{\mathrm{T}} + \frac{2}{3}J^{-2/3}(\overline{\mathbf{S}} : \mathbf{C})\mathbf{C}^{-1} \odot \mathbf{C}^{-1} : \mathbb{P}^{\mathrm{T}} \\ &= \mathbb{P} : \tilde{\mathbb{C}} : \mathbb{P}^{\mathrm{T}} - \frac{2}{3}\mathbf{C}^{-1} \otimes \overline{\mathbf{S}} + \\ &\quad \frac{2}{3}\mathrm{Tr}\left(J^{-2/3}\tilde{\mathbf{S}}\right)\left(\mathbf{C}^{-1} \odot \mathbf{C}^{-1} - \frac{1}{3}(\mathbf{C}^{-1} \odot \mathbf{C}^{-1}) : (\mathbf{C} \otimes \mathbf{C}^{-1})\right) \\ &= \mathbb{P} : \tilde{\mathbb{C}} : \mathbb{P}^{\mathrm{T}} - \frac{2}{3}\mathbf{C}^{-1} \otimes \overline{\mathbf{S}} + \frac{2}{3}\mathrm{Tr}\left(J^{-2/3}\tilde{\mathbf{S}}\right)\tilde{\mathbb{P}}, \end{aligned} \tag{2.37}$$

where we defined the trace in the material coordinates using the right Cauchy-Green tensor as the metric tensor in the Lagrangian setting as $\mathrm{Tr}\,(\bullet) = (\bullet) : \mathbf{C}$.

Moreover, we simplify

$$\begin{aligned}&(\mathbf{C}^{-1} \odot \mathbf{C}^{-1}) : (\mathbf{C} \otimes \mathbf{C}^{-1}) = \mathbf{C}^{-1} \otimes \mathbf{C}^{-1}, \\ &\frac{1}{2}(C^{-1}_{AC}C^{-1}_{BD} + C^{-1}_{AD}C^{-1}_{BC})_{ABCD}(C_{CD}C^{-1}_{EF})_{CDEF} = \\ &\frac{1}{2}(C^{-1}_{AC}C_{CD}C^{-1}_{BD}C^{-1}_{EF} + C^{-1}_{BC}C_{CD}C^{-1}_{AD}C^{-1}_{EF}) = (C^{-1}_{AD}C^{-1}_{EF})_{ADEF}, \end{aligned} \tag{2.38}$$

following from index notation and using eq. (2.29) and further used the modified fourth-order projection tensor in the reference configuration given by

$$\tilde{\mathbb{P}} = \mathbf{C}^{-1} \odot \mathbf{C}^{-1} - \frac{1}{3}\mathbf{C}^{-1} \otimes \mathbf{C}^{-1}. \tag{2.39}$$

By combining eqs. (2.31), (2.32), (2.37), we finally obtain the elasticity tensor in the Lagrangian description according to

$$\overline{\mathbb{C}} = \mathbb{P} : \tilde{\mathbb{C}} : \mathbb{P}^{\mathrm{T}} + \frac{2}{3}\mathrm{Tr}\left(J^{-2/3}\tilde{\mathbf{S}}\right)\tilde{\mathbb{P}} - \frac{2}{3}\left(\mathbf{C}^{-1} \otimes \overline{\mathbf{S}} + \overline{\mathbf{S}} \otimes \mathbf{C}^{-1}\right), \tag{2.40}$$

where we used the fictitious elasticity tensor $\tilde{\mathbb{C}}$ given in eq. (2.34).

The Elasticity Tensor in the Eulerian Setting. After deriving the elasticity tensor in the Lagrangian setting, we have to perform a push forward to obtain the Eulerian description of the elasticity tensor by

$$\begin{aligned} \mathbb{c} &= (\mathbf{F} \otimes \mathbf{F}) : \mathbb{C} : (\mathbf{F} \otimes \mathbf{F})^{\mathrm{T}}, \\ \mathbb{c}_{ijkl} &= F_{iI} F_{jJ} F_{kK} F_{lL} \mathbb{C}_{IJKL}. \end{aligned} \tag{2.41}$$

When we perform the push-forward of eq. (2.40) we obtain the spatial elasticity tensor as $\mathbb{c} = \mathbb{c}_{\mathrm{vol}} + \overline{\mathbb{c}}$ with

$$\mathbb{c}_{\mathrm{vol}} = J(\tilde{p}\mathbf{I} \otimes \mathbf{I} - 2p\mathbb{I}), \quad \overline{\mathbb{c}} = \mathbb{P} : \tilde{\mathbb{c}} : \mathbb{P} + \frac{2}{3}\mathrm{tr}\,(\tilde{\boldsymbol{\tau}})\mathbb{P} - \frac{2}{3}(\mathbf{I} \otimes \overline{\boldsymbol{\tau}} + \overline{\boldsymbol{\tau}} \otimes \mathbf{I}), \tag{2.42}$$

where $\tilde{\mathbb{c}}$ is the fictitious elasticity tensor in the Eulerian setting and given by the push-forward of $\tilde{\mathbb{C}}$.

2.7 Anisotropy for Finite Deformations

We know from histological experiments that the artery is a fiber reinforced material, and mechanical tests have shown that the collagen fibers play a dominant role in the mechanical behavior in the physiological and supra-physiological loading domain. Therefore, we seek to model the artery as an anisotropic material, i.e., we have to account for the directional dependence of the material behavior. There are two ways to do that, namely (i) restrict the way in which the SEF depends on the deformation [Green and Adkins, 1970] or (ii) introduce a vector field which represents the preferred direction of the material explicitly in the SEF [Simo et al., 1985]. Since the first approach requires to perform the computations in the local coordinate system aligned with the preferred direction, we use the second method to model anisotropy [Weiss et al., 1996]. This is especially convenient since the fiber orientation might depend on the position and we might encounter more than one fiber family, therefore it is advantageous that the formulation does not depend on a particular choice of the coordinate system. In a pioneering paper [Spencer, 1984], Spencer introduced five scalar invariants to model a material reinforced with one perfectly aligned fiber family. In the following, we want to give a short overview of his work.

We define a unit vector $\mathbf{M}$ representing the fiber direction in the undeformed configuration enclosing an angle α with the 1-axis of our coordinate system. If the fibers are the only quantities introducing anisotropy, the SEF must not change if both the deformation field $\mathbf{C}$ and the fibers $\mathbf{M}$ are rotated by an orthogonal rotation tensor $\mathbf{Q}$, and we therefore require $\Psi(\mathbf{C}, \mathbf{M}) = \Psi(\mathbf{Q}\mathbf{C}\mathbf{Q}^{\mathrm{T}}, \mathbf{Q}\mathbf{M})$. This states that Ψ is an isotropic invariant of $\mathbf{M}$ and $\mathbf{C}$. Since the sense of $\mathbf{M}$ is not important, Ψ must be an even function of $\mathbf{M}$, i.e., $\Psi(\mathbf{C}, \mathbf{M}) = \Psi(\mathbf{C}, -\mathbf{M})$, and hence Ψ can be expressed as an isotropic invariant of $\mathbf{C}$ and $\mathbf{M} \otimes \mathbf{M}$. This leads to the following set of invariants of $\mathbf{C}$ and $\mathbf{M}$:

$$
\begin{aligned}
&I_1^C = \operatorname{tr}(\mathbf{C}), \quad I_2^C = \tfrac{1}{2}[(\operatorname{tr}(\mathbf{C}))^2 - \operatorname{tr}(\mathbf{C}^2)], \quad I_3^C = \det \mathbf{C}, \\
&I_4^{C,M} = \mathbf{M} \cdot \mathbf{C}\mathbf{M} = \mathbf{C} : (\mathbf{M} \otimes \mathbf{M}), \quad I_5^{C,M} = \mathbf{M} \cdot \mathbf{C}^2\mathbf{M} = \mathbf{C}^2 : (\mathbf{M} \otimes \mathbf{M}),
\end{aligned} \tag{2.43}
$$

where the invariants $I_4^{C,M}$ and $I_5^{C,M}$ are directional since they are related to the direction of the fiber reinforcement. They are also called mixed invariants because they are defined by the tensor fields $\mathbf{C}$ and $\mathbf{M}$. For a more convenient notation, we drop the superscripts of the invariants for the rest of this work since we will solely use the invariants defined by $\mathbf{C}$ and $\mathbf{M}$.

It is not possible to distinguish the effects of the invariants I_4 and I_5, which is problematic for the determination of material parameters. Therefore, we will drop the fifth invariant I_5.

Experiments of [Schriefl et al., 2012d] have verified the assumption that there are two fiber families in the aorta, and since our model aim to capture histological observations as good as possible we have to introduce a second vector field, $\mathbf{M}'$, representing the second fiber family in our model. Because we dropped the invariant quadratic in $\mathbf{C}$ for the first fiber family, we do the same for the second fiber family and obtain two new invariants, namely

$$
I_6 = \mathbf{C} : (\mathbf{M}' \otimes \mathbf{M}'), \quad I_8 = \mathbf{M} \cdot \mathbf{C}^2\mathbf{M}' = \mathbf{C}^2 : (\mathbf{M} \otimes \mathbf{M}'), \tag{2.44}
$$

where I_6 corresponds to I_4 and I_8 is a new invariant accounting for the coupling between the fiber families. We drop I_8 for the same reasons as we neglected I_5 and finally obtain a set of three isotropic invariants and two directional invariants for our two fiber family model. We furthermore assume that the two fiber families feature the same mechanical properties and therefore the SEF Ψ must be symmetric with respect to interchanges of $\mathbf{M}$ and $\mathbf{M}'$.

If a fiber-reinforced body undergoes a deformation described by the deformation gradient **F**, the fibers, i.e., the field of unit vectors **M**, are moved with the particles of the body. The fibers in the deformed configuration are represented by the vector field

$$\mathbf{m} = \mathbf{FM}, \tag{2.45}$$

where the square of the stretch of a fiber is given by

$$\begin{aligned} \lambda_{\mathrm{f}}^2 &= \mathbf{m}^{\mathrm{T}} \cdot \mathbf{m} = \mathbf{MF}^{\mathrm{T}} \cdot \mathbf{FM} = \mathbf{M} \cdot \mathbf{CM} = \mathbf{C} : (\mathbf{M} \otimes \mathbf{M}) = I_4, \\ \lambda_{\mathrm{f}}^2 &= m_a m_a = F_{ab} M_b F_{ac} M_c = M_b C_{bc} M_c = C_{bc} M_b M_c = I_4, \end{aligned} \tag{2.46}$$

showing that the square root of the forth invariant is the fiber stretch, i.e., $\sqrt{I_4} = \lambda_{\mathrm{f}}$.

3 Existing Fiber Dispersion Models

'*Whenever a theory appears to you as the only possible one, take this as a sign that you have neither understood the theory nor the problem which it was intended to solve.*'

KARL POPPER

Modeling of fiber dispersion in soft biological tissues has been an active area of research in the last three decades. To the knowledge of the author, Lanir was the first who considered fiber dispersion in the analysis of fibrous connective tissues [Lanir, 1983]. In this paper he incorporates a probability density function (PDF, also called (fiber) dispersion function) in the strain-energy function to describe the statistical distribution of fibers. Based on his pioneering work, other researchers came up with many different forms for this function, e.g., some models use a discrete approach while others use a continuous distribution. To account for the fiber dispersion in a mechanical model, the PDF can either be (i) incorporated in the strain-energy function (requiring the angular integration of the SEF) or (ii) be integrated separately ('in advance') to obtain a generalized structure tensor representing the fiber dispersion. These two approaches, which we will refer to as angular integration (AI) and generalized structure tensor (GST), are not mutually exclusive since one model can be implemented in both ways; e.g., [Cortes et al., 2010] compared the two formulations for the well-known model proposed by [Gasser et al., 2006]. In general, the GST models use average stretches rather than the actual stretch in the fibers to compute the strain-energy and stress.

Dispersion models can also be classified according to the PDF representing the fiber dispersion: (i) planar distributions with only one parameter can represent either a two-dimensional

(planar) fiber distribution or represent a three-dimensional dispersion which is rotationally symmetric (transverse isotropy), whereas (ii) fully three dimensional fiber dispersion models use PDFs with two or more dispersion parameters to represent an, e.g., orthotropic fiber dispersion.

In this section we review some of the most popular models which incorporate fiber dispersion in soft biological tissues. Since this thesis is based on the papers of [Holzapfel et al., 2000, Gasser et al., 2006], we will discuss their approaches in more detail, and although the work by Fung does not consider fiber dispersion, we will give a short overview of his model since it inspired many subsequent researchers.

3.1 The Work of Fung

In his landmark paper [Fung, 1967], Fung showed the highly nonlinear stess-stretch behavior of mesentary tissue in uniaxial tension tests by measuring the stretch λ_1 and the corresponding first Piola-Kirchhoff stress P_{11}. When plotting the 'stiffness' $\mathrm{d}P_{11}/\mathrm{d}\lambda_1$ against P_{11}, he found a linear relationship, i.e., $\mathrm{d}P_{11}/\mathrm{d}\lambda_1 = c_1 P_{11} + c_2$, with c_1 and c_2 as material parameters. This differential equation suggests an exponential relationship between stress and stretch, and has the solution

$$P_{11} = \frac{c_2}{c_1}\Big\{ \exp[c_1(\lambda_1 - 1)] - 1\Big\}, \tag{3.1}$$

where a stress-free state for zero deformation, i.e., $P_{11} = 0$ for $\lambda_1 = 1$, was assumed. Although this formulation is one-dimensional, it is of fundamental importance and leads to another postulate by Fung where he introduces a SEF which is exponential in terms of the Green-Lagrange strain tensor and reads in its general formulation as

$$\Psi = c[\exp(Q(\mathbf{E})) - 1], \quad \text{and hence} \quad \mathbf{S} = c\exp(Q(\mathbf{E}))\frac{\partial Q(\mathbf{E})}{\partial \mathbf{E}}, \tag{3.2}$$

where he used eq. (2.16) and **E** instead of **C**. Here, the form of Q determines the material behavior and can be taken as, for example, a polynomial function of the components of the Green-Lagrange strain tensor **E**, where $Q = \frac{1}{2}c_{ABCD}E_{AB}E_{CD}$. A quadratic form (as seen in linearly elastic behavior[1]) was shown to be sufficient to describe a wide range of materials.

[1] Note that only Q is quadratic, but the strain-energy function is an exponential function with Q as the argument.

Moreover, it is possible to include anisotropy in this framework as shown by [Holzapfel et al., 2000, Humphrey, 2002].

3.2 Constitutive Model with Perfectly Aligned Fibers

The model of [Holzapfel et al., 2000] uses a strain-energy function which has been extended to include fiber dispersion in various follow-up papers of the same group and other researchers. In [Holzapfel et al., 2000], the authors model the isotropic non-collagenous groundmatrix with a neo-Hookean potential given by

$$\bar{\Psi}_{\mathrm{gm}} = \frac{1}{2} c(\bar{I}_1 - 3), \tag{3.3}$$

where $\bar{I}_1 = \mathrm{tr}\,\overline{\mathbf{C}}$ it the first invariant of the modified right Cauchy-Green tensor. To represent the collagen fibers, the researchers introduce an exponential function which accounts for the non-linear stiffening of arteries at high loads. The strain-energy function for one perfectly aligned collagen fiber family reads as

$$\bar{\Psi}_{\mathrm{f}} = \frac{k_1}{2k_2} \Big\{ \exp[k_2(\bar{I}_i - 1)^2] - 1 \Big\}, \quad i = 4, 6, \tag{3.4}$$

where $\bar{I}_i$ is the modified fourth invariant of $\overline{\mathbf{C}}$ and the structure tensor $\mathbf{H}_i$ (see eq. (2.43), where $\mathbf{M}_i \otimes \mathbf{M}_i = \mathbf{H}_i$), introducing the anisotropy. For each fiber family $i = 4, 6$, this energy is added to the neo-Hookean potential.

3.3 Fiber Model with Rotationally Symmetric Dispersion

In [Gasser et al., 2006], the authors assume a rotationally symmetric dispersion of fibers around the main fiber direction using a π-periodic *von Mises* distribution. The *von Mises* distribution is a function of the angle Θ and has, since it is a one-dimensional PDF, the concentration parameter b as the only argument. Its normalized version reads as

$$\rho(\Theta; b) = \frac{1}{2\pi I_0(b)} \exp(b \cos 2\Theta), \tag{3.5}$$

where $I_n(b)$ is the modified Bessel function of the first kind of order n defined as

$$I_n(x) = \frac{1}{\pi} \int_0^\pi \exp[x \cos(\alpha)] \cos(n\alpha) \, \mathrm{d}\alpha. \tag{3.6}$$

In Fig. 3.1, this PDF is plotted for different values of the concentration parameter b, showing that the distribution becomes narrower (higher concentration of fibers in the main fiber direction) for larger values of b.

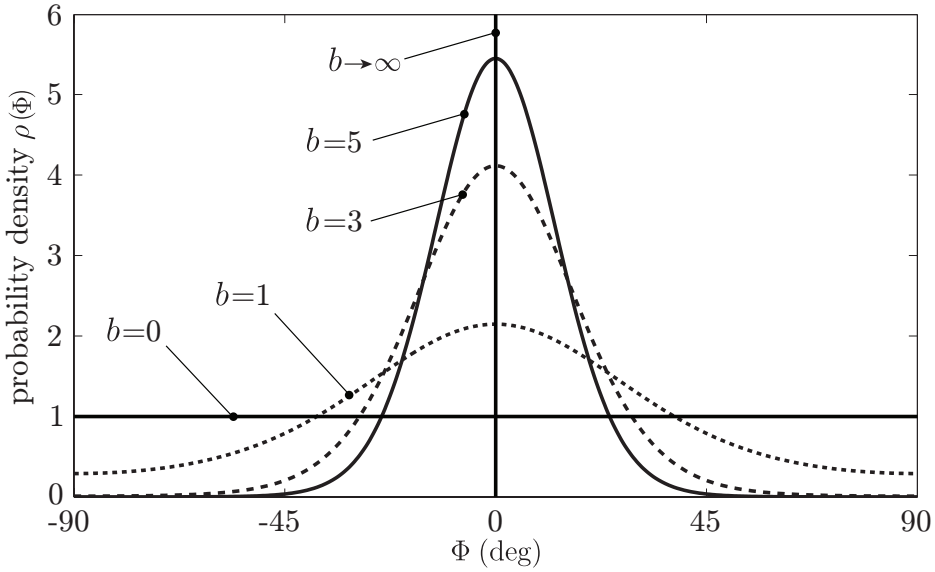

Figure 3.1: The standard *von Mises* distribution for five different concentration parameters $b \in \{0, 1, 3, 5, \infty\}$ and the location parameter $\mu = 0^\circ$ for all five distributions. For $b = 0$ we obtain the uniform distribution (isotropic fiber dispersion) while $b \to \infty$ yields a Dirac delta function at μ (perfect fiber alignment).

Since the material behavior does not depend on the sense of $\mathbf{M}$, the strain-energy only depends on $\mathbf{M}$ through the tensor product $\mathbf{M} \otimes \mathbf{M}$ (see section 2.7) or through a symmetric, second order tensor given by

$$\mathbf{H} = \frac{1}{4\pi} \int_{\mathbb{S}} \rho(\mathbf{M}) \, \mathbf{M} \otimes \mathbf{M} \, \mathrm{d}S, \tag{3.7}$$

which involves only the sines and cosines of Θ and the PDF $\rho(\mathbf{M})$. We denote the components of the structure tensor as $\mathbf{H} = H_{ij} \, \mathbf{e}_i \otimes \mathbf{e}_j$ and notice that due to the symmetries of $\rho(\mathbf{M})$ all off-diagonal components ($H_{ij}, i \neq j$) vanish. By introducing the parameter κ, which is an integral

measure of dispersion, the structure tensor can be written as

$$\mathbf{H} = \kappa\mathbf{I} + (1 - 3\kappa)\mathbf{M} \otimes \mathbf{M} \quad \text{with} \quad \kappa = \frac{1}{4}\int_0^\pi \rho(\Theta)\sin^3\Theta \,\mathrm{d}\Theta. \tag{3.8}$$

Finally, the structure tensor $\mathbf{H}$ is used to compute an average strain quantity

$$\bar{E} = \mathbf{H} : (\overline{\mathbf{C}} - \mathbf{I}) = \mathbf{H} : \overline{\mathbf{C}} - 1, \tag{3.9}$$

because $\mathbf{H} : \mathbf{I} = \mathrm{tr}\,\mathbf{H} = 1$. The authors use this strain quantity in the strain-energy function and follow the approach of [Holzapfel et al., 2000] by using an exponential function to account for the fiber recruitment according to

$$\bar{\Psi}_{\mathrm{f}i}(\overline{\mathbf{C}}, \mathbf{H}_i) = \frac{k_1}{2k_2}\Big\{\exp(k_2\bar{E}_i^2) - 1\Big\}, \quad i = 4, 6, \tag{3.10}$$

where the index i represents the fiber family.

3.4 Other Frameworks Including Dispersion

Mathematically, incorporating a PDF into the constitutive model is not challenging, but the resulting computational costs might be very high. For example, [Einstein, 2002] pointed out that 18 intervals of the PDF are required to capture the full range behavior of the mitral valve for a 2D case. This is mechanically equivalent to 18 weighted fiber families in the plane; in a 3D setting, this requires two integrals to be evaluated for the stress and four for the tangent matrix. In the framework of finite elements, these computations have to be performed for every iteration, for every time step, at every Gauss point for every finite element of the segmented geometry [Freed et al., 2005]. Moreover, if the inhomogeneous material properties of a tissue should be considered, the PDF can vary with the location and differ for each finite element. Therefore it is not only crucial to have a computationally efficient model but also to develop a robust method to determine the dispersion from histology and incorporate it in the computational framework in an efficient way.

In [Holzapfel et al., 2005a], the authors introduce a phenomenological scalar parameter $\rho \in [0, 1]$ which shifts the fiber dispersion from transversely isotropic to isotropic. Since it is introduced in a phenomenological way, it cannot be determined by histology but only by fitting to mechanical data.

The approach of [Sacks, 2003] incorporates a two-dimensional angular fiber distribution into the strain-energy function, considering only in-plane dispersion of fibers. The authors directly use the a mean angular fiber distribution which was determined from scattered light experiments. Therefore, the distribution function appears in the integral for the stress requiring numerical integration. To study perturbations of the distribution function, the beta distribution was used to represent the fiber dispersion. Note that the authors use a Gamma distribution to account for the gradual recruitment of fibers which are assumed to behave linearly elastic. Due to the recruitment distribution (which should not be confused with the fiber dispersion distribution), the final stress-strain relation is nonlinear.

[Driessen et al., 2005] studied the biaxial behavior of the arterial wall and the aortic valve, where the artery is modeled as a thick walled cylinder (following [Holzapfel et al., 2000]), while the aortic valve leaflet is simulated in the closed configuration using finite element analysis. They use a neo-Hookean material law for the isotropic matrix and an effective stress-strain relationship for the collagen fibers. A unimodular discrete normal probability density function accounts for the fiber dispersion, limiting their model to a planar fiber distribution.

[Freed and Doehring, 2005] introduced an alternative pair of directional invariants (similar to [Gasser et al., 2006]), based on[2] I_4 and I_5, denoted $I_{\langle 4\rangle}$ and $I_{\langle 5\rangle}$ where the angle brackets represent the dispersion invariant. To compute this dispersion invariant, they use a tensor $\mathbf{K}$ which reduces to $\mathbf{M} \otimes \mathbf{M}$ in the absence of splay, leading to $I_{\langle 4\rangle} = I_4$ and $I_{\langle 5\rangle} = I_5$. Using the set $\{I_1, I_2, I_3, I_{\langle 4\rangle}, I_{\langle 5\rangle}\}$ as integrity basis, the authors develop a constitutive equation for the Kirchhoff stress tensor. To account for the anisotropy, the authors use the Gaussian distribution to compute the splay invariants via an integral over the unit half-circle (in the 2D case) or the unit half-hemisphere (in the 3D case), including the deformation tensor $\mathbf{C}$ for $I_{\langle 4\rangle}$ and $\mathbf{C}^2$ for $I_{\langle 5\rangle}$, respectively. The integrals defining the stiffness tensor related to anisotropy can be solved analytically, making their approach suitable for an efficient finite element implementation. Nevertheless, the analytical solution requires the complex error function to be evaluated for the stiffness tensor and the fiber dispersion is restricted to the transverse isotropic case.

The model of [Caner et al., 2007] accounts for the fiber-matrix shear interaction by a separate term in the strain-energy function and uses an (inverse) exponential distribution function

[2] We changed their notation to be consistent with our notation.

to model the collagen fiber distribution, where the authors call this function 'anisotropy function'. Since this anisotropy function depends only on one angle, also this model is limited to two-dimensional (in-plane) fiber distributions (or, if generalized to 3D, transversely isotropic distributions).

In [Kroon and Holzapfel, 2008], the authors apply the model of [Holzapfel et al., 2000] to model discrete tissue layers, where the fiber orientations vary with each layer and are uniformly distributed over the azimuthal angle. The fiber stiffness in each layer changes according to a discrete, triangular stiffness distribution. This approach is only capable of modeling planar distributions and it models a distribution of stiffnesses rather than fiber orientations. Hence, the distribution parameters cannot be obtained from histological analysis and the authors fitted eight stiffness parameters $\{k_1, ...k_8\}$ to experimental data from mechanical tests. This corresponds to eight layers, each reinforced with one collagen fiber family with a stiffness k_i. Note that only one of the two material parameters from the model of [Holzapfel et al., 2000] is varied while the other parameter (k_2) is kept constant.

In [Ateshian et al., 2009], the material parameters $\alpha_i(\mathbf{n})$ and $\zeta_i(\mathbf{n})$, $i = 1, 2, 3$, in the strain-energy function are functions of the direction vector $\mathbf{n}$. The authors chose an ellipsoidal distribution for this directional dependence, yielding six parameters for the fiber dispersion, and apply a power-law SEF depending on the square of the fiber stretch to model the mechanical behavior of cartilage. Their model accounts for the osmotic pressure and uses the discretization of the unit sphere as a geodesic dome to solve the integrals for the Cauchy stress and the spatial elasticity tensor. Due to the lack of experimental data, the authors did not fit the fiber distribution to histological data but chose the dispersion parameters so the model fits data reported in literature. Although their model proposes six material parameters for orthotropy, they only use a transverse isotropic distribution for ζ, i.e., $\zeta_2 = \zeta_3$, and an isotropic distribution for α, i.e., $\alpha_1 = \alpha_2 = \alpha_3$.

In [Raghupathy and Barocas, 2009], a closed form solution of a specialized constitutive model based on the work of [Billiar and Sacks, 2000, Driessen et al., 2007] is derived. Although this provides an enormous speedup compared to the integration of the stress over the fiber distribution, it has two major disadvantages: first, it does not account for the different behavior of fibers in tension and compression and second, it is restricted to 2D fiber dispersions.

Also [Federico and Gasser, 2010] adopted the model of [Gasser et al., 2006] to include the extremal case of an in-plane arrangement of fibers and follow the angular integration approach. Their model uses a quadratic polynomial to account for the contribution of collagen fibers to the SEF. This allows the authors to use a spherical t-design to perform a rather complex integration over a unit sphere and implement the model in a finite element framework which they use to simulate cartilage in an unconfined compression and a contact problem in the hip joint. For the simulations, the dispersion was varied linearly from a planar isotropic dispersion in the superficial zone to a completely three-dimensional isotropic dispersion in the middle zone and nearly aligned, transverse isotropic distribution in the deep zone. The material parameters were chosen to qualitatively fit experimental data, which were not quantitatively compared with the model output in this work.

In [Holzapfel and Ogden, 2010b] the authors discuss the model of [Gasser et al., 2006] for the range of $\kappa \in [0, 1/2]$, with $\kappa = 1/2$ as the extreme case of a two-dimensional isotropic distribution, where they show that the range between $1/3$ and $1/2$ yields undesirable effects. Moreover, the work shows the adaptation of the fiber dispersion model of [Gasser et al., 2006] to a planar fiber distribution. We will see very similar results in the work we present here, as the adopted model is a special case of the model presented in section 5.

All mentioned models based on the work of [Gasser et al., 2006] assume a rotationally symmetric distribution of collagen fibers around a preferred fiber direction, an assumption which as been shown to be inappropriate for the arterial wall. For this reason, [Alastrué et al., 2010] suggest a truly three-dimensional PDF to account for the non-rotationally symmetric distribution. Specifically, the Bingham distribution is applied to represent the collagen fiber dispersion, but due to the lack of histological information the authors did not obtain the parameters of this PDF from histology but from data fitting to uniaxial tensile tests. The researchers compare two different material models, namely the exponential model of [Holzapfel et al., 2000] and the eight-chain model [Arruda and Boyce, 1993] for a transversely isotropic material [Kuhl et al., 2005, Alastrué et al., 2009a]. In order to obtain a high accuracy, the numerical integration requires a high order of discretization to perform the integration. The authors state that non-linear transformations might reduce the number of necessary integrations as proposed in [Alastrué et al., 2009b].

In the work of [Agianniotis et al., 2011], the fiber recruitment of collagen is modeled using a log/logistic probability function, whereas the fiber dispersion is represented by a two-dimensional *von Mises* distribution. This allows for a planar fiber distribution neglecting the three-dimensional dispersion of collagen fibers. The value of the concentration parameter of the PDF is fitted to mechanical experimental data and not obtained from histological data. Elastin is modeled as a transverse isotropic material, yielding an isotropic and an anisotropic material parameter for the mechanical behavior of elastin.

In the work of [Gasser et al., 2012], the PDF of [Alastrué et al., 2010] is adopted and incorporated into two different models, a phenomenological one with an exponential SEF and a model with a triangular PDF for the recruitment of collagen fibers leading to a piecewise stress-strain relation. They apply their model to a AAA wall and obtain integral relations for the stress in the circumferential and the axial direction. To solve for the Lagrangian multiplier, they use the membrane approximation, i.e., they neglect the stress in radial direction (transmural stresses) which are believed to be important from a clinical point of view.

In [Pandolfi and Vasta, 2012], the model of [Gasser et al., 2006] is extended by incorporating a higher-order statistical measure $\hat{\kappa} \in [0, 1/15]$ to reduce the differences between the GST and AI formulation. To obtain this measure $\hat{\kappa}$, the approximation of the average anisotropic strain-energy function contains also the quadratic term of the Taylor expansion around the mean value of the fourth invariant $\bar{I}_4$. This requires a fourth-order tensor $\mathbb{H} = \langle \mathbf{H} \otimes \mathbf{H} \rangle$ where $\mathbf{H}$ is[3] the original structure tensor from [Gasser et al., 2006], see eq. (3.7), and the angle brackets denote the averaging over the unit sphere. By utilizing the *von Mises* distribution, the authors find that the incorporation of $\hat{\kappa}$ reduces the difference to the AI formulation compared to the GST approach for uniaxial, biaxial and shear deformation.

Note that some authors include a PDF to represent the engagement of collagen fibers and some utilize two PDFs, one for the collagen fiber recruitment and another to capture the fiber dispersion. An overview of the discussed models is given in table 3.1.

[3] We changed the variable names to be consistent with our notation.

3.5 Shortcomings of Existing Models

As we have seen in this chapter, most models do not use information from histological data to obtain structural parameters describing the fiber dispersion. This is also owed to the fact that the quantification of fiber orientation and dispersion from histological data is challenging and requires a well defined experimental protocol. Since [Schriefl et al., 2013a] showed that diseased arterial walls show also a significant out-of-plane dispersion, two-dimensional fiber dispersion models might not be appropriate. Therefore, it is the aim of this work to develop a straightforward and computationally efficient constitutive model which is based on experimental data and capable of describing the nonlinear behavior of arterial wall tissue. Some existing models are very sophisticated but computationally expensive, which is especially in the context of finite elements and high mesh densities a problem and impedes a potential future application in a clinical setting where high performance computers are not available.

Table 3.1: Overview of existing fiber dispersion models. The column 'Formulation' describes the approach originally presented in the cited paper, 'Parameters' refers only to parameters describing the fiber dispersion and does not list mechanical or any other parameters and the abbreviations 'RS', 'OT', 'IP' and 'DD' mean rotationally symmetric, orthotropic, in plane and discrete distribution, respectively.

Reference	Formulation	PDF	Parameters	2D/3D	Dispersion
[Holzapfel et al., 2005a]	-	-	ρ	3D	RS
[Gasser et al., 2006]	GST	*von Mises*	κ	3D	RS
[Pandolfi and Vasta, 2012]	GST/AI	*von Mises*	$\kappa, \hat{\kappa}$	3D	RS
[Federico and Gasser, 2010]	AI	*von Mises*	b	2D/3D	RS
[Alastrué et al., 2010]	AI	Bingham	κ_2, κ_3	3D	OT
[Gasser et al., 2012]	AI	Bingham	κ_1, κ_2	3D	OT
[Freed and Doehring, 2005]	AI	Gaussian	σ	2D/3D	RS
[Sacks, 2003]	AI	discrete/Beta	γ, δ	2D	IP
[Driessen et al., 2005]	AI	Gaussian	σ	2D	IP
[Ateshian et al., 2009]	AI	ellipsoidal	$\xi_1, \xi_2, \xi_3,$ $\alpha_1, \alpha_2, \alpha_3$	3D	OT
[Agianniotis et al., 2011]	AI	*von Mises*	b	2D	IP
[Kroon and Holzapfel, 2008]	discrete	triangular	E_1, E_2	2D/3D	DD, IP
[Caner et al., 2007]	AI	exponential	c_1, c_2	2D	PD
this thesis	GST	bivariate *von Mises*	$\kappa_{\mathrm{ip}}, \kappa_{\mathrm{op}}$	2D/3D	OT

4 Fitting of Experimental Data

'If you want to understand function, study structure.'

FRANCIS H. C. CRICK

This quote of F. Crick, a co-discoverer of the structure of the DNA molecule, is one of the premises of biomechanics which states that function follows structure and mechanics[1]. As we saw in section 1.3, collagen fibers are the main load bearing constituents at high strains and, therefore, their structural arrangement is of crucial importance. Until the work of [Schriefl et al., 2012a], in which the orientation and dispersion of collagen fibers in the human aorta was quantified, no comparable data were available. Hence, also the models describing the mechanical behavior of the arterial wall were not based on experimentally founded dispersion data of collagen fibers.

In this chapter we first introduce the basics of probability theory and define a coordinate system to describe the fiber dispersion. After that, we will discuss the results of [Schriefl et al., 2012a] and motivate the use of the bivariate *von Mises* distribution to represent the dispersed collagen fibers. To fit this probability density function (PDF) to experimental data we introduce maximum likelihood estimation, well-suited method to determine parameters of distributions. At the end of this chapter, we show results of fitting the PDF to dispersion data obtained by various experimental methods, see chapter 3.

[1] Mechanobiology states that structure follows function, what is not a contradiction to biomechanics but just a different approach.

4.1 Probability Density Functions

The concept of the probability density function (PDF) allows us to describe the probability of finding a fiber in a certain direction in 3D space. First, we will start with a very general definition and then later in this chapter define a specific form of this PDF and show how to ensure that a given PDF fulfills the necessary requirements.

The probability of a random variable X to be in the interval $[a, b] \in \mathcal{X}$ with $\mathcal{X}$ being the sample space of X is given by the PDF $\rho(x)$ defined as

$$P[a \leq X \leq b] = \int_a^b \rho(x)\,\mathrm{d}x, \tag{4.1}$$

and has to fulfill

$$\rho(x) \geq 0 \,\forall\, x \in \mathcal{X}, \quad \int_{\mathcal{X}} \rho(x)\,\mathrm{d}x = 1, \tag{4.2}$$

where eqs. $(4.2)_1$ and $(4.2)_2$ are two requirements of every PDF, i.e., it has to be non-negative and its integral over the whole domain has to be equal to one (normalization condition), respectively. After defining the PDF, we can introduce the cumulative distribution function of X, given by $C_X(x) = \int_{-\infty}^{x} \rho(\alpha)\,\mathrm{d}\alpha$, which describes the probability that X will take a value less or equal to x, i.e., $C_X(x) = P[X \leq x]$. With this function, we can compute the probability of X being in the interval $(a, b]$ by $P[a < X \leq b] = C_X(b) - C_X(a)$. Because of the non-negativity of the PDF given in eq. $(4.1)_2$, the CDF is (not necessarily strictly) monotonically increasing and reaches the limiting values $\lim_{x\to-\infty} C_X(x) = 0$ and $\lim_{x\to\infty} C_X(x) = 1$ [Montgomery and Runger, 2010].

Remark. Note that the boundaries in the latter two equations, i.e., $-\infty$ and ∞, are actually the boundaries of the sample space $\mathcal{X}$ and not necessarily infinite. Especially for periodic PDFs, the boundaries could be, e.g., $-\pi$ and π. We adopted the notation from the most common textbooks and leave it to the reader to adjust these definitions to the specific problem. ■

We can parameterize a PDF by defining a parameter vector $\mathbf{p} = \{p_1, p_2, \ldots, p_n\}$ containing unspecified parameters p_i which, e.g., determine the shape and location of the PDF, and write the resulting PDF as $\rho(x \,|\, \mathbf{p})$ [Lyons, 1989, Evans et al., 2000] .

4.2 Coordinate System

We have to set up a suitable coordinate system to mathematically represent the structural data we obtain from histology. Motivated by the experiments of [Schriefl et al., 2012a], we introduce the coordinate system shown in Fig. 4.1 where the unit vector $\mathbf{M}$ is expressed through the two Eulerian angles Φ and Θ by $\mathbf{M}(\Phi,\Theta) = \cos\Theta\cos\Phi\,\mathbf{e}_1 + \cos\Theta\sin\Phi\,\mathbf{e}_2 + \sin\Theta\,\mathbf{e}_3$. Without loss of generality, we align the preferred fiber direction with the 1-direction and define a normal direction which we align with the 3-direction of the coordinate system.

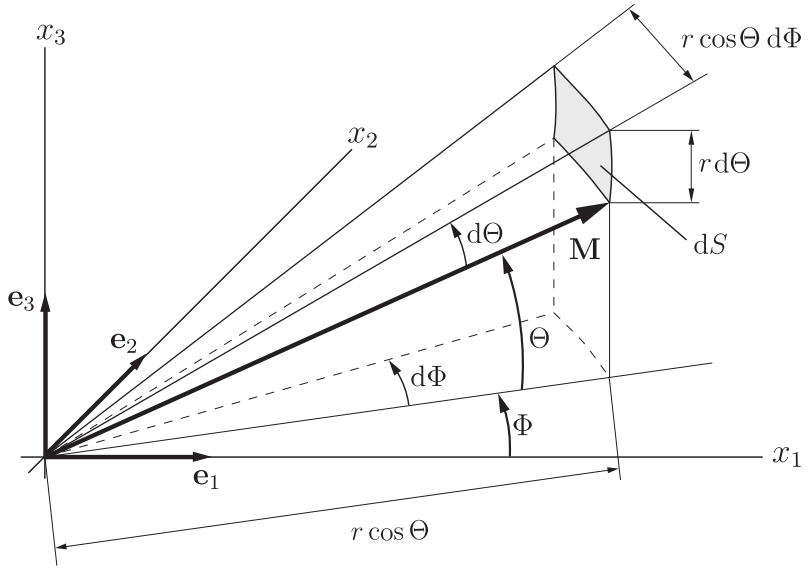

Figure 4.1: Unit vector $\mathbf{M}(\Phi,\Theta)$ defined by the Eulerian angles Φ and Θ in the 3D space. Since $\|\mathbf{M}\| = 1$, the differential surface of the unit sphere described by $\mathbf{M}$ is $\mathrm{d}S = \cos\mathrm{d}\Phi\mathrm{d}\Theta$. We align the 1-direction with the preferred fiber direction and the 3-direction (for symmetric out-of-plane dispersion) with the radial direction, therefore we refer to the angles Φ and Θ as the in-plane and out-of-plane angles, respectively.

Although the coordinate system looks similar to the one presented in [Gasser et al., 2006], there is a subtle but important difference: our approach does not involve an angle rotating around the preferred direction (like the angle Φ in [Gasser et al., 2006]) since there is no experimental evidence for a rotationally symmetric fiber dispersion in the arterial wall.

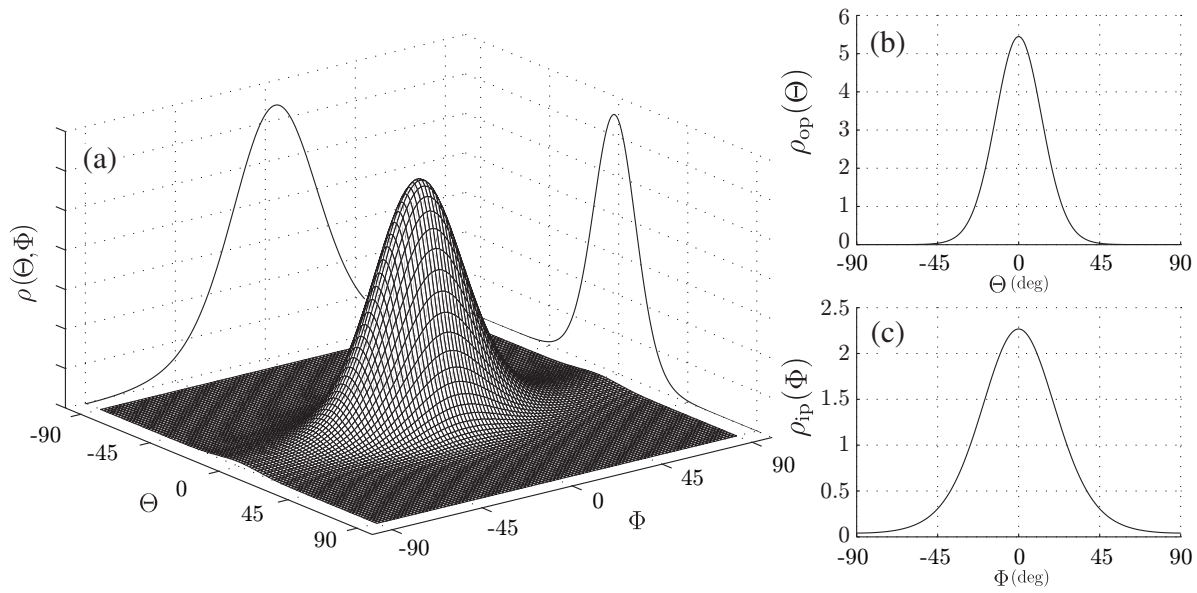

Figure 4.2: In (a), the three-dimensional representation of the bivariate *von Mises* distribution in the Φ,Θ-plane with two concentration parameters, $b_{\mathrm{ip}} = 2$ and $b_{\mathrm{op}} = 5$, is shown. Panels (b) and (c) display the two separate functions $\rho_{\mathrm{ip}}(b_{\mathrm{ip}},\Phi)$ and $\rho_{\mathrm{op}}(b_{\mathrm{op}},\Theta)$ which are multiplied to yield an orthotropic 3D fiber dispersion function.

4.3 The Bivariate von Mises Distribution

The coordinate system defined in the previous section allows us to introduce a probability density function $\rho(\mathbf{M}(\Phi,\Theta))$ describing the fiber dispersion in the reference configuration as a function of the unit vector $\mathbf{M}(\Phi,\Theta)$ in 3d space. The PDF has to be normalized, c.f. eq. $(4.2)_2$, so the integration over the unit sphere S yields

$$\frac{1}{4\pi}\int_S \rho(\Phi,\Theta)\,\mathrm{d}S = 1, \tag{4.3}$$

where $\mathrm{d}S = \cos\Theta\,\mathrm{d}\Theta\,\mathrm{d}\Phi$ and the factor $1/(4\pi)$ normalizes the surface of the unit sphere to one. After this very general introduction, we can specify the PDF based on histological observations in [Schriefl et al., 2012a,d] which yielded angular data of the in-plane collagen dispersion of the intima, media and adventitia of the thoracic aorta, the abdominal aorta and the common iliac arteries. In [Schriefl et al., 2012a], the out-of-plane angle has not been measured separately for every layer because the distributions out-of-plane are very similar at all anatomic locations and layers. Moreover, the authors observed no correlation between the dispersion in-plane and

out-of-plane, meaning that the fiber dispersions in these planes are independent of each other. Note that in-plane corresponds to the $1,2$-plane in Fig. 4.2 and out-of-plane is the dispersion in the 3-direction.

A PDF representing a fiber distribution has to fulfill the symmetry of a fiber, $\rho(\mathbf{M}) \equiv \rho(-\mathbf{M})$, which is equivalent to $\rho(\Phi, \Theta) = \rho(\Phi + \pi, -\Theta)$. Based on the experimental results presented in [Schriefl et al., 2012a,d], we identify two additional symmetries[2] of our density function, namely the symmetry in-plane $\rho(\Phi, \Theta) = \rho(-\Phi, \Theta)$ and the symmetry out-of-plane $\rho(\Phi, \Theta) = \rho(\Phi, -\Theta)$. Moreover, the independence of the dispersion in-plane and out-of-plane allows us to split the density function in a multiplicative way, i.e, $\rho(\Phi, \Theta) = \rho_{\mathrm{ip}}(\Phi)\rho_{\mathrm{op}}(\Theta)$. With this split, the symmetry requirements read as $\rho_{\mathrm{ip}}(\Phi) = \rho_{\mathrm{ip}}(-\Phi)$ and $\rho_{\mathrm{op}}(\Theta) = \rho_{\mathrm{op}}(-\Theta)$.

Based on these observations we choose to represent the fiber dispersion with a π-periodic bivariate *von Mises* distribution [Mardia, 1975], a PDF which takes the azimuthal angle Φ and the elevation angle Θ as arguments and features the symmetries discussed in the previous paragraph. The bivariate *von Mises* distribution is a multiplication of two π-periodic *von Mises* distributions given by

$$\rho(\Phi, \Theta) = N_{\mathrm{c}} \exp(b_{\mathrm{ip}} \cos 2\Phi) \exp(b_{\mathrm{op}} \cos 2\Theta) = N_{\mathrm{c}} \bar{\rho}_{\mathrm{ip}}(b_{\mathrm{ip}}, \Phi) \bar{\rho}_{\mathrm{op}}(b_{\mathrm{op}}, \Theta), \tag{4.4}$$

where N_{c} is a normalization constant depending on b_{ip} and b_{op}. A plot of this 3D distribution is shown in Fig. 4.2.

The original π-periodic *von Mises* distribution $\tilde{\rho}(\alpha)$ [Mardia and Jupp, 1999] was already introduced in eq. (3.5), and is given by

$$\tilde{\rho}(\alpha) = \frac{\exp[b \cos(2(\alpha - \mu))]}{2\pi I_0(b)}, \tag{4.5}$$

where $b > 0$ is the concentration parameter and μ is the location parameter defining the shape and the location of the distribution, respectively. The distribution is normalized by $I_0(b)$, where $I_n(b)$ is the modified Bessel function of the first kind of order n defined as (c.f. eq. (3.6))

$$I_n(x) = \frac{1}{\pi} \int_0^{\pi} \exp[x \cos(\alpha)] \cos(n\alpha) \, \mathrm{d}\alpha. \tag{4.6}$$

[2] Here, symmetry means a fiber dispersion symmetric around the main fiber orientation in the respective plane.

A plot of this circular distribution for different concentration parameters is shown in Fig. 3.1, where the location parameter is set to $\mu = 0^\circ$ for all distributions. This form of the *von Mises* distribution is π-periodic, a close approximation to the wrapped normal distribution, simple and yet sufficient to describe experimental data very well as we will see in this chapter. We use maximum likelihood estimation to obtain the parameters b_{ip} and b_{op} of the PDFs $\rho_{\mathrm{ip}}(\Phi)$ and $\rho_{\mathrm{op}}(\Theta)$, respectively, therefore we will introduce this method in the following.

4.4 Maximum Likelihood Estimation

In this section, we will give a short introduction on maximum likelihood estimation (MLE)[3] which will be used to obtain the parameters of the PDF $\rho(\boldsymbol{\theta}|\mathbf{p})$ since it has many optimal parameters in estimation: (i) sufficiency: the MLE estimator contains the complete information about the parameter of interest; (ii) consistency: the true value for the parameter that generated the data is recovered asymptotically; (iii) efficiency: the lowest possible variance of parameter estimates is achieved asymptotically; (iv) parameterization invariance: the same MLE solution is obtained independently of the parameterization used. For proofs of these properties see [Miura, 2011].

Remark. Very often least squares estimation (LSE) is used to determine parameters of distributions. It should be noted that LSE is not a method for parameter estimation but an approach that is primarily used with linear regression models. Although it is possible to determine parameters of a PDF by minimizing the sum of squared errors (what is done in LSE), this method has several disadvantages as we pointed out in [Schriefl et al., 2012c], hence we prefer the parameter identification via MLE. Nevertheless, in chapter 6 we use LSE to fit parameters of the constitutive model to mechanical data, an application where LSE is widely accepted. ■

From experiments, we obtain a data vector $\boldsymbol{\theta} = \{\theta_1, \theta_2, \ldots, \theta_n\}$ containing the measured fiber angles. We define the number of angles in a certain interval from θ_i to θ_{i+1} as $y_i = \{\mathrm{count}\,(\theta)\,\forall\,\theta_i \leq \theta < \theta_{i+1}\}$. The collection of these numbers of angles in a certain, most of the times constant, interval, gives the 'histogram' vector $\mathbf{y}$. The boundaries θ_i define the bin size of

[3] MLE was invented by R. Fisher, the father-in-law of G. E. P. Box who we get to know at the beginning of the next chapter.

the histogram, if, for example, the bin size is chosen to be 5° and the range of admissible angles is $\theta \in [-90, 90)$, we get $y_1 = \{\text{count}(\theta) \forall\ -90 \leq \theta \leq -85\}$ or $y_4 = \{\text{count}(\theta) \forall\ -75 \leq \theta < -70\}$.

Note that when we use second harmonic generation (SHG) or multiphoton microscopy (MPM) to determine the fiber orientation and dispersion, we directly obtain an intensity spectrum which can be interpreted as a histogram vector.

The vector $\boldsymbol{\theta}$ can be seen as a random sample (i.e., a set of observations) from an unknown population. This population is described by a probability density distribution $\rho(\boldsymbol{\theta}|\mathbf{p})$, and $\boldsymbol{\theta}$ is a realization of ρ for a specific choice of the parameter vector $\mathbf{p}$ and n samples. If individual observations θ_i are statistically independent of one another, the PDF for the data $\boldsymbol{\theta} = \{\theta_1, \theta_2, \ldots, \theta_n\}$ can, given the parameter vector $\mathbf{p}$, be expressed as a multiplication of PDFs for individual observations,

$$\rho(\boldsymbol{\theta} = \{\theta_1, \theta_2, \ldots, \theta_n\} \,|\, \mathbf{p}) = \rho(\theta_1 \,|\, \mathbf{p})\, \rho(\theta_2 \,|\, \mathbf{p}) \ldots \rho(\theta_n \,|\, \mathbf{p}) = \prod_{i=1}^{n} \rho(\theta_i \,|\, \mathbf{p}). \tag{4.7}$$

According to the PDF some set of data is, for given parameters, more probable than another set. If we look at the *von Mises* distribution we see that for, e.g., a large concentration parameter b, a 'peaked' distribution is more likely than an isotropic one. Since we already observed the data, we are confronted with an inverse problem: we have the data and know the function which generated them (at least we assume to know the underlying PDF), and now we have to find the parameters of the PDF which are most likely to have generated the data. To solve this inverse problem, we define the likelihood function by reversing the roles of the data vector $\boldsymbol{\theta}$ and the parameter vector $\mathbf{p}$, i.e.

$$\mathcal{L}(\mathbf{p} \,|\, \boldsymbol{\theta}) = \rho(\boldsymbol{\theta} \,|\, \mathbf{p}). \tag{4.8}$$

Here, $\mathcal{L}(\mathbf{p} \,|\, \boldsymbol{\theta})$ represents the likelihood of the parameter $\mathbf{p}$ given the data observed in $\boldsymbol{\theta}$ and is therefore a function of $\mathbf{p}$. Since the functions are defined on different scales, they are not directly comparable with each other. More specifically, the PDF is defined on the data scale since it is a function of the data given a particular set of parameters. The likelihood function, in contrast, is a function of the parameters given a particular set of data and is thus defined on the parameter scale. We can interpret the likelihood function as the likelihood of a particular parameter value

for a fixed data set, where the likelihood has the interpretation of an 'unnormalized probability'. For a model with one parameter, the plot of the likelihood function is a curve, whereas for e.g., two parameters the resulting visualization is a surface in the parameter space. Once we have a set of data, we can find the most suited set of parameters for our given distribution. The method of maximum likelihood estimation seeks to find the set of parameters which maximize the likelihood function. Hence MLE seeks to find the parameters of the PDF making the observed data most likely.

Since the logarithm of a function and the function itself have the same maximum, the computation of the MLE estimate uses the logarithm of the likelihood function, i.e., $\ln \mathcal{L}(\mathbf{p} \,|\, \boldsymbol{\theta})$, rather than $\mathcal{L}(\mathbf{p} \,|\, \boldsymbol{\theta})$. We want to maximize the function, therefore we look for the roots of the first derivative of the likelihood function, and since the shape of the likelihood must be convex in order to be a maximum and not a minimum, we require the second derivative to be negative for all parameter estimates p_i, i.e.,

$$\frac{\partial \ln \mathcal{L}(\mathbf{p} \,|\, \boldsymbol{\theta})}{\partial p_i} = 0, \quad \frac{\partial^2 \ln \mathcal{L}(\mathbf{p} \,|\, \boldsymbol{\theta})}{\partial p_i^2} < 0. \tag{4.9}$$

In general it is not possible to obtain the analytical solution of the MLE estimate, the MLE estimate must therefore be found numerically using nonlinear optimization algorithms, e.g., with the `mle` command in MATLAB.

4.5 Fitting of Arterial Collagen Dispersion Data

Fitting of Two Fiber Families. In [Schriefl et al., 2012c], we showed an automated method to determine the orientation and dispersion of collagen fibers from 2D images. Therein we used the *von Mises* distribution and MLE to obtain the principal direction and dispersion values of collagen fibers in a human intima.

Since the arterial wall is often reinforced with two dispersed fiber families, we might find an overlapping region in the histogram of fiber angles, see, for example, Fig. 4.3. In this case we use a mixture (additive superposition) of two *von Mises* distributions, given by

$$\rho_{\text{mix}}(\Phi) = \rho_1(\Phi) + \rho_2(\Phi) = \sum_{i=1}^{2} \frac{\exp[b_i \cos(2(\Phi - \mu_i))]}{I_0(b_i)}, \tag{4.10}$$

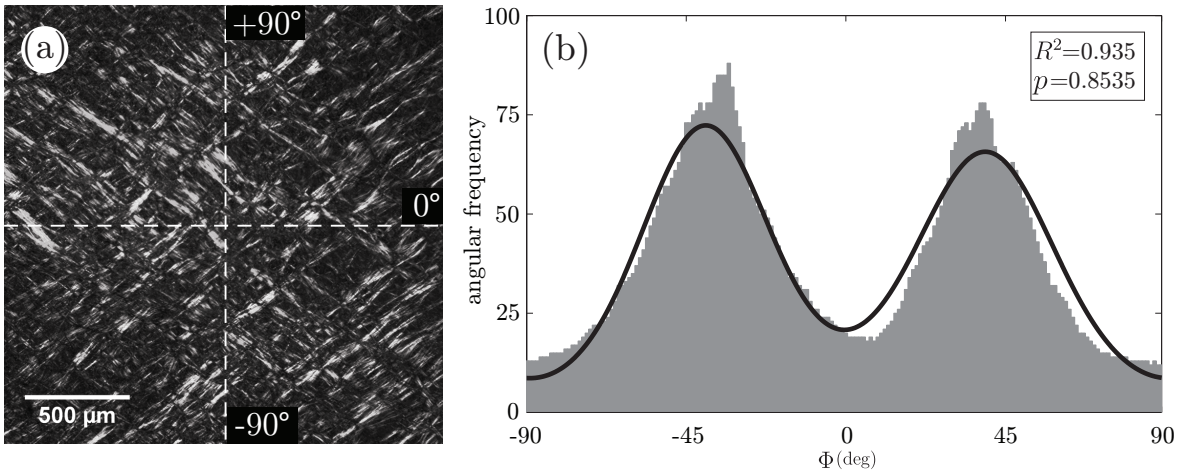

Figure 4.3: Panel (a) shows an in-plane section of the intima of a thoracic aorta which was obtained by polarized light microscopy and picrosirius red staining. The white dashed lines labeled 0° and 90° represent the circumferential and axial direction of the vessel. In panel (b), the angular fiber distribution of the image in panel (a) is shown. We used maximum likelihood estimation of two superimposed *von Mises* distributions to determine the fitting parameters, i.e., $b_1 = 2.503$, $\mu_1 = 39.6^\circ$, $b_2 = 2.149$, $\mu_2 = 39.4^\circ$, clearly indicating two symmetric fiber families [Schriefl et al., 2012b].

to fit the dispersion data and account for the superposition of two fiber families. Hence, the concentration parameters b_1 and b_2 and the location parameters μ_1 and μ_2 of the two distributions are fitted. It is not required to normalize the mixture of the two *von Mises* distributions in (4.10) since it is only used in the fitting process to determine the four fitting parameters and the data is not normalized [Lyons, 1989]. If there is only one fiber family present as, e.g., for the out-of-plane dispersion, only one *von Mises* distribution and two distribution parameters have to be determined.

The result of the fitting procedure is shown in Fig. 4.3 where we see two peaks and a substantial amount of fiber dispersion. Moreover, the goodness of fit measures (R^2 and p-value) indicate that two superimposed *von Mises* distributions are suitable to represent the fiber dispersion. Note that Fourier power spectrum analysis yields an intensity plot and cannot directly be used for the parameter estimation using MLE. Instead, we use the histogram to infer the underlying angles which 'generated' this intensity distribution required for the MLE procedure. For details regarding the data analysis and parameter estimation see [Schriefl et al., 2012c].

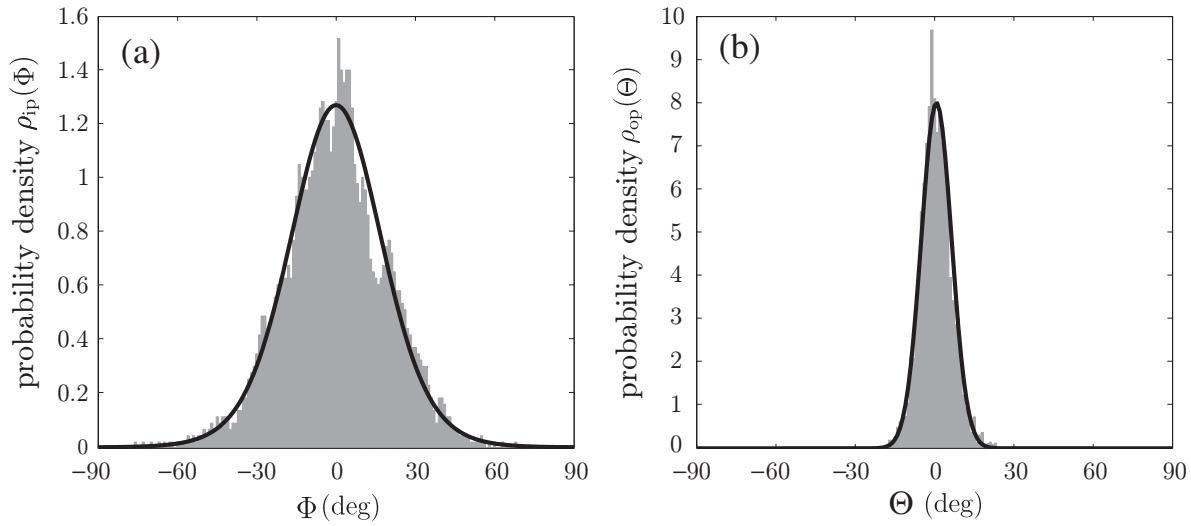

Figure 4.4: Collagen fiber dispersion taken from [Schriefl et al., 2012a] and fitted with a *von Mises* distribution, from which the location and concentration parameters were determined. Panel (a) shows the in-plane dispersion of the media of the common iliac arteries, where one fiber family is visible. In panel (b), we show the out-of-plane dispersion, where the angular distribution was obtained from the whole arterial wall. The obtained parameters are $b_{\mathrm{ip}} = 2.84$ and $b_{\mathrm{op}} = 25.3$, with R^2 values of 0.974 and 0.970, respectively. Note that for both distributions the location parameter $\mu \sim 0^\circ$, i.e., the distribution is aligned circumferentially in-plane and axially out-of-plane.

In Fig. 4.4(a), the result of fitting one fiber family is shown. Again, the high R^2-value indicates that the *von Mises* distribution is very suitable to fit dispersed collagen fibers.

Fitting out-of-plane Data. While in [Schriefl et al., 2012b] we show the applicability of the *von Mises* distribution to represent the in-plane dispersion, also the out-of-plane dispersion has to be considered. Therefore, we fitted the data of [Schriefl et al., 2012a] where also the out-of-plane dispersion of the human aorta was assessed, see Fig. 4.4(b). Again, the good fit suggests that the *von Mises* distribution is a good choice to represent the dispersion of collagen fibers in human arteries. The work of [Schriefl et al., 2013a] also shows that the *von Mises* distribution is also applicable for diseased arteries which show a much higher out-of-plane dispersion than healthy arteries.

Fitting of Dispersion Data Throughout the Arterial Wall. While [Schriefl et al., 2012a] were the first who quantified the collagen fiber dispersion in the human aortic wall, the method to obtain the dispersion data is quite laborious since fiber angles had to be measured manually. To overcome this problem, the same group presented an automated method to quantify the three dimensional structure of collagen fibers using optical clearing and second-harmonic generation imaging [Schriefl et al., 2012d].

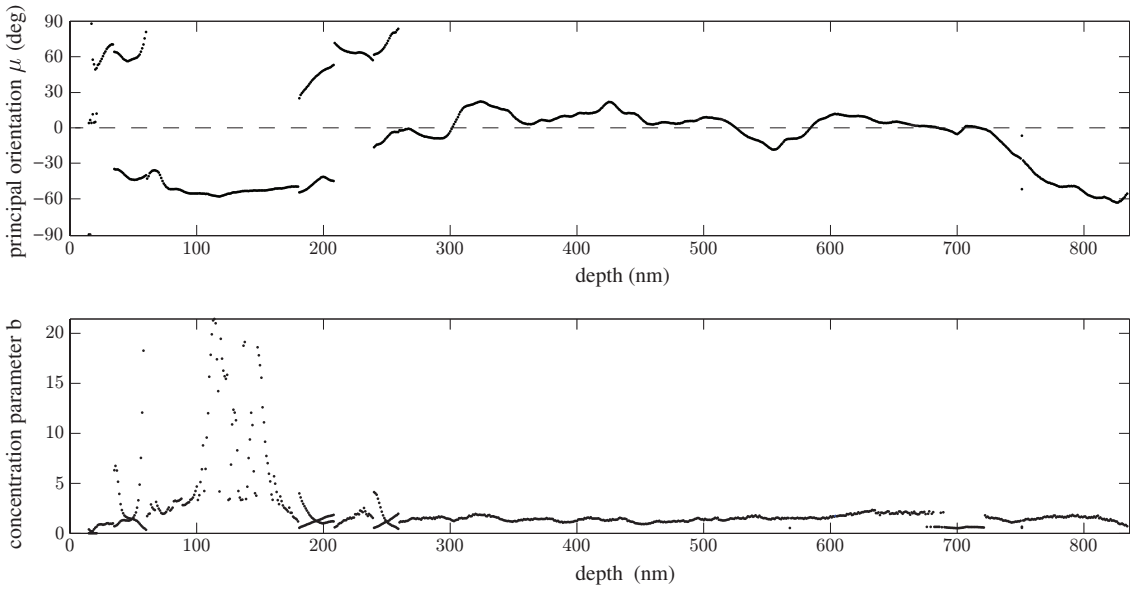

Figure 4.5: Result of the fitting procedure from data record $\#1$ in Table 4.1. The top panel shows the fitting results of the angle μ through the depth of the specimen, where at first two different fiber families are visible. Around 230 nm, only one fiber family which is oriented circumferentially can be seen. In the lower plot, the dispersion parameter b is plotted [Schriefl et al., 2012d]. In the region from 100 to 200 nm (corresponding to the adventitia), two highly aligned fiber families around $\pm 45^\circ$ are visible. After that, the media is reinforced with two fiber families which are oriented much closer to the circumferential direction and feature much higher dispersion.

This approach yields three-dimensional image stacks, so called z-stacks, where each image shows the in-plane distribution of collagen fibers. The researchers obtained the continuous three-dimensional fiber distribution with a resolution of one degree to determine both the fiber orientation and dispersion throughout the entire arterial wall using the methods we presented in [Schriefl et al., 2012c]. We use their data to compute an average b-value, i.e,, an average mea-

sure of fiber dispersion of the whole arterial wall. In Fig. 4.5, one exemplary result of this fitting procedure throughout the arterial wall is shown. We identified an inhomogeneous distribution of fiber orientation and dispersion depending on the depth and related to the structure of the wall. For example, in the adventitia (approximately the first 230 nm) the fibers are more aligned and oriented more towards the axial direction compared to other regions.

It also should be noted that the histology varies strongly between each specimen, as it is the case for every biological tissue. We nevertheless computed average values for the principal fiber orientation and fiber dispersion and, therefore, homogenize the tissue. For the fiber angle we take the mean value of all orientations in the wall, but for the dispersion the median is a more appropriate measure since in a small region the values differ considerably from the others.

Table 4.1: Results of 9 measurements of human aortas as described in [Schriefl et al., 2012d] and described in the text. The data were obtained by maximum likelihood estimation and yielded a list of principal orientations μ and b_{ip}-values for each data set, from which we calculate the mean and median. One exemplary dataset ($\#1$) is shown in Fig. 4.5 where the fiber orientation and dispersion through the thickness of the arterial wall are depicted.

	Data record	$\pm\mu$ in$^\circ$	mean of b_{ip}	median of b_{ip}
	1	27	2.23	1.49
	2	28	2.4	1.54
	3	16	2.07	1.88
	4	14	1.69	1.64
	5	22	1.5	1.3
	6	23	1.56	1.39
	7	19	1.2	1.26
	8	28	1.58	1.36
	9	32	1.96	1.3
Mean		23.2	1.8	1.46
Variance		36.7	0.151	0.041
Standard Deviation		6.05	0.389	0.202

In the end, we take the mean of these measures as the input variables for the constitutive model. Note that b_{ip} is a measure for the in-plane dispersion and is used in chapter 5 to compute an integral measure of dispersion for the constitutive model. In chapter 6, we use these histological parameters in the fitting procedure to determine the mechanical parameters of the model. Since the interspecimen variability is that high and we do not have the histological information of the specimens used for fitting the mechanical data in chapter 6, we do not restrict the histological parameters completely. Instead, we allow them to vary within the boundaries of twice the standard deviation[4], since the mean value $\pm$ two times the standard deviation contains, assuming a normal distribution, approximately $95\,\%$ of the data.

[4]The standard deviation is the square root of the variance, see Table 4.1.

5 Novel Constitutive Framework Considering Fiber Dispersion

'Essentially, all models are wrong, but some are useful.'

GEORGE E. P. BOX

As we have seen in chapter 3, there are quite a few constitutive models in the literature which account for the fiber dispersion in soft biological tissue. We have also seen that a few of them are capable to represent the 'real' distribution of collagen fibers in arterial tissue, and most of them are computationally very expensive.

In this chapter we present a novel structural continuum mechanical framework which incorporates fiber dispersion and is at the same time computationally efficient. First, we introduce a structure tensor to describe an orthotropic fiber dispersion without specifying a particular choice for the PDF. Then, we use the bivariate *von Mises* distribution to represent the three-dimensional fiber dispersion and show some special cases of fiber dispersion. Finally, we propose a SEF which is the basis to derive the stress and elasticity tensors required for a finite element implementation of the constitutive law. We will see that our proposed model is indeed useful in chapter 6 .

5.1 Structure Tensor for an Orthotropic Fiber Dispersion

We use a structure tensor to mathematically quantify the fiber dispersion, which in the end will be incorporated in a strain-energy function (see section 2.5), describing the material behavior. As shown in section 3.3, we can define a structure tensor according to

$$\mathbf{H} = \frac{1}{4\pi} \int_{\mathbb{S}} \rho(\mathbf{M})\, \mathbf{M} \otimes \mathbf{M}\, \mathrm{d}S, \tag{5.1}$$

which accounts for the fiber orientation through $\mathbf{M}$ and fiber dispersion through $\rho(\mathbf{M})$. Since the dispersion function is orthotropic, all off-diagonal components vanish.

As shown in section 4.3, we decompose the PDF $\rho(\Phi, \Theta)$ into two density functions, $\rho_{\mathrm{ip}}(\Phi)$ and $\rho_{\mathrm{op}}(\Theta)$, describing the in-plane and out-of-plane dispersion, respectively. Hence the probability of finding a fiber oriented with $\mathbf{M}(\Phi, \Theta)$ is given by $\rho(\Phi, \Theta) = \rho_{\mathrm{ip}}(\Phi)\rho_{\mathrm{op}}(\Theta)$. Because the symmetry of the PDF still has to be fulfilled, we require $\rho_{\mathrm{ip}}(\Phi) = \rho_{\mathrm{ip}}(-\Phi)$ and $\rho_{\mathrm{op}}(\Theta) = \rho_{\mathrm{op}}(-\Theta)$.

With this multiplicative split of the PDF we can easily verify that the off-diagonal components of $\mathbf{H}$ vanish by examining at the properties of the two PDFs and the integration boundaries in eq. (5.1). Upon rewriting the latter equation, we obtain

$$\mathbf{H} = \frac{1}{4\pi} \int_{\Phi=-\pi}^{\pi} \int_{\Theta=-\pi/2}^{\pi/2} \rho_{\mathrm{ip}}(\Phi)\rho_{\mathrm{op}}(\Theta)\, \mathbf{M} \otimes \mathbf{M} \cos\Theta\, \mathrm{d}\Theta\, \mathrm{d}\Phi. \tag{5.2}$$

When we take a look at the off-diagonal components of $\mathbf{M} \otimes \mathbf{M}$ we find (i) $\cos^3\Theta \cos\Phi \sin\Phi$, (ii) $\cos^2\Theta \cos\Phi \sin\Theta$ and (iii) $\cos^2\Theta \sin\Phi \sin\Theta$. Remembering that both $\rho_{\mathrm{ip}}(\Phi)$ and $\rho_{\mathrm{op}}(\Theta)$ are symmetric functions, we can conclude the following: in (i) the trigonometrical functions in Φ are symmetric and asymmetric, hence the product is asymmetric and the integration from $-\pi$ to π with $\rho_{\mathrm{ip}}(\Phi)$, a symmetric function, yields zero. In (ii) and (iii) the functions of Θ are asymmetric, hence the integration of the product with $\rho_{\mathrm{op}}(\Theta)$, a symmetric function, vanishes.

With these properties, the structure tensor $\mathbf{H}$ represents an orthotropic fiber dispersion with the components

$$H_{11} = \kappa_{\mathrm{op}}(C - 3\kappa_{\mathrm{ip}}), \quad H_{22} = 3\kappa_{\mathrm{ip}}\kappa_{\mathrm{op}}, \quad H_{33} = 1 - C\kappa_{\mathrm{op}}. \tag{5.3}$$

In eq. (5.3) we introduced three abbreviations for the integrals constituting the main diagonal of **H**, namely two dispersion measures κ_{ip} and κ_{op} describing the dispersion in-plane and out-of-plane, given as

$$\kappa_{\mathrm{ip}} = \frac{1}{3\pi} \int_{\Phi=-\pi}^{\pi} \rho_{\mathrm{ip}}(\Phi) \sin^2 \Phi \, \mathrm{d}\Phi, \quad \kappa_{\mathrm{op}} = \frac{1}{4} \int_{\Theta=-\pi/2}^{\pi/2} \rho_{\mathrm{op}}(\Theta) \cos^3 \Theta \, \mathrm{d}\Theta, \tag{5.4}$$

and a constant

$$C = \frac{1}{\pi} \int_{\Phi=-\pi}^{\pi} \rho_{\mathrm{ip}}(\Phi) \, \mathrm{d}\Phi. \tag{5.5}$$

In the next section we will construct the structure tensor **H** in a convenient notation with a particular choice of the density function $\rho(\Phi, \Theta)$.

5.2 Incorporating the Bivariate *von Mises* Distribution

In section 4.3 we demonstrated that the bivariate *von Mises* distribution is very suitable to represent the fiber dispersion in the arterial wall. The PDF has to fulfill the normalization condition, given in eq. (4.3), which can be rewritten as

$$\int_{\mathbb{S}} \rho(\Phi, \Theta) \, \mathrm{d}S = N_{\mathrm{c}}(b_{\mathrm{ip}}, b_{\mathrm{op}}) \int_{\Theta=-\pi/2}^{\pi/2} \bar{\rho}_{\mathrm{ip}}(\Theta) \cos \Theta \, \mathrm{d}\Theta \int_{\Phi=-\pi}^{\pi} \bar{\rho}_{\mathrm{op}}(\Phi) \, \mathrm{d}\Phi = 4\pi. \tag{5.6}$$

where the bar indicates that the PDF is not normalized yet, c.f. eq. (4.4). From eq. (5.6) we can determine the normalization constant

$$N_{\mathrm{c}}(b_{\mathrm{ip}}, b_{\mathrm{op}}) = \sqrt{\frac{b_{\mathrm{op}}}{2\pi}} \frac{4}{I_0(b_{\mathrm{ip}}) \mathrm{erf}(\sqrt{2b_{\mathrm{op}}}) \exp(b_{\mathrm{op}})}, \tag{5.7}$$

where $\mathrm{erf}(\bullet)$ is the error function defined as

$$\mathrm{erf}(x) = \frac{2}{\sqrt{\pi}} \int_0^x \exp(-\xi) \, \mathrm{d}\xi. \tag{5.8}$$

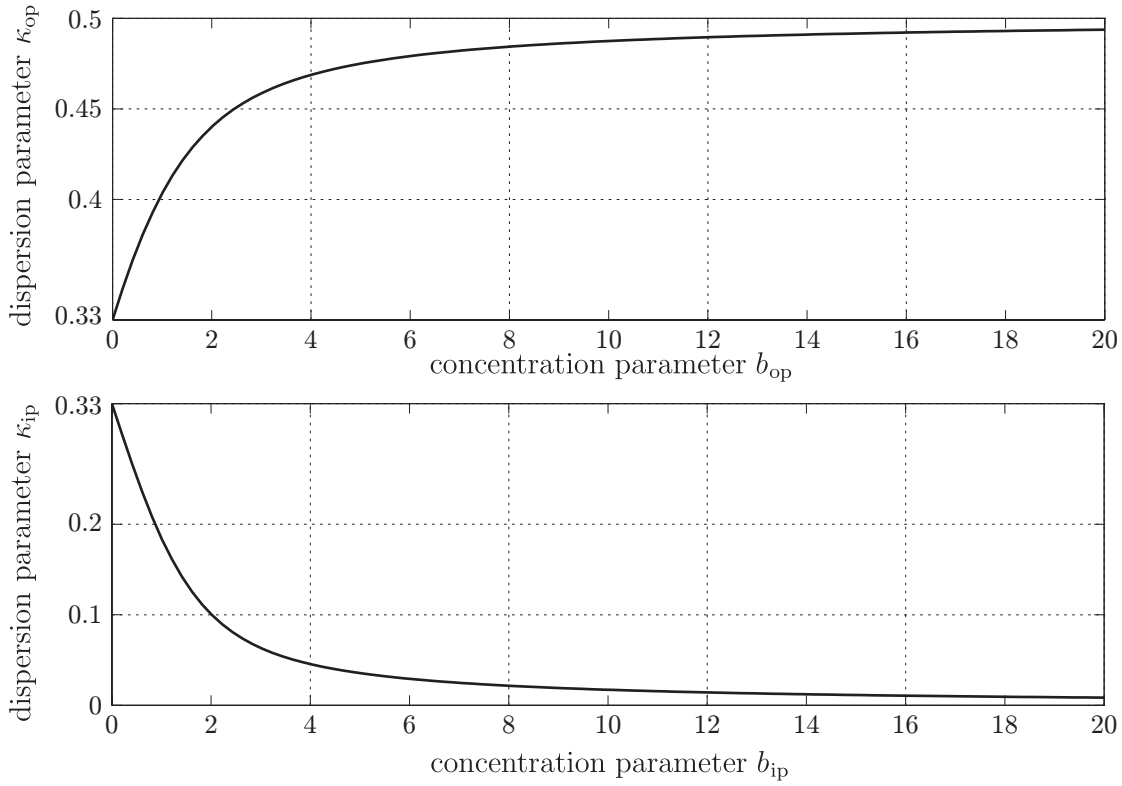

Figure 5.1: In this figure, the highly nonlinear relations between the concentration parameters $b_{\mathrm{op}}, b_{\mathrm{ip}}$ and the corresponding dispersion measures $\kappa_{\mathrm{op}} \in [1/3, 1/2]$ and $\kappa_{\mathrm{ip}} \in [0, 1/3]$ are shown. For isotropy, both concentration parameters are zero and the dispersion parameters are $\kappa_{\mathrm{op}} = \kappa_{\mathrm{ip}} = 1/3$. In the case of perfect alignment, on the other hand, the concentration parameters go towards infinity and the dispersion measures are $\kappa_{\mathrm{op}} = 1/2, \kappa_{\mathrm{ip}} = 0$.

It is arbitrary how we distribute the constant N_{c} on the two PDFs $\rho_{\mathrm{ip}}(\Phi)$ and $\rho_{\mathrm{op}}(\Theta)$ since the PDFs have to fulfill the normalization condition together, i.e., their multiplication has to fulfill eq. (4.3); therefore, we define the probability density functions as

$$\rho_{\mathrm{ip}}(\Phi) = \frac{1}{I_0(b_{\mathrm{ip}})} \exp[a(\cos 2\Phi)], \quad \rho_{\mathrm{op}}(\Theta) = 4\sqrt{\frac{b_{\mathrm{op}}}{2\pi}} \frac{\exp[b_{\mathrm{op}}(\cos 2\Theta - 1)]}{\mathrm{erf}(\sqrt{2b_{\mathrm{op}}})}, \tag{5.9}$$

for the in-plane and out-of-plane dispersion, respectively.

Although it is theoretically arbitrary how we distribute the normalization constant on the two PDFs, it is convenient to separate the concentration parameters b_{ip} and b_{op} so they are with the respective PDF, i.e., $\rho_{\mathrm{ip}}(\Phi)$ and $\rho_{\mathrm{op}}(\Theta)$. This enables us to fit the in-plane and out-of-plane dispersion separately.

Using the PDFs given in eq. (5.9), the constant C in eq. (5.5) is 2 and the dispersion parameters are given by

$$\kappa_{\mathrm{op}} = \frac{1}{4} \int_{\Theta=-\pi/2}^{\pi/2} 4\sqrt{\frac{b_{\mathrm{op}}}{2\pi}} \frac{\exp[b_{\mathrm{op}}(\cos 2\Theta - 1)]}{\mathrm{erf}(\sqrt{2b_{\mathrm{op}}})} \cos^3\Theta \mathrm{d}\Theta, \tag{5.10}$$

$$\kappa_{\mathrm{ip}} = \frac{1}{3\pi} \int_{\Phi=-\pi}^{\pi} \frac{1}{I_0(b_{\mathrm{ip}})} \exp[b_{\mathrm{ip}}(\cos 2\Phi)] \sin^2\Phi \mathrm{d}\Phi. \tag{5.11}$$

A closed form solution for the integrals in eqs. (5.10),(5.11) is given by

$$\kappa_{\mathrm{op}} = \frac{1}{3}\left(1 - \frac{I_1(b_{\mathrm{ip}})}{I_0(b_{\mathrm{ip}})}\right), \qquad \kappa_{\mathrm{op}} = \frac{1}{4}\left(2 - \frac{1}{2b_{\mathrm{op}}} + \frac{\exp(-2b_{\mathrm{op}})\sqrt{2/\pi}}{\sqrt{b_{\mathrm{op}}}\,\mathrm{erf}(\sqrt{2b_{\mathrm{op}}})}\right). \tag{5.12}$$

These relations allow for the computation of the concentration parameters for given dispersion values κ_{ip} and κ_{op} using a nonlinear solver like `FindRoot` in MATHEMATICA or `fsolve` in MATLAB. In Fig. 5.1, the (nonlinear) relations between the concentration parameters and the dispersion parameters are shown. We see that for the isotropic case both dispersion parameters are $1/3$ while for perfect fiber alignment $\kappa_{\mathrm{ip}} = 0$ and $\kappa_{\mathrm{op}} = 1/2$. With the parameters κ_{ip} and κ_{op} we can construct the structure tensor

$$\mathbf{H} = 3\kappa_{\mathrm{ip}}\kappa_{\mathrm{op}}\mathbf{I} + [2\kappa_{\mathrm{op}}(1 - 3\kappa_{\mathrm{ip}})]\mathbf{M}_{\mathrm{f}} \otimes \mathbf{M}_{\mathrm{f}} + [1 - \kappa_{\mathrm{op}}(2 + 3\kappa_{\mathrm{ip}})]\mathbf{M}_{\mathrm{n}} \otimes \mathbf{M}_{\mathrm{n}}, \tag{5.13}$$

where $\mathbf{I}$ is the second-order identity tensor and $\mathbf{M}_{\mathrm{f}}$ and $\mathbf{M}_{\mathrm{n}}$ are unit vectors oriented in the main fiber direction and the direction perpendicular on the main plane of dispersion, respectively. Note that these vectors coincide with the 1- and 3-direction of the coordinate system introduced in Fig. 4.1. These vectors should not be confused with $\mathbf{M}(\Phi, \Theta)$ since $\mathbf{M}$ is an arbitrarily oriented unit vector in space while $\mathbf{M}_{\mathrm{f}}$ and $\mathbf{M}_{\mathrm{n}}$ are unit vectors oriented in a certain direction.

5.3 Special Cases of Fiber Dispersions

Our model includes several other existing dispersion models as special cases. In this section, we will discuss some cases of fiber dispersions which are summarized in Table 5.1 and shown in Fig. 5.2, where $\rho(\mathbf{M})\mathbf{M}$ is visualized.

Table 5.1: Special cases of the proposed model. The abbreviations used are PA: perfect alignment, PI: planar isotropy, ID: isotropic distribution, PD: planar distribution and RS: rotationally symmetric distribution. The references are [1] [Holzapfel et al., 2000], [2] [Holzapfel and Ogden, 2010b], [3] [Federico and Gasser, 2010], [4] [Holzapfel et al., 2005a], [5] [Gasser et al., 2006].

Case	Conc. parameters	Dispersion parameters	Structure tensor	Ref.
PA	$b_{\mathrm{ip}} \to \infty, b_{\mathrm{op}} \to \infty$	$\kappa_{\mathrm{ip}} \to 0, \kappa_{\mathrm{op}} \to 1/2$	$\mathbf{H} = \mathbf{M}_{\mathrm{f}} \otimes \mathbf{M}_{\mathrm{f}}$	[1]
PD	$b_{\mathrm{op}} \to \infty$	$\kappa_{\mathrm{op}} \to 1/2$	$\mathbf{H} = 3/2\kappa_{\mathrm{ip}}[\mathbf{I} - \mathbf{M}_{\mathrm{n}} \otimes \mathbf{M}_{\mathrm{n}}] + (1 - 3\kappa_{\mathrm{ip}})\mathbf{M}_{\mathrm{f}} \otimes \mathbf{M}_{\mathrm{f}}$	[2,3]
PI	$b_{\mathrm{ip}} \to 0, b_{\mathrm{op}} \to \infty$	$\kappa_{\mathrm{ip}} \to 1/3, \kappa_{\mathrm{op}} \to 1/2$	$\mathbf{H} = 1/2(\mathbf{I} - \mathbf{M}_{\mathrm{n}} \otimes \mathbf{M}_{\mathrm{n}})$	[2,3]
ID	$b_{\mathrm{ip}} = 0, b_{\mathrm{op}} = 0$	$\kappa_{\mathrm{ip}} = 1/3, \kappa_{\mathrm{op}} = 1/3$	$\mathbf{H} = 1/3\mathbf{I}$	[4,5]
RS	-	$\kappa_{\mathrm{op}} = 1/(3\kappa_{\mathrm{ip}} + 2)$	$\mathbf{H} = 3\kappa_{\mathrm{ip}}\kappa_{\mathrm{op}}\mathbf{I} + [2\kappa_{\mathrm{op}}(1 - 3\kappa_{\mathrm{ip}})]\mathbf{M}_{\mathrm{f}} \otimes \mathbf{M}_{\mathrm{f}}$	[3,5]

Isotropic Distribution. An isotropic fiber distribution is represented by a uniform distribution in both planes, meaning that $\rho(\Phi, \Theta) = 4\pi$ and is independent of Φ and Θ. This distribution is characterized by $(b_{\mathrm{ip}} = 0, b_{\mathrm{op}} = 0) \to (\kappa_{\mathrm{ip}} = 1/3, \kappa_{\mathrm{op}} = 1/3)$ and the structure tensor reads as $\mathbf{H} = 1/3\mathbf{I}$, featuring no preferred direction.

Planar Isotropic Distribution. If a distribution features perfectly out-of-plane alignment ($b_{\mathrm{op}} \to \infty$) and is fully dispersed in-plane ($b_{\mathrm{ip}} = 0$), it is planar isotropic (2D isotropy). The according dispersion parameters are $\kappa_{\mathrm{op}} = 1/2$ and $\kappa_{\mathrm{ip}} = 1/3$. For this case, the structure tensor is given by $\mathbf{H} = 1/2(\mathbf{I} - \mathbf{M}_{\mathrm{n}} \otimes \mathbf{M}_{\mathrm{n}})$.

Planar Distribution. A distribution with all the fibers oriented in-plane, as presented in [Holzapfel and Ogden, 2010b], has perfect alignment in this plane, resulting in a zero out-of-plane dispersion. Hence we get $(b_{\mathrm{op}} \to \infty) \to (\kappa_{\mathrm{op}} \to 1/2)$ and the according structure tensor is $\mathbf{H} = 3/2\kappa_{\mathrm{ip}}[\mathbf{I} - \mathbf{M}_{\mathrm{n}} \otimes \mathbf{M}_{\mathrm{n}}] + (1 - 3\kappa_{\mathrm{ip}})\mathbf{M}_{\mathrm{f}} \otimes \mathbf{M}_{\mathrm{f}}$.

Note that the PDF describing the in-plane dispersion $\rho_{\mathrm{ip}}(\Phi)$ in eq. $(5.9)_1$ is the same as in [Holzapfel and Ogden, 2010b]. Nevertheless, the formulation for the structure tensor presented in this thesis looks different since the in-plane dispersion measure $\kappa_{\mathrm{ip}} \in [0, 1/3]$ whereas [Holzapfel and Ogden, 2010b] introduce a dispersion parameter $\kappa_{2\mathrm{d}} \in [0, 1/2]$. Also note that any planar distribution represented by our model can be used in a 3D setting and is not restricted to 2D problems.

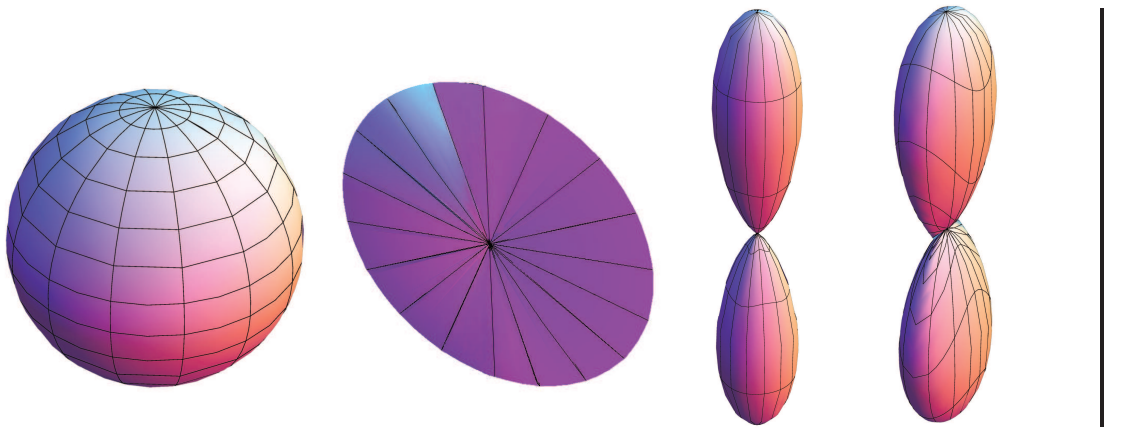

Figure 5.2: Visualization of the fiber distribution defined by $\rho(\mathbf{M})\,\mathbf{M}$ where the distance from the center to the surface represents the probability of finding a fiber in the according direction. The plots have been scaled differently and represent an (a) 3D isotropic fiber distribution; (b) 2D (planar) isotropic fiber distribution; (c) a rotationally symmetric distribution; (d) a non-rotationally symmetric distribution and (e) a perfectly aligned distribution. The associated parameters and structure tensors are given in Table 5.1.

Rotationally Symmetric Distribution. A rotationally symmetric distribution features only one preferred direction, meaning that two components of the structure tensor are equal (transverse isotropy). This is achieved by $\kappa_{\text{op}} = 1/(3\kappa_{\text{ip}} + 2)$ and yields $\mathbf{H} = 3\kappa_{\text{ip}}\kappa_{\text{op}}\mathbf{I} + [2\kappa_{\text{op}}(1 - 3\kappa_{\text{ip}})]\mathbf{M}_{\text{f}} \otimes \mathbf{M}_{\text{f}}$.

Since we do not use a rotationally symmetric coordinate system but base our work on experimental observations [Schriefl et al., 2012a,d], the case of rotational symmetry looks different than in [Gasser et al., 2006]. Nevertheless, the presented model is able to represent a rotationally symmetric fiber distribution as a special case which might be appropriate for tissues such as cartilage or the myocardium.

Perfect Alignment. If both concentration parameters b_{ip} and b_{op} reach infinity, the dispersion in both planes becomes zero and we obtain the model proposed by [Holzapfel et al., 2000]. With $(b_{\text{ip}} \to \infty, b_{\text{op}} \to \infty) \to (\kappa_{\text{ip}} \to 0, \kappa_{\text{op}} \to 1/2)$ and the structure tensor $\mathbf{H} = \mathbf{M}_{\text{f}} \otimes \mathbf{M}_{\text{f}}$, hence all fibers are oriented in the direction of $\mathbf{M}_{\text{f}}$.

Table 5.2: Summary of the parameters of the proposed model. The vectors $\mathbf{M}_{\mathrm{f}}$ and $\mathbf{M}_{\mathrm{n}}$ are defined in the coordinate system shown in Fig. 4.1. The column 'Exp. method' refers to the way how the parameter can be determined, i.e., the structural parameters can be determined by histological methods while the mechanical parameters need to be fitted to mechanical tests, e.g., uniaxial or biaxial tension).

Parameter	Interpretation	Range	Exp. method
c [kPa]	stiffness of isotropic ground matrix	$[0, \infty)$	Mech. tests
k_1 [kPa]	stress-like parameter	$[0, \infty)$	Mech. tests
k_2 [-]	dimensionless parameter	$[0, \infty)$	Mech. tests
κ_{ip} [-]	dispersion in-plane	$[0, 1/3]$	Histology
κ_{op} [-]	dispersion out-of-plane	$[1/3, 1/2]$	Histology
$\mathbf{M}_{\mathrm{f}}$ [-]	preferred fiber direction	hemisphere	Histology
$\mathbf{M}_{\mathrm{n}}$ [-]	normal direction on the dispersion plane	hemisphere	Histology

5.4 Anisotropic Strain-Energy Function

Up to now we have only considered one fiber family with the direction vectors $\mathbf{M}_{\mathrm{f}}$ and $\mathbf{M}_{\mathrm{n}}$ defining the main fiber direction and normal direction, respectively. In order to generalize the model to more than one fiber family we introduce the vectors $\mathbf{M}_{\mathrm{f}i}$ and $\mathbf{M}_{\mathrm{n}i}$, where the index i denotes the ith fiber family. Note that our approach follows the work of [Holzapfel et al., 2000] where the volumetric part of the strain-energy is additively splitted in the isochoric contributions of the ground matrix $\bar{\Psi}_{\mathrm{g}}$ and the fibers $\bar{\Psi}_{\mathrm{f}}$.

In the following we include two fiber families which are oriented symmetrically and feature the same material parameters and equal dispersion in both planes. Hence, the superposition of energies reads as

$$\bar{\Psi} = \bar{\Psi}_{\mathrm{g}} + \sum_{i=4,6} \bar{\Psi}_{\mathrm{f}i}(\overline{\mathbf{C}}, \mathbf{H}_i(\kappa_{\mathrm{ip}}, \kappa_{\mathrm{op}}, \mathbf{M}_{\mathrm{f}i}, \mathbf{M}_{\mathrm{n}i})). \tag{5.14}$$

Following [Holzapfel and Weizsäcker, 1998] we model the groundmatrix with a neo-Hookean material $\Psi_{\mathrm{g}} = c/2(\bar{I}_1 - 3)$, where the stress-like parameter c is the shear modulus in the reference configuration.

For the fiber contribution, we adopt the phenomenological approach of [Gasser et al., 2006] using an exponential function

$$\bar{\Psi}_{\mathrm{f}i}(\overline{\mathbf{C}}, \mathbf{H}_i) = \frac{k_1}{2k_2}[\exp(k_2 \bar{E}_i^2) - 1], \quad i = 4, 6, \tag{5.15}$$

where k_1 is a stress-like parameter and k_2 is a dimensionless parameter describing the mechanical behavior of the collagen fibers, see [Holzapfel et al., 2000] and eq. (3.10). Here, $\bar{E}_i = \mathbf{H}_i : (\overline{\mathbf{C}} - \mathbf{I})$ is a Green-Lagrange strain like quantity which can be interpreted as an averaged or weighted fiber strain, depending on the fiber dispersion through the structure tensor $\mathbf{H}$ and the (isochoric) macroscopic deformation through $\overline{\mathbf{C}}$.

Since $\mathrm{tr}\,(\mathbf{H}_i) = 1$, we can write the average fiber strain $\bar{E}_i = \mathbf{H}_i : \overline{\mathbf{C}} - 1$ and give an interpretation of this quantity by

$$\bar{E} = \int_S \rho(\mathbf{M})\, \overline{\mathbf{C}} : \mathbf{M} \otimes \mathbf{M}\, \mathrm{d}S - 1 = \int_S \rho(\mathbf{M}) \lambda^2\, \mathrm{d}S - 1 = \langle \lambda \rangle^2 - 1, \tag{5.16}$$

where $\langle \lambda \rangle^2$ is a weighted average of λ^2 and hence $\bar{E}$ is a weighted strain [Cortes et al., 2010].

When we perform the double contraction of $\mathbf{H}_i$ with $\overline{\mathbf{C}}$ we get

$$\bar{E}_i = 3\kappa_{\mathrm{ip}}\kappa_{\mathrm{op}}\bar{I}_1 + [2\kappa_{\mathrm{op}}(1 - 3\kappa_{\mathrm{ip}})]\bar{I}_{4\mathrm{f}} + [1 - \kappa_{\mathrm{op}}(2 + 3\kappa_{\mathrm{ip}})]\bar{I}_{4\mathrm{n}} - 1, \tag{5.17}$$

where we introduced the directionally dependent pseudo-invariants of the symmetric tensors $\mathbf{H}$ and $\overline{\mathbf{C}}$ which are defined as

$$\bar{I}_{\mathrm{f}i} = \overline{\mathbf{C}} : \mathbf{M}_{\mathrm{f}i} \otimes \mathbf{M}_{\mathrm{f}i} \quad \text{and} \quad \bar{I}_{\mathrm{n}i} = \overline{\mathbf{C}} : \mathbf{M}_{\mathrm{n}i} \otimes \mathbf{M}_{\mathrm{n}i}, \quad i = 4, 6. \tag{5.18}$$

These invariants are the square of the stretches of the ith fiber family in the fiber direction $\mathbf{M}_{\mathrm{f}i}$ and normal direction $\mathbf{M}_{\mathrm{n}i}$, respectively. An overview of the parameters is given in Table 5.2.

Following [Holzapfel et al., 2000, Holzapfel and Gasser, 2001], we make the common assumption that the fibers do not resist any compression and are only active in tension. The invariant $\bar{I}_{\mathrm{f}i}$ is used as a switch between fiber compression and tension where the anisotropic part only contributes to the strain-energy if $\bar{I}_{\mathrm{f}i} > 1$, which is the same approach as presented in [Gasser et al., 2006].

The strain-energy function used in the proposed model consequently reads as

$$\bar{\Psi} = \begin{cases} \dfrac{c}{2}(\bar{I}_1 - 3) + \displaystyle\sum_{i=4,6} \frac{k_1}{2k_2}\Big\{ \exp\Big[k_2 \bar{E}_i^2\Big] - 1\Big\} & \text{if} \quad \bar{I}_{\text{if}} > 1, \\ \dfrac{c}{2}(\bar{I}_1 - 3) + \displaystyle\sum_{i=4,6} \frac{k_1}{2k_2}\Big\{ \exp\Big[k_2 (3\kappa_{\text{ip}}\kappa_{\text{op}}\bar{I}_1 - 1)^2\Big] - 1\Big\} & \text{if} \quad \bar{I}_{\text{if}} \leq 1. \end{cases} \tag{5.19}$$

As pointed out in [Holzapfel et al., 2004], this is sufficient for the convexity of the potential for perfect fiber alignment, i.e., $\kappa_{\text{ip}} = 0, \kappa_{\text{op}} = 1/2$. The handling of fiber compression is also a numerical issue which is extensively discussed in [Eriksson et al., submitted] where the authors compare different ways to deal with compression for the model presented in [Gasser et al., 2006].

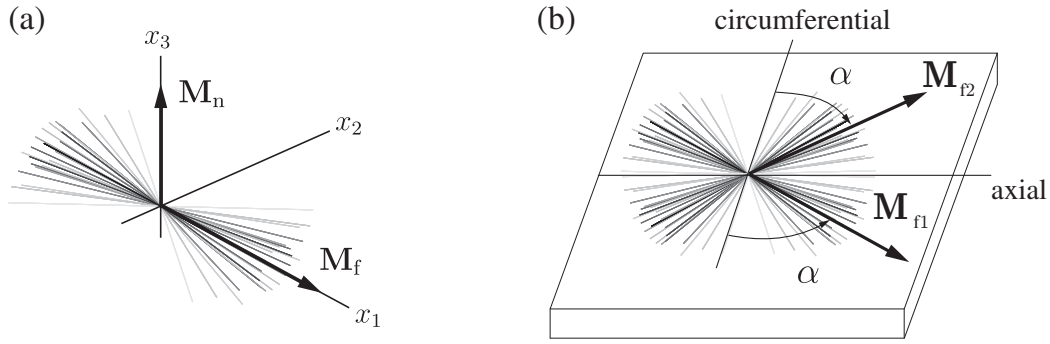

Figure 5.3: Panel (a) illustrates the fiber dispersion of a single fiber family in its 'local' coordinate system which corresponds to the one presented in 4.1. The 1- and 3-direction of this coordinate system coincide with the preferred fiber direction $\mathbf{M}_{\text{f}}$ and normal direction $\mathbf{M}_{\text{n}}$. Panel (b) shows two symmetric fiber families where the main fiber direction is aligned in-plane and makes an angle α with the circumferential direction.

5.5 Derivation of the Elasticity and Stress Tensors

In order to implement the model in a nonlinear finite element code, the tangent modulus, i.e., the elasticity tensor, is required. Since we want to use the software package FEAP, the spatial elasticity tensor and also the Kirchhoff stress tensor need to be computed. Due to the incompressibility of the material we focus on the isochoric contributions of $\overline{\boldsymbol{\tau}}$ and $\overline{\mathbb{C}}$, as defined in eq. $(2.23)_2$ and eq. $(2.42)_2$.

To work with a convenient notation, we introduce the scalar stress function and the scalar elasticity function as

$$\psi'_{\mathrm{f}i} = \frac{\partial \bar{\Psi}_{\mathrm{f}}}{\partial \bar{E}} = k_1 \bar{E}_i \exp(k_2 \bar{E}_i^2) \quad \text{and} \quad \psi''_{\mathrm{f}i} = \frac{\partial^2 \bar{\Psi}_{\mathrm{f}}}{\partial \bar{E}^2} = k_1(1 + 2k_2 \bar{E}_i^2) \exp(k_2 \bar{E}_i^2), \tag{5.20}$$

respectively. These functions are scalar measures of the stress/elastic response and are used in the derivatives of the strain-energy function with respect to the modified right Cauchy-Green tensor, which are given by

$$\frac{\partial \bar{\Psi}_{\mathrm{f}}}{\partial \overline{\mathbf{C}}} = \psi'_{\mathrm{f}i} \mathbf{H}_i, \quad \frac{\partial^2 \bar{\Psi}_{\mathrm{f}}}{\partial \overline{\mathbf{C}}^2} = \psi''_{\mathrm{f}i} \mathbf{H}_i \otimes \mathbf{H}_i, \tag{5.21}$$

where we used $\partial \bar{E} / \partial \overline{\mathbf{C}} = \mathbf{H}$ and $\partial^2 \bar{E} / \partial \overline{\mathbf{C}}^2 = \mathbf{H} \otimes \mathbf{H}$. In order to implement the finite element method in an Eulerian setting, the push-forward of the stress tensor and the elasticity tensor are required. These tensors can be expressed by the respective scalar stress/elasticity function and the Eulerian structure tensor, and we introduce the push-forward of the Lagrangian structure tensor via the unimodular part of the deformation gradient $\overline{\mathbf{h}}_i = \overline{\mathbf{F}} \mathbf{H}_i \overline{\mathbf{F}}^{\mathrm{T}}$.

The Kirchhoff Stress Tensor. As in [Holzapfel, 2000], we split the contribution of the ground matrix and the fibers to the fictitious stress according to

$$\tilde{\boldsymbol{\tau}} = \tilde{\boldsymbol{\tau}}_{\mathrm{g}} + \sum_{i=4,6} \tilde{\boldsymbol{\tau}}_{\mathrm{f}i}, \tag{5.22}$$

where n denotes the number of fiber families. We represent the non-collagenous isotropic ground matrix by a neo-Hookean material, yielding the isochoric response of the Kirchhoff stress according to $\overline{\boldsymbol{\tau}}_{\mathrm{g}} = \operatorname{dev} \tilde{\boldsymbol{\tau}}_{\mathrm{g}} = \mathbb{P} : \tilde{\boldsymbol{\tau}}_{\mathrm{g}}$ with $\tilde{\boldsymbol{\tau}}_{\mathrm{g}} = c\, \overline{\mathbf{b}}$.

To obtain the stress contribution of the ith fiber family, we perform the push-forward of the second Piola-Kirchhoff stress tensor where we can use the scalar stress function defined in eq. $(5.20)_1$ as

$$\tilde{\boldsymbol{\tau}}_{\mathrm{f}i} = 2 \overline{\mathbf{F}} \frac{\partial \bar{\Psi}}{\partial \overline{\mathbf{C}}} \overline{\mathbf{F}}^{\mathrm{T}} = 2 \psi'_{\mathrm{f}i} \overline{\mathbf{h}}_i. \tag{5.23}$$

To finally obtain the Kirchhoff stress tensor, we have to project the fictitious Kirchhoff stress tensor by $\overline{\boldsymbol{\tau}} = \mathbb{P} : \tilde{\boldsymbol{\tau}}$.

The Spatial Elasticity Tensor. Using the equations for the elasticity tensor in the Eulerian setting, given in section 2.6, we derive $\mathbb{c}$ for the specific choice of our strain-energy function $\bar{\Psi}_{\mathrm{f}}(\overline{\mathbf{C}}, \mathbf{H}_i)$. We obtain the first term of eq. $(2.42)_2$ in the contribution of the ith fiber family to the isochoric elasticity tensor as

$$\overline{\mathbb{c}}_1 = \mathbb{P} : \tilde{\mathbb{c}}_{\mathrm{f}i} : \mathbb{P} = 4J^{-4/3}\psi''_{\mathrm{f}i}(\mathbb{P} : \overline{\mathbf{h}}_i) \otimes (\mathbb{P} : \overline{\mathbf{h}}_i), \tag{5.24}$$

where $\tilde{\mathbb{c}}_{\mathrm{f}i} = 4J^{-4/3}\psi''_{\mathrm{f}i}\,\overline{\mathbf{h}}_i \otimes \overline{\mathbf{h}}_i$ (see eq. $(5.21)_2$ and (2.41)). Hence, the complete isochoric elasticity tensor in the spatial configuration is given as

$$\overline{\mathbb{c}} = 4J^{-4/3} \sum_{i=4,6} \psi''_{\mathrm{f}i}(\mathbb{P} : \overline{\mathbf{h}}_i) \otimes (\mathbb{P} : \overline{\mathbf{h}}_i) + \frac{2}{3}\mathrm{tr}\,(\tilde{\boldsymbol{\tau}})\mathbb{P} - \frac{2}{3}(\mathbf{I} \otimes \overline{\boldsymbol{\tau}} + \overline{\boldsymbol{\tau}} \otimes \mathbf{I}). \tag{5.25}$$

Considering the minor and major symmetries of the elasticity tensor, which arise from the symmetry of $\mathbf{E}$ and Schwarz's theorem, we can utilize Voigt notation and implement an efficient finite element code in the finite analysis program FEAP [Taylor, 2000].

6 Simulations

'Computers are useless. They only give you answers.'

PABLO PICASSO

This quote of Picasso is not completely true since computers enable us to obtain answers very fast, so they are certainly not useless. Still, it is more important to state the right questions and set up a reasonable framework to address them (which we hope to have achieved in the previous chapters). Now we have to solve nonlinear problems (e.g., using Newton-Raphson-like algorithms) for complex geometries (where the finite element is an appropriate tool); all methods which heavily rely on computational power.

Up to now we refined an existing constitutive model of the arterial wall considering new experimental results regarding collagen fiber dispersion. After determining the dispersion parameters of the model in section 4.5, we will determine the mechanical parameters of our proposed model in this chapter by fitting it to biaxial tension tests. Therefore, we will first derive the analytical solution of this deformation and then show how to implement a nonlinear fitting procedure. After that, we simulate the inflation of a thin walled tube, but since the artery is thick walled and certainly not a simple tube, finite element analysis is required to perform more realistic and patient-specific simulations. Hence, we conclude this chapter by a simple example where we compare different fiber dispersion cases for the biaxial extension of a unit cube and present the result using finite elements and the corresponding analytical solution. This serves not only to validate the finite element implementation but also to demonstrate the influence of fiber dispersion on the mechanical behavior.

6.1 Biaxial Extension

We consider a sample with two symmetric fiber families, where the fibers make an angle α with the circumferential axis, see Fig. 5.3(b). To obtain the second Piola-Kirchhoff stress tensor **S**, we have to derive the strain-energy function with respect to the right Cauchy-Green tensor **C**, c.f. eq. $(2.16)_2$. Since the Cauchy stress tensor is the push-forward of the second Piola-Kirchhoff stress tensor, it reads as

$$\begin{aligned}\boldsymbol{\sigma} &= 2\mathbf{F}\frac{\partial\bar{\Psi}}{\partial\mathbf{C}}\mathbf{F}^{\mathrm{T}} - p\mathbf{I} = 2\mathbf{F}\left(\sum_{i=1,4\mathrm{f},4\mathrm{n}}\frac{\partial\bar{\Psi}}{\partial I_i}\frac{\partial I_i}{\partial\mathbf{C}}\right)\mathbf{F}^{\mathrm{T}} - p\mathbf{I},\\ &= 2\mathbf{F}\left(\frac{\partial\bar{\Psi}}{\partial I_1}\mathbf{I} + \frac{\partial\bar{\Psi}}{\partial I_{4\mathrm{f}}}\mathbf{M}_{\mathrm{f}}\otimes\mathbf{M}_{\mathrm{f}} + \frac{\partial\bar{\Psi}}{\partial I_{4\mathrm{n}}}\mathbf{M}_{\mathrm{n}}\otimes\mathbf{M}_{\mathrm{n}}\right)\mathbf{F}^{\mathrm{T}} - p\mathbf{I}\\ &= 2\left(\frac{\partial\bar{\Psi}}{\partial I_1}\mathbf{b} + \frac{\partial\bar{\Psi}}{\partial I_{4\mathrm{f}}}\mathbf{m}_{\mathrm{f}}\otimes\mathbf{m}_{\mathrm{f}} + \frac{\partial\bar{\Psi}}{\partial I_{4\mathrm{n}}}\mathbf{m}_{\mathrm{n}}\otimes\mathbf{m}_{\mathrm{n}}\right) - p\mathbf{I},\end{aligned} \tag{6.1}$$

where the Lagrange multiplier p enforces the incompressibility condition. The vectors $\mathbf{m}_{\mathrm{f}}$ and $\mathbf{m}_{\mathrm{n}}$ are the push-forward of $\mathbf{M}_{\mathrm{f}}$ and $\mathbf{M}_{\mathrm{n}}$, see eq. (2.45), and $\mathbf{b} = \mathbf{F}\mathbf{F}^{\mathrm{T}}$ is the left Cauchy-Green tensor. For biaxial tension of an incompressible material the deformation is described by

$$[\mathbf{F}] = \mathrm{diag}\,[\lambda_1, \lambda_2, (\lambda_1\lambda_2)^{-1}], \quad [\mathbf{C}] = [\mathbf{F}]^{\mathrm{T}}[\mathbf{F}] = \mathrm{diag}\,[\lambda_1^2, \lambda_2^2, (\lambda_1\lambda_2)^{-2}]$$

and the unit vectors describing the fiber direction and normal direction in the reference state are given by

$$\mathbf{M}_{\mathrm{f}} = [\sin\alpha \quad \cos\alpha \quad 0]^{\mathrm{T}}, \quad \mathbf{M}_{\mathrm{n}} = [0 \quad 0 \quad 1]^{\mathrm{T}}, \tag{6.2}$$

which are used to compute the invariants

$$\begin{aligned} I_1 &= \lambda_1 + \lambda_2 + \lambda_3 = \lambda_1 + \lambda_2 + (\lambda_1\lambda_2)^{-2}\\ I_{4\mathrm{f}} &= \mathbf{C} : (\mathbf{M}_{\mathrm{f}}\otimes\mathbf{M}_{\mathrm{f}}) = \lambda_1^2\sin^2\alpha + \lambda_2^2\cos^2\alpha,\\ I_{4\mathrm{n}} &= \mathbf{C} : (\mathbf{M}_{\mathrm{n}}\otimes\mathbf{M}_{\mathrm{n}}) = (\lambda_1\lambda_2)^{-2}. \end{aligned} \tag{6.3}$$

Using the average strain (eq. (5.17)), the scalar stress function (eq. $(5.20)_1$), and the chain rule, we obtain the derivatives of the strain-energy function as

$$\frac{\partial\bar{\Psi}}{\partial I_1} = \frac{c}{2} + 6\kappa_{\mathrm{ip}}\kappa_{\mathrm{op}}\psi'_{\mathrm{f}i}, \quad \frac{\partial\bar{\Psi}}{\partial I_{4\mathrm{f}}} = 4\kappa_{\mathrm{op}}(1-3\kappa_{\mathrm{ip}})\psi'_{\mathrm{f}i}, \quad \frac{\partial\bar{\Psi}}{\partial I_{4\mathrm{n}}} = 2[1-\kappa_{\mathrm{op}}(2+3\kappa_{\mathrm{ip}})]\psi'_{\mathrm{f}i},$$

and finally get the Cauchy stress tensor

$$\begin{aligned}\boldsymbol{\sigma} = c\mathbf{b} + 4\psi'_{\mathrm{f}i}\big\{&3\kappa_{\mathrm{ip}}\kappa_{\mathrm{op}}\mathbf{b} + 2\kappa_{\mathrm{op}}(1-3\kappa_{\mathrm{ip}})\mathbf{m}_{\mathrm{f}}\otimes\mathbf{m}_{\mathrm{f}}\\ &+[1-\kappa_{\mathrm{op}}(2+3\kappa_{\mathrm{ip}})]\mathbf{m}_{\mathrm{n}}\otimes\mathbf{m}_{\mathrm{n}}\big\} - p\mathbf{I}.\end{aligned} \tag{6.4}$$

Since we implement this equation in a mathematical software package, we have to write it in matrix notation

$$\begin{aligned}[\boldsymbol{\sigma}] = c\begin{bmatrix}\lambda_1^2 & 0 & 0\\ 0 & \lambda_2^2 & 0\\ 0 & 0 & \lambda_3^2\end{bmatrix} + 4\psi'_{\mathrm{f}i}\Bigg(3\kappa_{\mathrm{ip}}\kappa_{\mathrm{op}}\begin{bmatrix}\lambda_1^2 & 0 & 0\\ 0 & \lambda_2^2 & 0\\ 0 & 0 & \lambda_3^2\end{bmatrix} + 2\kappa_{\mathrm{op}}(1-3\kappa_{\mathrm{ip}})\begin{bmatrix}\lambda_1^2\mathrm{s}^2 & \lambda_1^2\lambda_2^2\mathrm{cs} & 0\\ \lambda_1^2\lambda_2^2\mathrm{cs} & \lambda_2^2\mathrm{c}^2 & 0\\ 0 & 0 & 0\end{bmatrix}\\ + [1-\kappa_{\mathrm{op}}(2+3\kappa_{\mathrm{ip}})]\begin{bmatrix}0&0&0\\0&0&0\\0&0&1\end{bmatrix}\Bigg) - p\begin{bmatrix}1&0&0\\0&1&0\\0&0&1\end{bmatrix},\end{aligned} \tag{6.5}$$

where s and c are abbreviations for $\sin\alpha$ and $\cos\alpha$. Note that the surface in 3-direction is load free ($\sigma_{33} = 0$) which enables us to determine the Lagrangian multiplier $p = c\lambda_3^2 + 4\psi'_{\mathrm{f}i}[3\kappa_{\mathrm{ip}}\kappa_{\mathrm{op}}\lambda_3^2 + 1 - \kappa_{\mathrm{op}}(2+3\kappa_{\mathrm{ip}})]$ in order to solve the system of equations for σ_{11} and σ_{22} (of course we could also solve for three unknowns ($\sigma_{11}, \sigma_{22}, p$) and introduce $\sigma_{33} = 0$ as the third equation).

6.2 Parameter Fitting to Experimental Data from Mechanical Tests

In order to determine the mechanical material parameters of our model, we use experimental data from biaxial tension tests and minimize the so called objective function

$$e = \sum_{\substack{d=1:1,\\ 1:0{,}75,\\ \cdots}} \sum_{i=1}^{n} [(\sigma_{11,i}^{\mathrm{mod},d} - \sigma_{11,i}^{\mathrm{exp},d})^2 + (\sigma_{22,i}^{\mathrm{mod},d} - \sigma_{22,i}^{\mathrm{exp},d})^2], \tag{6.6}$$

where n is the number of data points and d is the data set, e.g., different ratios of a biaxial tension test. This is equivalent to minimizing the sum of squared errors and also a well-accepted means to determine material parameters.

To quantify the goodness of the fit, we calculate the R^2 value which is also known as the coefficient of determination. It is calculated by

$$R^2 = 1 - \frac{SS_{\text{err}}}{SS_{\text{tot}}}, \tag{6.7}$$

where SS_{err} and SS_{tot} are the sum of squares of the differences between model/experiment and mean of experiment/experiment, respectively (for details see, e.g., [Montgomery and Runger, 2010]).

In the Figs. 6.1 and 6.2 the results of fitting the model to four biaxial tension tests of two specimen are shown. The tests were performed with the same sample and different stretch ratios, so the datasets in eq. (6.6) are $d = 1:1, 1:0.75, 0.75:1$ and $0.5:1$. Each dataset contains $3000 - 3500$ data points, depending on the stretch ratio, and was smoothed with a moving average filter with a span of 10 (specimen #1) and 20 (specimen #2) data points. After that, we took 50 datapoints from each experimental dataset (the circles and crosses in Figs. 6.1 and 6.2) and fitted them to the model. Note that all datasets were fitted simultaneously, i.e., one set of parameters is sufficient to obtain a good fit for all four datasets. Moreover we see the great variability between specimen when looking at the magnitude of the stresses.

Table 6.1: Initial values and range for the parameters in the fitting procedure.

Parameter	Initial value	Range	Result #1	Result #2	mean
c [kPa]	10	$0 - 1000$	3.6	12.7	8.15
k_1 [kPa]	30	$0 - 1000$	38.7	16.13	27.6
k_2 [-]	50	$0 - 1000$	16.83	5.27	11.05
κ_{ip} [-]	0.17	$0.1 - 0.18$	0.178	0.16	0.169
κ_{op} [-]	0.49	$0.48 - 0.5$	0.48	0.48	0.48
α [deg]	25	$11 - 35$	32.51	25.46	28.88

Note that although we determined the values for κ_{ip}, κ_{op} and α in chapter 4, we allow the fitting algorithm to slightly vary these values, i.e., we define a small range (in section 4.5). To find the minimum, we used the function `fsolve` in MATLAB which uses a `trust-region-dogleg` algorithm. It should also be mentioned that the parameters κ_{ip} and α are not independent but depend on the starting value, i.e., the same fit can be obtained with different values of κ_{ip} and

α. This is only a problem since we allow these values to vary because we do not have specific histologic information of the respective specimen. Usually, the parameters κ_{ip}, κ_{op} and α can be determined from distribution fitting, as described in section 4.5, and hence need not to be varied in the fitting to mechanical tests.

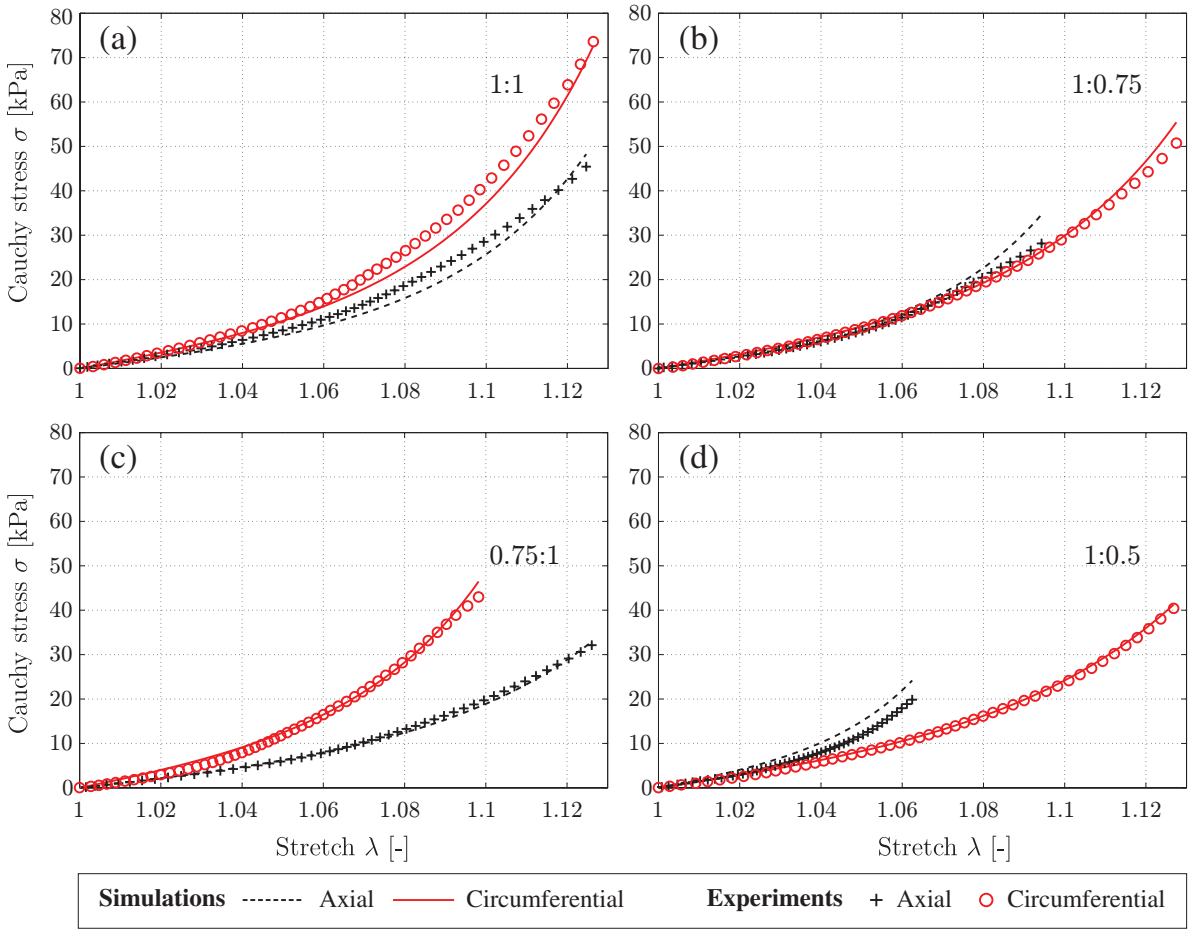

Figure 6.1: Fitting of the proposed model to the results of four biaxial tension tests of specimen #1. The plots show different stretch circumferential to axial stretch ratios of biaxial tests, i.e., (a) $1:1$, (b) $1:0.75$, (c) $0.75:1$ and (d) $1:0.5$. The results of the fit, the initial values and the admissible ranges of the parameters are given in Table 6.1. The good quality of the fit is also reflected in the high coefficient of determination, $R^2 = 0.9828$, which was calculated for all four fits together.

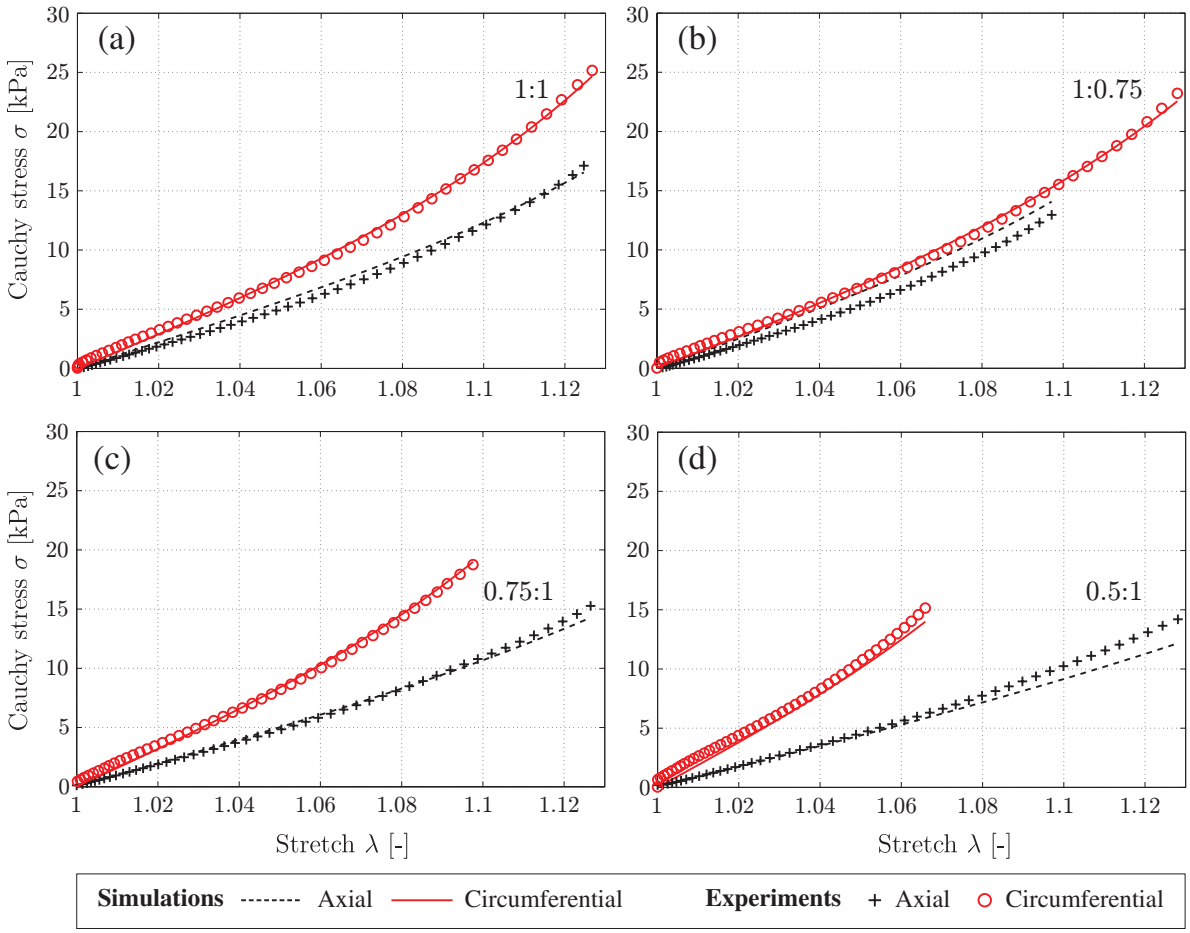

Figure 6.2: Fitting of the proposed model to the results of four biaxial tension tests of specimen #2. The plots show different circumferential to axial stretch ratios of biaxial tests, i.e., (a) $1:1$, (b) $1:0.75$, (c) $0.75:1$ and (d) $0.5:1$. The results of the fit, the initial values, and the admissable ranges of the parameters are given in Table 6.1. Also this specimen yielded a good fit ($R^2 = 0.990$).

6.3 Inflation of a Thin Walled Tube

We consider the inflation of a thin walled tube which is reinforced by two mechanically equivalent, symmetric fiber families dispersed in two planes. The main fiber direction lies in the plane and makes an angle α with the circumferential direction. The material parameters are taken from the previous chapter, see section 6.2 and Table 6.1.

By invoking a membrane approximation, the equilibrium equations in the axial and circumferential direction for a tube subjected to the internal pressure p_i are given by

$$\sigma_z - \frac{r_i^2}{2hr} p_\mathrm{i} = 0, \quad \sigma_\theta - \frac{r_i}{h} p_\mathrm{i} = 0, \tag{6.8}$$

where h, r and r_i are the height, the outer and inner radii in the current configuration, respectively. For an incompressible material, i.e., $\lambda_z \lambda_\theta \lambda_r = 1$, they are related to the respective quantities in the reference configuration through

$$h = \frac{H}{\lambda_\theta \lambda_z}, \quad r = \lambda_\theta R, \quad r_i = r - \frac{h}{2} = \lambda_\theta R - \frac{H}{2\lambda_z \lambda_\theta}, \tag{6.9}$$

see Fig. 6.3 where these quantities are depicted. Note that the tube is thin-walled, i.e., $H/R << 1$, and that the membrane theory does not account for the stress distribution through the thickness of the wall (radial stresses are neglected).

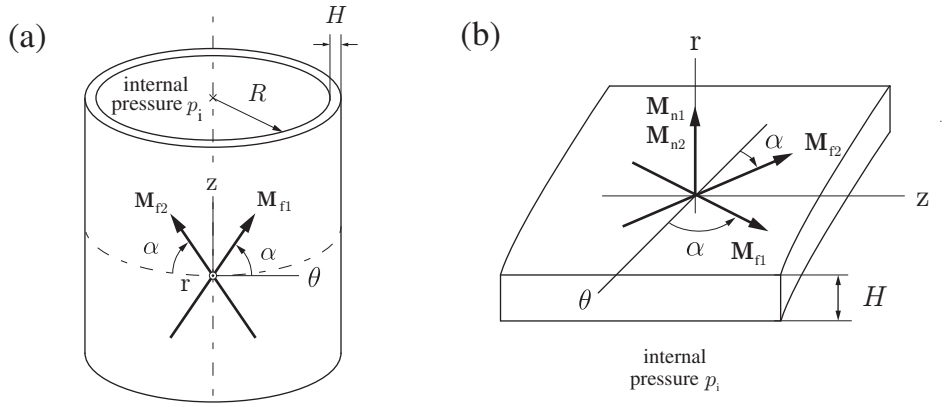

Figure 6.3: (a) Thin walled tube with radius R and thickness H in the reference configuration subjected to the internal pressure p_i. A local coordinate system z, r, θ, oriented in the axial, radial and circumferential direction, is used to define the angle α of two symmetrically dispersed fiber families defined by the vectors $\mathbf{M}_{\mathrm{f}i}$; (b) closeup of the coordinate system where the normal vectors $\mathbf{M}_{\mathrm{n}i}$ oriented in the radial direction are depicted. This means that the mean fiber direction is in-plane, i.e., in the z, θ-plane.

As shown in [Holzapfel, 2000], the principal Cauchy stresses in the axial and circumferential direction read as

$$\sigma_z = \lambda_z \frac{\partial \bar{\Psi}(\lambda_z, \lambda_\theta, \gamma)}{\partial \lambda_z}, \quad \sigma_\theta = \lambda_\theta \frac{\partial \bar{\Psi}(\lambda_z, \lambda_\theta, \gamma)}{\partial \lambda_\theta}, \tag{6.10}$$

and substituting into eq. (6.8) yields

$$\lambda_z \frac{\partial \bar{\Psi}(\lambda_z, \lambda_\theta, \gamma)}{\partial \lambda_z} - \frac{\lambda_z(\lambda_\theta R - (H/(2\lambda_\theta \lambda_z))^2}{2HR} p_\mathrm{i} = 0,$$
$$\lambda_\theta \frac{\partial \bar{\Psi}(\lambda_z, \lambda_\theta, \gamma)}{\partial \lambda_\theta} - \Big(\frac{\lambda_\theta^2 \lambda_z R}{H} - \frac{1}{2}\Big) p_\mathrm{i} = 0. \tag{6.11}$$

The equations in (6.11) form a set of nonlinear equations which can be solved with, e.g., the `fsolve` command in MATLAB. Since the fibers are arranged symmetrically, the principal stretches coincide with the radial and circumferential stretches.

In eq. (6.11), the derivatives of the strain-energy function with respect to the stretches λ_z and λ_θ are required. Recall that we can write eq. (5.17) in terms of the invariants $\bar{I}_1$, $\bar{I}_{4\mathrm{f}}$, and $\bar{I}_{4\mathrm{n}}$ and use the same direction vectors $\mathbf{M}_\mathrm{f}$ and $\mathbf{M}_\mathrm{n}$ as in the previous example, given in eq. (6.2).

In section 6.1 we showed how to derive the SEF directly with respect to the right Cauchy-Green tensor. Now we apply the chain rule with respect to the average strain $\bar{E}$. Using eq. (5.18), we start with the invariants which are given by

$$\bar{I}_1 = \lambda_z^2 + \lambda_\theta^2 + (\lambda_z \lambda_\theta)^{-2}, \quad \bar{I}_{4\mathrm{f}} = \lambda_z^2 \sin^2\alpha + \lambda_\theta^2 \cos^2\alpha, \quad \bar{I}_{4\mathrm{n}} = (\lambda_z \lambda_\theta)^{-2}, \tag{6.12}$$

and their derivatives with respect to the two independent principal stretches are

$$\frac{\partial \bar{I}_1}{\partial \lambda_z} = 2\lambda_z - 2\lambda_z^{-3}\lambda_\theta^{-2}, \quad \frac{\partial \bar{I}_{4\mathrm{f}}}{\partial \lambda_z} = 2\lambda_z \sin^2\alpha, \quad \frac{\partial \bar{I}_{4\mathrm{n}}}{\partial \lambda_z} = -2\lambda_z^{-3}\lambda_\theta^{-2}, \tag{6.13}$$
$$\frac{\partial \bar{I}_1}{\partial \lambda_\theta} = 2\lambda_\theta - 2\lambda_\theta^{-3}\lambda_z^{-2}, \quad \frac{\partial \bar{I}_{4\mathrm{f}}}{\partial \lambda_\theta} = 2\lambda_\theta \cos^2\alpha, \quad \frac{\partial \bar{I}_{4\mathrm{n}}}{\partial \lambda_\theta} = -2\lambda_\theta^{-3}\lambda_z^{-2}. \tag{6.14}$$

Now we are able to compute the derivatives of $\bar{E}$ with respect to the principal stretches using eq. (5.17). Thus,

$$\frac{\partial \bar{E}}{\partial \lambda_i} = 3\kappa_\mathrm{ip}\kappa_\mathrm{op}\frac{\partial \bar{I}_1}{\partial \lambda_i} + \Big[2\kappa_\mathrm{op}(1 - 3\kappa_\mathrm{ip})\Big]\frac{\partial \bar{I}_{4\mathrm{f}}}{\partial \lambda_i} + \Big[1 - \kappa_\mathrm{op}(2 + 3\kappa_\mathrm{ip})\Big]\frac{\partial \bar{I}_{4\mathrm{n}}}{\partial \lambda_i}, \tag{6.15}$$

where $i = \mathrm{z}, \theta$ and the derivatives in eq. (6.14) were used. Using the chain rule, eq. (5.19) and the scalar stress function in eq. $(5.20)_1$, we finally obtain the derivatives of the strain-energy as

$$\frac{\partial \bar{\Psi}}{\partial \lambda_z} = \frac{c}{2}\frac{\partial \bar{I}_1}{\partial \lambda_z} + 2\psi'_{\mathrm{f}i}\frac{\partial \bar{E}}{\partial \lambda_z}, \quad \frac{\partial \bar{\Psi}}{\partial \lambda_\theta} = \frac{c}{2}\frac{\partial \bar{I}_1}{\partial \lambda_\theta} + 2\psi'_{\mathrm{f}i}\frac{\partial \bar{E}}{\partial \lambda_\theta}, \tag{6.16}$$

where the factor 2 appears because both fiber families are symmetric, have the same material/dispersion properties and undergo a symmetric deformation. With eq. (6.16) we can finally

solve the nonlinear system of equations given in eq. (6.11) for $\lambda_z, \lambda_\theta$ when the pressure p_i is prescribed. In Fig. 6.4 we show the results of the simulation of the inflation test, where we compare three different cases. For the first case ('exp. dispersion'), we took the values obtained in section 6.2 and summarized in Table 6.1 to perform the simulation (solid black curve in Fig. 6.4). The red circles are experimental results of an inflation tests of a media-intima composite taken from [Sommer et al., 2010] and are drawn in this plot but did not serve in any fitting procedure. We see that, even though we fitted the material parameters to histology and biaxial tension tests, the results of the simulation matches the experimental data of the inflation test very well.

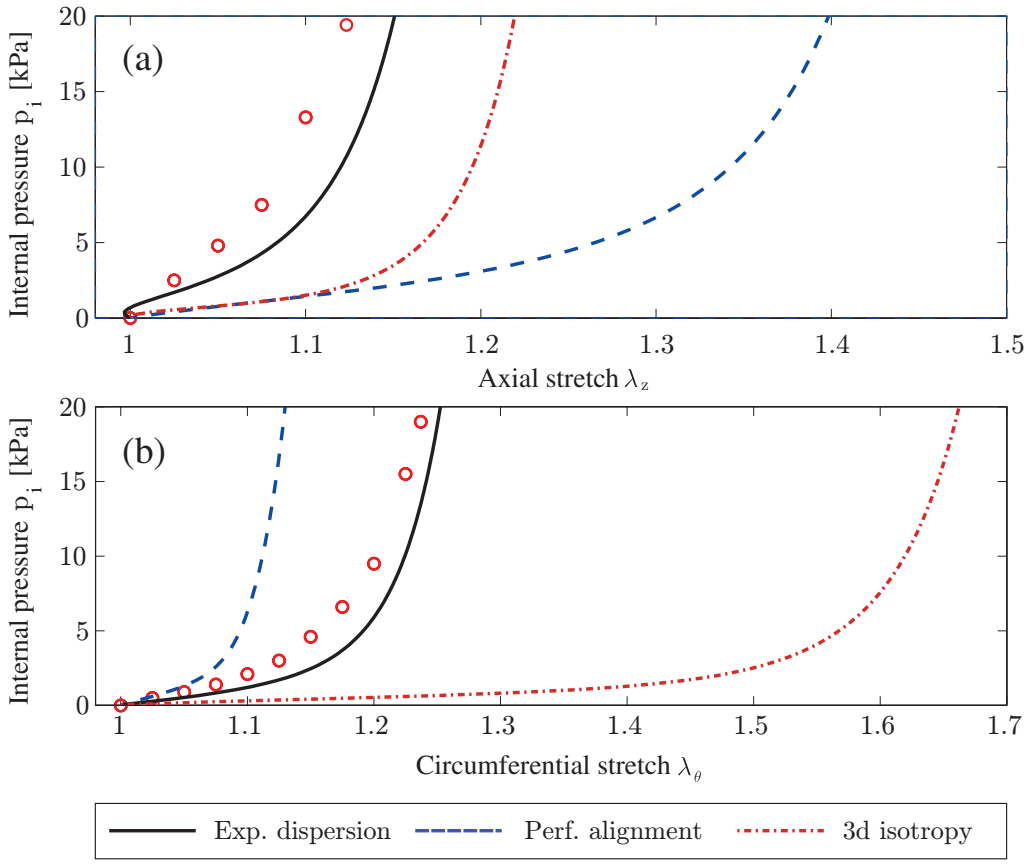

Figure 6.4: In (a) and (b), the results of an inflation test of a thin walled tube with the internal pressure p_i over the axial stretch λ_z and the circumferential stretch λ_θ are shown, respectively. The solid black curves are the result of the simulation with parameters taken from section 6.2, whereas the blue dashed curves and the red dash-dotted curves have the same parameters except that the dispersion parameters are varied (see figure). The red circles are taken from [Sommer et al., 2010] and represent the inflation test of an intima-media composite of a human internal coronary artery which are in the range of the simulation results.

To see the influence of fiber dispersion on the mechanical behavior, we take the same mechanical parameters and change the fiber dispersion to completely isotropic (red dash-dotted curve) and completely aligned (blue dashed curve). For perfect alignment, the tube is stiffer in the circumferential direction and softer in the axial direction than in the case of experimental fiber dispersion since the fibers are oriented more closely to the circumferential direction and not dispersed towards the axial direction. Therefore, no dispersed fibers reinforce the tube in the axial direction, resulting in an unrealistically high stretch in the axial direction. In the 3D isotropic case, the material is softer in both directions because fibers are also dispersed in the 3-direction, i.e., $\kappa_{\text{op}} = 1/3$.

6.4 Finite Element Implementation and Example

In this section we demonstrate the capabilities of our proposed model using a unit cube, reinforced with one fiber family which is aligned in the 1-direction of the coordinate system (see Fig. 6.5(a)). The cube is subjected to biaxial tension in the $1,2$-plane and we investigate four different cases of fiber dispersion: (I) high alignment out-of-plane and in plane; (II) high alignment out-of-plane and less alignment in plane compared to case (I); (III) high alignment out-of-plane and isotropy in plane (2D isotropy), and (IV) isotropy in both planes (3D isotropy), see Fig. 6.5(b) and (c) for details.

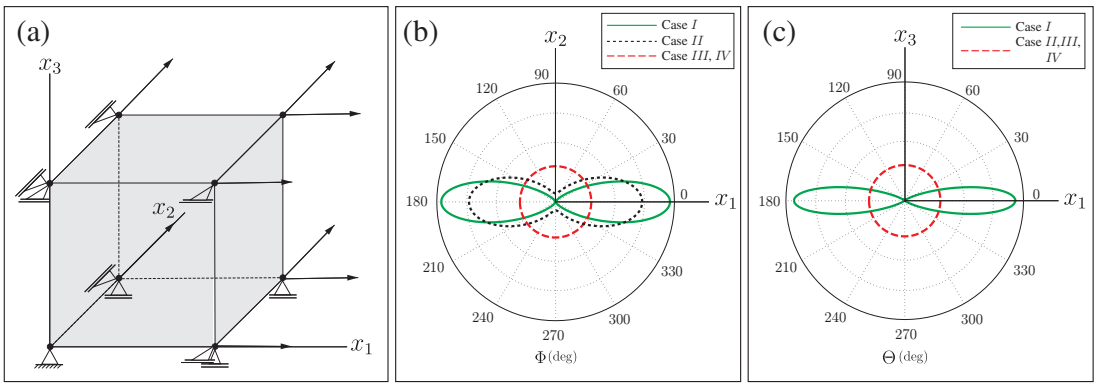

Figure 6.5: (a) Biaxial tension of a cube in the 1- and 2-direction. The deformation is displacement-controlled where the stretches λ_1 and λ_2 are increased to 1.2 and the 3-direction contracts due to incompressibility; (b) and (c) show polar plots of the dispersion cases I-IV for the in-plane and out-of-plane dispersion, respectively.

We use the results of section 5.5 to implement our model in the finite element code FEAP [Taylor, 2000]. The analytical solution and the finite element solution of the biaxial tension of a cube, shown in Fig. 6.5, are depicted in Fig. 6.6. We used four different dispersion cases, outlined in Table 6.2, for the single fiber family oriented in the 1-direction of the coordinate system.

Table 6.2: Four different fiber dispersions for the biaxial tension of a cube. Note that cases I, II and III feature the same (very small) out-of-plane dispersion.

Case	Description	Dispersion Parameters
I	little dispersion in-plane	$\kappa_{\mathrm{ip}}^{I} = 0.066, \kappa_{\mathrm{op}}^{I} = 0.48$
II	larger dispersion in-plane than in case I	$\kappa_{\mathrm{ip}}^{II} = 0.166, \kappa_{\mathrm{op}}^{II} = 0.48$
III	2D-isotropy	$\kappa_{\mathrm{ip}}^{III} = 1/3, \kappa_{\mathrm{op}}^{III} = 0.48$
IV	3D-isotropy	$\kappa_{\mathrm{ip}}^{IV} = 1/3, \kappa_{\mathrm{op}}^{IV} = 1/3$

The maximum stretch in both the 1- and 2-direction is 1.2, and the according stresses are computed using the framework established in section 6.1. To demonstrate the influence of fiber dispersion, we compare four different fiber dispersions summarized in table 6.2. In the cases I-III, the out-of-plane dispersion is $\kappa_{\mathrm{op}}^{I-III} = 0.48$, i.e., a very small amount of fibers is oriented out-of-plane. The in-plane dispersion increases from $\kappa_{\mathrm{ip}}^{I} = 0.066$, $\kappa_{\mathrm{ip}}^{II} = 0.166$ to $\kappa_{\mathrm{ip}}^{III} = 1/3$. Dispersion case IV is a 3D-isotropic dispersion case where the dispersion in all directions is equal, i.e., $\kappa_{\mathrm{ip}}^{IV} = \kappa_{\mathrm{op}}^{IV} = 1/3$.

Figure 6.6 shows a stress-stretch diagram of the stresses σ_{11} and σ_{22}, where 1 is the main fiber direction and $1, 2$ is the main plane of dispersion. The stress in the 1-direction decreases from dispersion case I-III since the dispersion in-plane is increased and more and more fibers are dispersed in the 2-direction (away from the 1-direction). For case IV, the out-of-plane dispersion lowers the stress in both the 1- and 2-direction. In the 2-direction, the stress increases for case I-III since the fibers are dispersed towards the 2-direction. In case IV, however, fibers are turned towards the 3-direction and hence σ_{22} also decreases. Note that for cases III and IV the stresses in 1- and 2-direction are equal, i.e., $\sigma_{11}^{III} = \sigma_{22}^{III}$ and $\sigma_{11}^{IV} = \sigma_{22}^{IV}$, since the dispersion in-plane is isotropic ($\kappa_{\mathrm{ip}}^{III} = \kappa_{\mathrm{ip}}^{IV} = 1/3$).

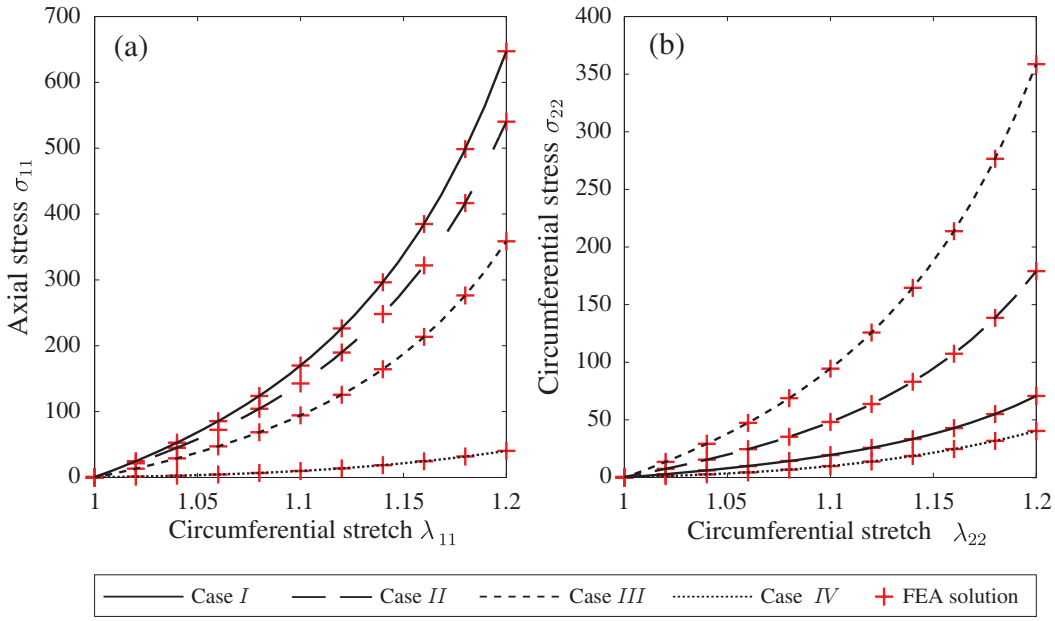

Figure 6.6: Panels (a) and (b) show the stress-stretch plots in the axial and circumferential direction, respectively. The protocol is displacement-driven with a maximal stretch of 1.2. The four different cases of fiber dispersion are depicted in in Fig. 6.5 and Table 6.2. The red crosses represent the solutions of the finite element analysis while the black curves are obtained from the analytical solution of biaxial tension, see section 6.1.

7 Discussion

'The first principle is that you must not fool yourself and you are the easiest person to fool.'

RICHARD P. FEYNMAN

As various previous approaches have shown, incorporating fiber dispersion into a continuum mechanical framework is a challenging task. In the last chapter of this work, we want to address the advantages and disadvantages of our presented model compared to other approaches in the literature.

As discussed in chapter 3, most of the models in the literature do not account for the out-of-plane dispersion of fibers or simply model the fiber dispersion as transversely isotropic. There are some models considering an orthotropic fiber dispersion [Ateshian et al., 2009, Gasser et al., 2012, Alastrué et al., 2010], but they are computationally quite expensive. Moreover, they either do not fit the fiber dispersion function to histological data or have a rather crude experimental approach to determine the collagen fiber orientation.

The work presented in this thesis, in contrast, is based on careful experimental observations showing how to fit histological data from different experimental methods using an easy to handle PDF and maximum likelihood estimation. Our model is fully 3D and based on the GST approach which was introduced in [Gasser et al., 2006]. This method is computationally efficient and embedded in the well-known framework of [Holzapfel et al., 2000]. In [Federico and Herzog, 2008], the authors derive the GST approach in detail and discussed its validity for the arterial wall, where the fiber dispersion can be approximated with a Taylor series and the fibers are loaded in tension.

7.1 Fitting of Distribution Data from Human Arteries

One of our main goals is to account for the structure of biological tissues in our model and to capture the physiological and pathological mechanisms in the arterial wall. This motivates the use of the bivariate *von Mises* distribution to represent the collagen fiber dispersion, which assumes that the dispersion in-plane and out-of-plane are independent [Schriefl et al., 2012a,d].

Multiple collagen fiber families including dispersion lead to overlapping regions which cannot be fitted with a single PDF. To overcome this problem, we use a superposition of two *von Mises* distributions to fit the in-plane data, yielding good results since MLE is a powerful tool to estimate distribution parameters. Even though least squares estimation is very often used to fit distribution functions, we again emphasize that MLE is the more appropriate and in most cases the more efficient approach to determine the parameters of a PDF as we pointed out in [Schriefl et al., 2012b].

We fitted the PDF to experimental data which were obtained with various methods, e.g., picrosirius red staining and polarizing microscopy [Schriefl et al., 2012a], second harmonic image generation [Schriefl et al., 2012d], or optical clearing and SHG [Schriefl et al., 2012d]. With the latter method the authors obtained a series of z-stacks which could be fitted with the methods we outlined in [Schriefl et al., 2012d]. This yields a location and a concentration parameter for each layer and theoretically enables us to consider the inhomogeneous structure of the tissue. Nevertheless, we took the mean/median of the location and dispersion parameters and therefore homogenized the tissue.

Although in healthy arterial walls collagen fibers are mainly oriented in-plane, the need for a model considering the out-of-plane dispersion was emphasized by the results of [Schriefl et al., 2012a], where the authors observed a considerable amount of collagen fibers oriented out-of-plane. More data concerning the dispersion of collagen fibers not only of the arterial wall but of all biological tissues is required, and multiphoton microscopy in combination with optical clearing [Schriefl et al., 2012d] seems to be a powerful tool to obtain dispersion data from various tissues.

7.2 Novel Framework Considering Fiber Dispersion

The main goal of this work is the development of a new structurally motivated continuum mechanical model for the passive arterial wall which incorporates fiber dispersion. Using the concentration parameters of two PDFs, we defined two dispersion measures to quantify the in-plane and out-of-plane dispersion which are used to calculate an average strain quantity. This average strain reduces the complex deformation patterns of the fibers to a scalar and is used in the strain-energy function. From this function, we showed how to derive the stress and elasticity tensors and outlined the necessary mathematical and mechanical background.

As we seek to represent the structure of the tissue, we have to generalize our model to more than one fiber family. There are several approaches to incorporate more fiber families in a continuum mechanical framework, e.g., [Flynn et al., 2011] use six discrete fiber bundles and the model proposed by [Baek et al., 2007] includes four fiber families. The work of [Schriefl et al., 2012a,d] showed that the number of fiber families depends on the location of the artery and the layer, where in most cases two fiber families are reported. Therefore, we extended the formulation to two fiber families.

We also showed how to derive the equations for a biaxial tension test and an inflation test using the proposed model and how to implement them in a numerical package, e.g., MATLAB. After that, we fitted the model to datasets obtained from biaxial tension tests to determine the associated material parameters. Since we do not have the histological information of the specimen we tested in the biaxial test, we allowed the structural parameters obtained from the distribution fitting in section 4.5 to vary a certain range ($\pm$ twice the standard deviation) during the fitting procedure. The excellent fitting results indicate that the model is indeed suitable to describe the mechanical behavior of the human abdominal aortic wall.

In section 6.3 we saw that, even though the parameters were obtained from biaxial tension tests, the results for the inflation test are plausible and in the range of reported values. Of course, this is the result of fitting the parameters to only two biaxial tension tests and the inflation test results are from a different specimen (for details see [Sommer et al., 2010]). Still, it shows that the model is capable of reproducing experimental data even though the parameters were fitted to parameters obtained from a different experimental method.

It is also evident that fiber dispersion has a large influence on the mechanical behavior of the tube, see Fig. 6.4. Also note the inversion of the axial stretch for very small pressures, a phenomenon also observed in, e.g., [Holzapfel and Gasser, 2001]. This is due to the high resistance to axial stretch because of the fibers, and at very low pressures its energetically more favourable to contract in the axial direction. Fibers are a crucial means in the body to endow soft tissue with tensile strength, and their orientation and dispersion strongly affect the mechanical behavior. This can also be seen in section 6.4, where different dispersion cases are compared (in the same example we validate the finite element implementation by comparing it to the analytical solution of the biaxial tension test).

7.3 Limitations

One of the main simplifications of this model is the computation of an average stretch, and this might not be appropriate for every tissue type and every load case. Nevertheless, our framework yields good fits to biaxial tension data and is capable to reproduce results in the range of reported values of inflation tests, so we assume that this simplification is justified to some extent.

It is also possible to implement this model using angular integration (AI) rather than the generalized structure tensor (GST), but since AI does not describe the fiber dispersion with integral dispersion measures but requires an integration of infinitesimal fiber fractions, a large number of calculations would have to be performed to evaluate the strains and stresses [Cortes et al., 2010].

For the inflation test in section 6.3, we used the membrane theory for the sake of simplicity and we neglect stresses in the radial direction. For saccular aneurysm or cerebral arteries this assumption holds, but the aorta and the large blood vessels have to be treated as thick-walled vessels.

The split of the strain-energy function for anisotropic, hyperelastic materials is also a topic which is not completely understood yet for the compressible case, see [Sansour, 2007] and [Helfenstein et al., 2010] for a discussion on this issue. Nevertheless we follow the work of [Holzapfel et al., 2000] and decompose the SEF in a volumetric and a deviatoric part for the numerical FE analysis. In most physiological and pathological cases we can neglect viscous ef-

fects like stress relaxation and creep. Furthermore, we also neglect inertia forces and, therefore, have to solve quasi-static initial-boundary value problems [Taylor and Humphrey, 2009].

Since a biological tissue is a very complex material, modeling the mechanical behavior of the arterial wall requires a lot of assumptions. Even though most models describing fiber dispersion make these assumptions, we want to briefly discuss the simplifications we make. Probably the most profound assumption is that we neglect the active contribution of smooth muscle cells and only consider the passive behavior of the artery. Residual stresses are another important phenomenon in the arterial wall, which are believed to have a great influence on the mechanics of soft biological tissue [Holzapfel and Ogden, 2010a]. Also incompressibility and the isotropy of the elastin network are assumptions, but there is evidence in the literature justifying this assumptions, see, e.g., [Gundiah et al., 2007]. Our framework does not yet consider growth and remodeling [Valentínn et al., 2013] and also works on quite a macroscopic level, although especially the role of proteoglycans on the molecular level might be important [Azeloglu et al., 2007, Schmidt et al., 2013].

Another limitation of this work is the lack of histological data which calls for more experiments to obtain structural data of both healthy and diseased blood vessels. But one also has to consider the highly inhomogeneous histology of soft biological tissue, in general, and the extreme variation between specimens especially for diseased aortas in particular. These considerable individual histological differences make it difficult to provide general statements about the microstructure of blood vessels.

Bibliography

A. Agianniotis, R. Rezakhaniha, and N. Stergiopulos. A structural constitutive model considering angular dispersion and waviness of collagen fibres of rabbit facial veins. *Biomedical Engineering OnLine*, 10:18, 2011.

V. Alastrué, M. A. Martinez, M. Doblaré, and A. Menzel. Anisotropic micro–sphere–based finite elasticity applied to blood vessel modelling. *J. Mech. Phys. Solids*, 57:178–203, 2009a.

V. Alastrué, M. A. Martinez, A. Menzel, and M. Doblaré. On the use of non-linear transformations for the evaluation of anisotropic rotationally symmetric directional integrals. application to the stress analysis in fibred soft tissues. *Int. J. Numer. Meth. Engng*, 79:474–504, 2009b.

V. Alastrué, P. Sáez, M. A. Martínez, and M. Doblaré. On the use of the bingham statistical distribution in microsphere-based constitutive models for arterial tissue. *Mech. Res. Commun.*, 37:700–706, 2010.

B. Alberts, D. Bray, J. Lewis, M. Raff, K. Roberts, and J. D. Watson. *Molecular Biology of the Cell*. Garland Publishing, New York, 1994.

S. M. Arribas, A. Hinek, and M. C. Gonzalez. Elastic fibres and vascular structure in hypertension. *Pharmacol. Ther.*, 111:771–791, 2006.

E. M. Arruda and M. C. Boyce. A three–dimensional constitutive model for the large stretch behavior of rubber elastic materials. *J. Mech. Phys. Solids*, 41:389–412, 1993.

G. A. Ateshian, V. Rajan, N. O. Chahine, C. E. Canal, and C. T. Hung. Modeling the matrix of articular cartilage using a continuous fiber angular distribution predicts many observed phenomena. *J. Biomech. Eng.*, 131:61003, 2009.

E. U. Azeloglu, M. B. Albro, V. K. Thimmappa, G. A. Ateshian, and K. D. Costa. Heterogeneous transmural proteoglycan distribution provides a mechanism for regulating residual stresses in the aorta. *Am. J. Physiol. Heart Circ. Physiol.*, 294:1197–1205, 2007.

S. Baek, R. L. Gleason, K. R. Rajagopal, and J. D. Humphrey. Theory of small on large: potential utility in computations of fluid-solid interactions in arteries. *Comput. Meth. Appl. Mech. Eng.*, 196:3070–3078, 2007.

K. L. Billiar and M. S. Sacks. Biaxial mechanical properties of the natural and glutaraldehyde treated aortic valve cusp – Part I: Experimental results. *J. Biomech.*, 122:23–30, 2000.

P. Boutouyrie, D. P. Germain, A. I. Tropeano, B. Laloux, F. Carenzi, M. Zidi, X. Jeunemaitre, and S. Laurent. Compressibility of the carotid artery in patients with pseudoxanthoma elasticum. *Hypertension*, 38:1181–1184, 2001.

A. C. Burton. Relation of structure to function of the tissues of the wall of blood vessels. *Physiological Reviews*, 34:619–642, 1954.

F. C. Caner, Y. Guo, B. Moran, Y. P. Bažant, and I. Carol. Hyperelastic anisotropic microplane constitutive model for annulus fibrosus. *Trans. Am. Soc. Mech. Eng.*, 128:632–641, 2007.

D. H. Cortes, S. P. Lake, J. A. Kadlowec, L. J. Soslowsky, and D. M. Elliot. Characterizing the mechanical contribution of fiber angular distribution in connective tissue: comparison of two modeling approaches. *Biomech. Model. Mechanobiol.*, 9:651–658, 2010.

J. M. Davidson, K. E. Hill, and J. L. Alford. Developmental changes in collagen and elastin biosynthesis in the porcine aorta. *Dev. Biol.*, 118:103–111, 1986.

J. Díez. *Arterial Stiffness and Extracellular Matrix*. Blackwell Publishing, 2007.

N. J. Driessen, A. Mol, C. V. Bouten, and F. P. Baaijens. Modeling the mechanics of tissue-engineered human heart valve leaflets. *J. Biomech.*, 40:325–334, 2007.

N. J. B. Driessen, C. V. C. Bouten, and F. P. T. Baaijens. A structural constitutive model for collagenous cardiovascular tissue incorporating the angular fiber distribution. *J. Biomech. Eng.*, 127:494–503, 2005.

D. R. Einstein. *Nonlinear Acoustic Analysis of the Mitral Valve*. PhD thesis, University of Washington, Seattle, 2002.

T. S. E Eriksson, D. M. Pierce, and G. A. Holzapfel. On tension-compression switching in dispersed fiber-reinfoces constitutive models. *unpublished*, submitted.

M. Evans, N. Hastings, and B. Peacock. *Statistical Distribution*. John Wiley & Sons, New York, 2000.

A. Federico and A. Grillo. Elasticity and permeability of porous fibre reinforced materials under large deformations. *Mech. Mat.*, 44:58–71, 2012.

A. Federico and W. Herzog. On the permeability of fibre-reinforced porous materials. *Int. J. Solids Structures*, 45:2160–2172, 2008.

S. Federico and T. C. Gasser. Nonlinear elasticity of biological tissues with statistical fibre orientation. *J. R. Soc. Interface*, 7:955–966, 2010.

P. J. Flory. Thermodynamic relations for highly elastic materials. *Trans. Faraday Soc.*, 57: 829–838, 1961.

C. Flynn, M.B. Rubin, and P. Nielsen. A model for the anisotropic response of fibrous soft tissues using six discrete fibre bundles. *Int. J. Numer. Meth. Biomed. Engng.*, 27:1793–1811, 2011.

O. Frank. Die grundform des arteriellen pulses (translated by k. sagawa, r.k. lie and j. schaefer. *JMCC*, 22:253–277, 1899/1990.

P. Fratzl and R. Weinkamer. Nature's hierarchical materials. *Progress in Material Science*, 52: 1263–1334, 2007.

A. D. Freed and T. C. Doehring. Elastic model for crimped collagen fibrils. *J. Biomech. Eng.*, 127:587–593, 2005.

A. D. Freed, D. R. Einstein, and I. Vesely. Invariant formulation for dispersed transverse isotropy in aortic heart valves: An efficient means for modeling fiber splay. *Biomech. Model. Mechanobiol.*, 4:100–117, 2005.

Y. C. Fung. *Foundations of Solid Mechanics*. Prentice-Hall, Englewood Cliffs, New Jersey, 1965.

Y. C. Fung. Elasticity of soft tissues in simple elongation. *Am. J. Physiol.*, 213:1532–1544, 1967.

Y. C. Fung. *Biomechanics: Mechanical Properties of Living Tissue*. Springer-Verlag, New York, 1981.

Y. C. Fung. *Biomechanics. Mechanical Properties of Living Tissues*. Springer-Verlag, New York, 2nd edition, 1993.

T. C. Gasser, R. W. Ogden, and G. A. Holzapfel. Hyperelastic modelling of arterial layers with distributed collagen fibre orientations. *J. R. Soc. Interface*, 3:15–35, 2006.

T. C. Gasser, S. Gallinetti, X. Xing, C. Forsell, J. Swedenborg, and J. Roy. Spatial orientation of collagen fibers in the abdominal aortic aneurysms wall and its relation to wall mechanics. *Acta Biomater.*, 8:3091–3103, 2012.

A. I. Gottlieb. *Rubin's Pathology - Clinicopathologic Foundations of Medicine*. Lippincott Williams & Wilkins, 351 West Camden Street, Baltimore, MD 21201, 2007.

A. E. Green and J. E. Adkins. *Large Elastic Deformations*. Oxford University Press, Oxford, England, 2nd edition, 1970.

N. Gundiah, M. B. Ratcliffe, and L. A. Pruitt. Determination of strain energy function for arterial elastin: Experiments using histology and mechanical tests. *J. Biomech.*, 40:586–594, 2007.

J. Helfenstein, M. Jabareen, E. Mazza, and S. Govindjee. On non-pyhsical response in models for fiber-reinforced hyperelastic materials. *Int. J. Solids Structures*, 47:2056–2061, 2010.

G. A. Holzapfel. On large strain viscoelasticity: Continuum formulation and finite element applications to elastomeric structures. *Int. J. Numer. Meth. Engng*, 39:3903–3926, 1996.

G. A. Holzapfel. *Nonlinear Solid Mechanics. A Continuum Approach for Engineering*. John Wiley & Sons, Chichester, 2000.

G. A. Holzapfel and T. C. Gasser. A viscoelastic model for fiber-reinforced composites at finite strains: Continuum basis, computational aspects and applications. *Comput. Meth. Appl. Mech. Eng.*, 190:4379–4403, 2001.

G. A. Holzapfel and R. W. Ogden. Modelling the layer-specific 3D residual stresses in arteries, with an application to the human aorta. *J. R. Soc. Interface*, 7:787–799, 2010a.

G. A. Holzapfel and R. W. Ogden. Constitutive modelling of arteries. *Proc. R. Soc. Lond. A*, 466:1551–1597, 2010b.

G. A. Holzapfel and H. W. Weizsäcker. Biomechanical behavior of the arterial wall and its numerical characterization. *Comp. Biol. Med.*, 28:377–392, 1998.

G. A. Holzapfel, T. C. Gasser, and R. W. Ogden. A new constitutive framework for arterial wall mechanics and a comparative study of material models. *J. Elasticity*, 61:1–48, 2000.

G. A. Holzapfel, T. C. Gasser, and R. W. Ogden. Comparison of a multi-layer structural model for arterial walls with a Fung-type model, and issues of material stability. *J. Biomech. Eng.*, 126:264–275, 2004.

G. A. Holzapfel, G. Sommer, C. T. Gasser, and P. Regitnig. Determination of the layer-specific mechanical properties of human coronary arteries with non-atherosclerotic intimal thickening, and related constitutive modelling. *Am. J. Physiol. Heart Circ. Physiol.*, 289:H2048–2058, 2005a.

G. A. Holzapfel, M. Stadler, and T. C. Gasser. Changes in the mechanical environment of stenotic arteries during interaction with stents: Computational assessment of parametric stent design. *J. Biomech. Eng.*, 127:166–180, 2005b.

D. J. S. Hulmes. Collagen diversity, synthesis and assembly. In P. Fratzl, editor, *Collagen: Structure and Mechanics*, pages 15–47. Springer, 2008.

J. D. Humphrey. *Cardiovascular Solid Mechanics. Cells, Tissues, and Organs*. Springer-Verlag, New York, 2002.

J. D. Humphrey and P. B. Canham. Structure, mechanical properties and mechanics of intracranial saccular aneurysms. *J. Elasticity*, 61:49–81, 2000.

Kowalak, Cavallini, Chohan, Hughes, Johanson, and Poeggel, editors. *Handbook of Pathophysiology*. Lippincott Williams & Wilkins, Springhouse Coporation, 1111 Bethlehem Pike, P.O. Box 908, PA 19477-0908, 2001.

M. Kroon and G. A. Holzapfel. A new constitutive model for multi-layered collagenous tissues. *J. Biomech.*, 41:2766–2771, 2008.

E. Kuhl, A. Menzel, and K. Garikipati. On the convexity of transversely isotropic chain network models. *Phil. Mag. Lett.*, 86:3241–3258, 2005.

M. R. Labrosse. *Structure and Mechanics of the Artery*, pages 45–81. Springer US, 2007.

Y. Lanir. Constitutive equations for fibrous connective tissues. *J. Biomech.*, 16:1–12, 1983.

P. Libby, P. M. Ridker, and G. K. Hansson. Progress and challenges in translating the biology of atherosclerosis. *Nature*, 473:319–325, 2011.

L. Lyons. *Statistics for Nuclear and Particle Physicists*. Cambridge University Press, Cambridge, 1989.

K. I. Mardia. Statistics of directional data (with discussion). *J. Roy. Statist. Soc. Ser. B*, 37: 349–393, 1975.

K. V. Mardia and P. E. Jupp. *Directional Statistics*. John Wiley & Sons, Ltd, 1999.

K. Miura. An introduction to maximum likelihood estimation and information geometry. *Interdisciplinary Information Sciences*, 17:155–174, 2011.

D. C. Montgomery and G. C. Runger. *Applied Statistics and Probability for Engineers*. John Wiley & Sons, Ltd, 2010.

M. E. Nimni. Collagen in cardiovascular tissue. In G. W. Hastings, editor, *Cardiovascular Biomaterials*. Springer-Verlag, New York, 1992.

R. W. Ogden. On the overall moduli of non-linear elastic composite. *J. Mech. Phys. Solids*, 22: 541–553, 1974.

R. W. Ogden. Nearly isochoric elastic deformations: Application to rubberlike solids. *J. Mech. Phys. Solids*, 26:37–57, 1978.

R. W. Ogden. *Non-linear Elastic Deformations*. Dover, New York, 1997.

V. Ottani, M. Raspanti, and A. Ruggeri. Collagen structure and functional implications. *Micron*, 32:251–260, 2001.

A. Pandolfi and M. Vasta. Fiber distributed hyperelastic modeling of biological tissues. *Mech. Mat.*, 44:151–162, 2012.

K. H. Parker. A brief history of arterial wave mechanics. *Med. Biol. Eng. Comput.*, 47:111–118, 2009.

R. Raghupathy and V. H. Barocas. A closed-form structural model of planar fibrous tissue mechanics. *J. Biomech.*, 42:1424–1428, 2009.

K. Reiser, R. J. McCormick, and R. B. Rucker. Enzymatic and nonenzymatic cross-linking of collagen and elastin. *FASEB J.*, 6:2439–2449, 1992.

M. S. Sacks. Incorporation of experimentally-derived fiber orientation into a structural constitutive model for planar collagenous tissues. *J. Biomech. Eng.*, 125:280–287, 2003.

C. Sansour. On the physical assumptions underlying the volumetric isochoric split and the case of anisotropy. *Eur. J. Mech. A/Solids*, 27:28–39, 2007.

T. Schmidt, D. Balzani, A. J. Schriefl, and G. A. Holzapfel. Modeling and experimental investigations of the stress-softening behavior of soft collagenous tissues. In *XII International Conference on Computational Plasticity. Fundamentals and Applications*, Barcelona, September 03-05, 2013 2013. Conference Paper.

F. J. Schoen. *Robbins Pathologic Basis of Disease*. W.B. Saunders Company., The Curtis Center, Independence Square West, Philadelphia, Pennsylvania 19106, 1994.

A. J. Schriefl, G. Zeindlinger, D. M. Pierce, P. Regitnig, and G. A. Holzapfel. Determination of the layer-specific distributed collagen fiber orientations in human thoracic and abdominal aortas and common iliac arteries. *J. R. Soc. Interface*, 9:1275–1286, 2012a.

A. J. Schriefl, M. J. Collins, D. M. Pierce, G. A. Holzapfel, L. E. Niklason, and J. D. Humphrey. Remodeling of intramural thrombus and collagen in an Ang-II infusion ApoE-/- model of dissecting aortic aneurysms. *Thromb. Res.*, 130:e139–146, 2012b.

A. J. Schriefl, A. J. Reinisch, S. Sankaran, D. M. Pierce, and G. A. Holzapfel. Quantitative assessment of collagen fiber orientations from 2D images of soft biological tissues. *J. R. Soc. Interface*, 9:3081–3093, 2012c.

A. J. Schriefl, H. Wolinski, P. Regitnig, S. D. Kohlwein, and G. A. Holzapfel. An automated approach for three-dimensional quantification of fibrillar structures in optically cleared soft biological tissues. *J. R. Soc. Interface*, 10:1–10, 2012d.

A. J. Schriefl, H. Wolinski, S. D. Kohlwein, and G. A. Holzapfel. Structural differences in collagen morphologies between healthy and aaa tissues. In *The 4th Canadian Conference on Nonlinear Solid Mechanics (CanCNSM 2013), book of abstracts*, Montréal, July 23-26, 2013 2013a. Abstract.

R. E. Shadwick. Mechanical design in arteries. *J. Exp. Biol.*, 202:3305–3313, 1999.

J. C. Simo, R. L. Taylor, and K. S. Pister. Variational and projection methods for the volume constraint in finite deformation elasto-plasticity. *Comput. Meth. Appl. Mech. Eng.*, 51:177–208, 1985.

G. Sommer, P. Regitnig, L. Költringer, and G. A. Holzapfel. Biaxial mechanical properties of intact and layer–dissected human carotid arteries at physiological and supra-physiological loadings. *Am. J. Physiol. Heart Circ. Physiol.*, 298:H898–912, 2010.

A. J. M. Spencer. Constitutive theory for strongly anisotropic solids. In A. J. M. Spencer, editor, *Continuum Theory of the Mechanics of Fibre-Reinforced Composites*, pages 1–32. Springer-Verlag, Wien, 1984. CISM Courses and Lectures no. 282.

C. A. Taylor and J. D. Humphrey. Open problems in computational vascular biomechanics: hemodynamics and arterial wall mechanics. *Comput. Meth. Appl. Mech. Eng.*, 198:3514–3523, 2009.

R. L. Taylor. *FEAP – A Finite Element Analysis Program – Version 7.3*. University of California at Berkeley, 2000.

A. Valentínn, J. D. Humphrey, and G. A. Holzapfel. A finite element based constrained mixture implementation for arterial growth, remodeling, and adaptation: theory and numerical verification. 2013. in press.

J. E. Wagenseil and R. P. Mecham. Vascular extracellular matrix and arterial mechanics. *Phys. Rev. A (3)*, 89:957–989, 2009.

J. A. Weiss, B. N. Maker, and S. Govindjee. Finite element implementation of incompressible, transversely isotropic hyperelasticity. *Comput. Meth. Appl. Mech. Eng.*, 135:107–128, 1996.

WHO Media centre. Cardiovascular diseases (CVDs), September 2012. URL `http://www.who.int/mediacentre/factsheets/fs317/en/index.html`.

Statutory Declaration

I declare that I have authored this thesis independently, that I have not used other than the declared sources/resources, and that I have explicitly marked all material, which has been quoted by the relevant reference.

date

signature